Alma Mater Studiorum – Università di Bologna

Dipartimento di Fisica e Astronomia "Augusto Righi"
Laurea Magistrale in Fisica del Sistema Terra

Love numbers of super-Earths: a numerical approach

Presentata da:
Luca Francioni

Relatore:
Prof. Giorgio Spada

Correlatore:
Dott. Daniele Melini

Anno Accademico 2025 - 2026
Appello II

Abstract

Studiare la deformabilità di un pianeta è uno degli approcci più adeguati a ricostruire la sua struttura interna. Testando diversi modelli del pianeta è possibile produrre vari set di valori di numeri di Love, i coefficienti adimensionali che ne parametrizzano completamente la risposta deformativa sotto l'azione di sorgenti perturbative esterne e interne. Esistono tre tipi di numeri di Love: i numeri di Love mareali misurano la risposta a un potenziale esterno al pianeta; i numeri di Love di carico misurano la risposta a un carico posto direttamente sulla superficie planetaria; i numeri di Love di taglio misurano la risposta a forze di taglio applicate tangenzialmente alla superficie. In questa tesi è presentato un approccio numerico per la stima di tutti i numeri di Love della Terra e di tre classi di super Terre, una delle tipologie di esopianeti più diffuse nell'universo. I modelli interni assunti in questo studio sono sia completamente solidi che aventi un nucleo esterno fluido, e sono considerati sia in casi comprimibili che incomprimibili, con reologia elastica. Dopo aver presentato la teoria completa della deformazione planetaria, introduciamo il codice sviluppato per l'integrazione numerica della deformazione e dei numeri di Love di ogni modello. In seguito, discutiamo il metodo usato per costruire il modello interno più adatto a ogni taglia di super Terra, produciamo dei set di numeri di Love per ognuna di esse e li compariamo con quelli ottenuti per la Terra. I nostri risultati di numeri di Love per la Terra tendono a sovrastimare i valori precedentemente noti in letteratura. Per la super Terra avente massa pari a $2\,M_\oplus$, otteniamo una risposta deformativa inferiore a quella manifestata dalla Terra: l'aumento in massa e raggio non riesce a bilanciare l'aumento del profilo di rigidità del pianeta. Per la super Terra avente massa pari a $4\,M_\oplus$, i numeri di Love sono comparabili con quelli della Terra con una differenza nei loro valori al massimo del $35\,\%$, indicando una risposta deformativa simile tra i due corpi celesti. Per la super Terra avente massa pari a $8\,M_\oplus$, l'aumento nelle dimensioni del pianeta domina completamente la risposta deformativa, generando numeri di Love sempre più grandi almeno del $20\,\%$ delle loro controparti terrestri. Vengono infine proposti alcuni miglioramenti al metodo adottato in questa tesi che, alla conoscenza dei relatori e dell'autore, è il primo lavoro ad avere come obiettivo la stima dei numeri di Love di super Terre rocciose e la comparazione di questi ultimi con i numeri di Love della Terra.

Abstract

Studying the deformability of a planet is one of the most meaningful approaches to infer its internal structure. By testing many models of the planet, it is possible to produce different datasets of Love numbers, *i.e.* the dimensionless coefficients that fully parameterize the deformation response of the planet under a perturbative action exerted by external and internal sources. There are three types of Love numbers: tidal Love numbers due to an external massive body; load Love numbers due to a load directly located in contact with the planetary surface; and shear Love numbers due to shear forces acting tangentially on the surface. In this thesis, we present a numerical approach for the evaluation of all the Love numbers of the Earth and of three classes of super-Earths, one of the most widespread kinds of exoplanets in the universe. The interior models we assumed for this study are both fully solid and with a fluid outer core, and are considered in both compressible and incompressible cases, in elastic rheology. After presenting the complete theory of planetary deformations, we introduce the code developed to carry out the numerical integration of deformations and Love numbers for each model. Then, we discuss the method used to build up the most suitable interior model for every super-Earth size, we produce datasets of Love numbers for each of them, and we compare these latter to the datasets produced for Earth. Our results for the Love numbers of the Earth generally overestimate the already-known values presented in the past literature. For the super Earth of $2\,M_{\oplus}$, we obtain a smaller deformation response than the one manifested from the Earth: the increase in mass and radius cannot balance the increase in the rigidity profile of the planet. For the super-Earth of $4\,M_{\oplus}$, its Love numbers are comparable with the terrestrial ones in a range of at maximum $35\,\%$ difference, indicating a similar response to perturbations. For the super-Earth of $8\,M_{\oplus}$, the increase in the dimension of the planet completely dominates the deformation response, producing Love numbers at least $20\,\%$ greater than their counterparts for the Earth. In the end, we propose some improvement scenarios for the method we have adopted in this work, which, to the knowledge of the supervisors and the author, is the first work having the aim of evaluating Love numbers of rocky super-Earths and comparing them to the Love numbers of the Earth.

Contents

Chapter 1

Introduction

1 Beyond the planet Earth system

In the last decades the understanding that scientific community has developed of the Earth in our Solar System has evolved: besides our planet, in fact, a lot of planetary bodies have been discovered all around our galaxy, even in stellar systems that are completely different from the one we live in.
Thanks to the great improvement in the instrumentation and observational capabilities, the search for exoplanets has collected a lot of data on planetary populations employing various techniques: the transit method and radial velocity spectroscopy have been the most useful for their detection [Coughlin et al., 2016, NASA, 2026]. Furthermore, statistical analysis on the detectable physical properties of these celestial bodies - mainly *mass* and *radius* - has confirmed that planets with size similar to the Earth or bigger represent one of the largest populations in the Milky Way. This conclusion makes Earth-like rocky planets one of the most interesting research fields for the future, especially in the size range of the so-called *super-Earths*.

Currently, the main challenge of Planetary Geophysics is to characterize the nature and the internal structure of the exoplanets. Understanding how planets are internally structured is the key to unveil their formation mechanisms and the evolution of the Earth itself. In order to elaborate and develop proper interior models for exoplanets, the deep knowledge of our planet is fundamental and *vice versa*. To study rocky massive regimes, the use of Earth-like models can provide meaningful information on the dependence that planetary parameters show on size and internal differentiation. At the same time, the progress reached in describing these planetary classes will improve our testing possibilities on the interior of the Earth. In fact, as we will see in the following study, our planet can be considered as a lower limit case of the super-Earth planetary regime, and not a unique presence in the universe anymore.

2 Super-Earths

In modern Planetary Sciences, the class of super-Earths is defined as the class of planets having a mass from two up to ten times the mass of the Earth [NASA, 2026]. These celestial bodies are more massive than our planet but lighter than the gas giants. The first super-Earths were discovered by the Arecibo radiotelescope in 1992, orbiting around the pulsar *PSR B1257+12* [Wolszczan and Frail, 1992]; later renamed as Poltergeist and Phobetor, they have masses four times the Earth and they are at about 980 light years from the Solar System, in the Virgo constellation. Since then, super-Earths have been revealed to be one of the most widespread kinds of planet in our galaxy: on more than 6200 exoplanets found until 2026, about 30 % (1793) of the total are super-Earths or fall in a range no greater than 50 % of their maximum size [NASA, 2026].
The detection methods that astronomers use nowadays to discover new exoplanets allow to obtain indirectly a few physical properties of them, among which the most important are their mass and radius. Recalling that the Earth mass is: $M_\oplus = 5.972 \cdot 10^{24}\,kg$, the mass distribution of the currently known super-Earths is displayed in Fig. 1.1.

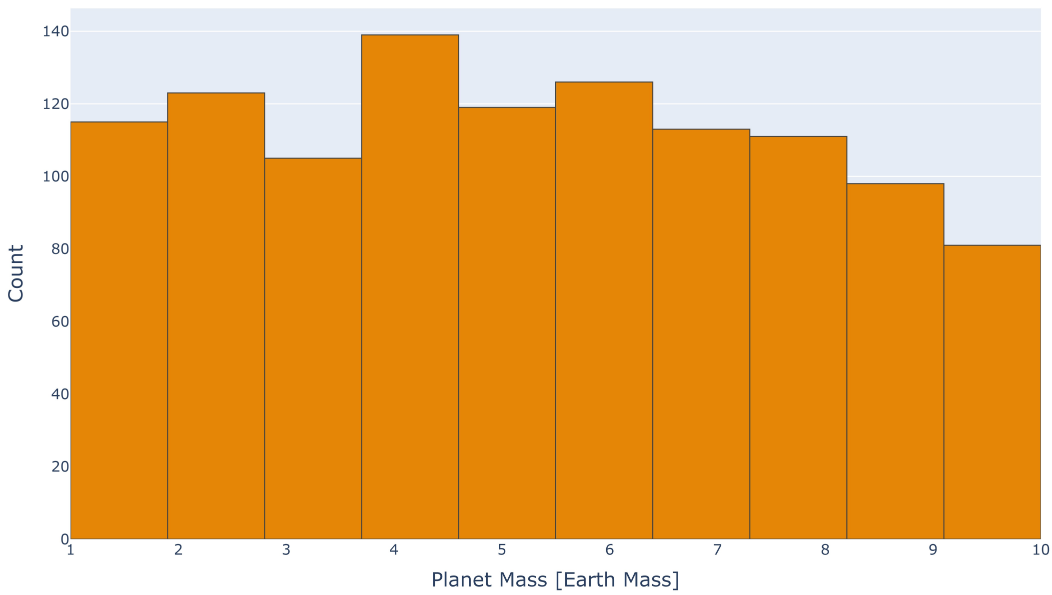

Figure 1.1: *Mass distribution of the currently discovered exoplanets between one up to ten times the size of the Earth, in units of Earth masses $M_\oplus$, obtained by data and plotting tools of [NASA, 2026] database. Here, only the planets that have a confirmed mass in the super-Earths range (about 1130 out of 1793) are reported, while the missing super-Earths have their minimum mass that falls in this range; we have chosen not to report them for the clarity of dataset.*

Meaningful relations between mass and radius of super-Earths have been established along the years starting from [Valencia et al., 2006] and [Sotin et al., 2007]. There are many works in the past literature that carried out a detailed classification of relations between mass and radius in very massive planetary regimes [Zeng and Sasselov, 2013], also covering rocky cases [Zeng et al., 2016].
Recalling that the Earth radius is: $R_\oplus = 6371\,km$, the mass-radius distribution of the currently known super-Earths is displayed in Fig. 1.2.

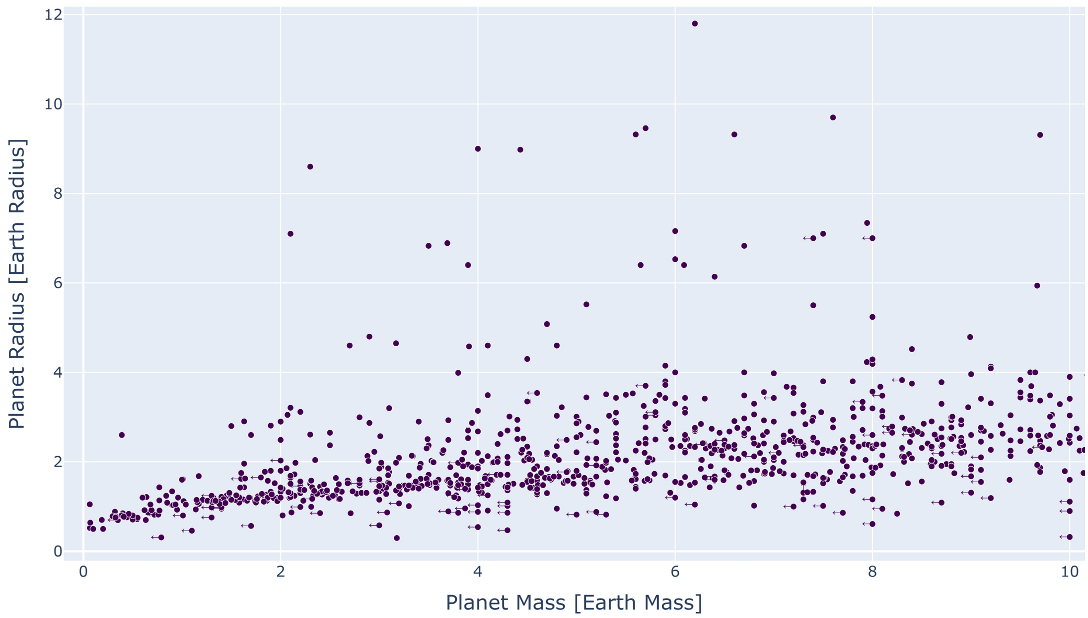

Figure 1.2: *Mass vs Radius distribution of the currently discovered exoplanets up to ten times the size of the Earth, in units of Earth masses $M_\oplus$ and Earth radii $R_\oplus$, obtained by data and plotting tools of [NASA, 2026] database.*

Fundamental works like [Valencia et al., 2007] and [Van Heck and Tackley, 2011] have highlighted another important geophysical feature: the possibility of plate tectonics on super-Earths. Not only is this phenomenon considered sustainable in a more massive planet, but it is also more likely than in the Earth's case: the larger the planet mass the higher the stress induced on its solid components, and this makes tectonic plates thinner, which in turn facilitates their motion. As a consequence, the Earth could be the lowest mass regime that is able to sustain active plate tectonics.

Moreover, in the opinion of astrobiologists, super-Earths are also considered to be valid candidates to host life. Since the 2000s, a lot of exoplanets have been discovered in the habitable zone of their orbital systems, and many of these are super-Earths [Udry et al., 2007]. Recently, super-Earths in habitable zone have been detected at a few light-year distances from the Earth too [Mendenhall, 2026, Conzo et al., 2026]. Another factor that would support the habitability hypothesis on super-Earths is the feature of plate tectonics introduced previously: as stated since [Walker et al., 1981], a planetary surface that reshapes itself by subduction is very rich in resources and elements that represent the basis of biomolecules, such as carbon C. In [Nakajima et al., 2026] also a new model for the sustainability of a planetary magnetic field on super-Earths is presented: this would make the possibility of life on them more than a mere hypothesis.

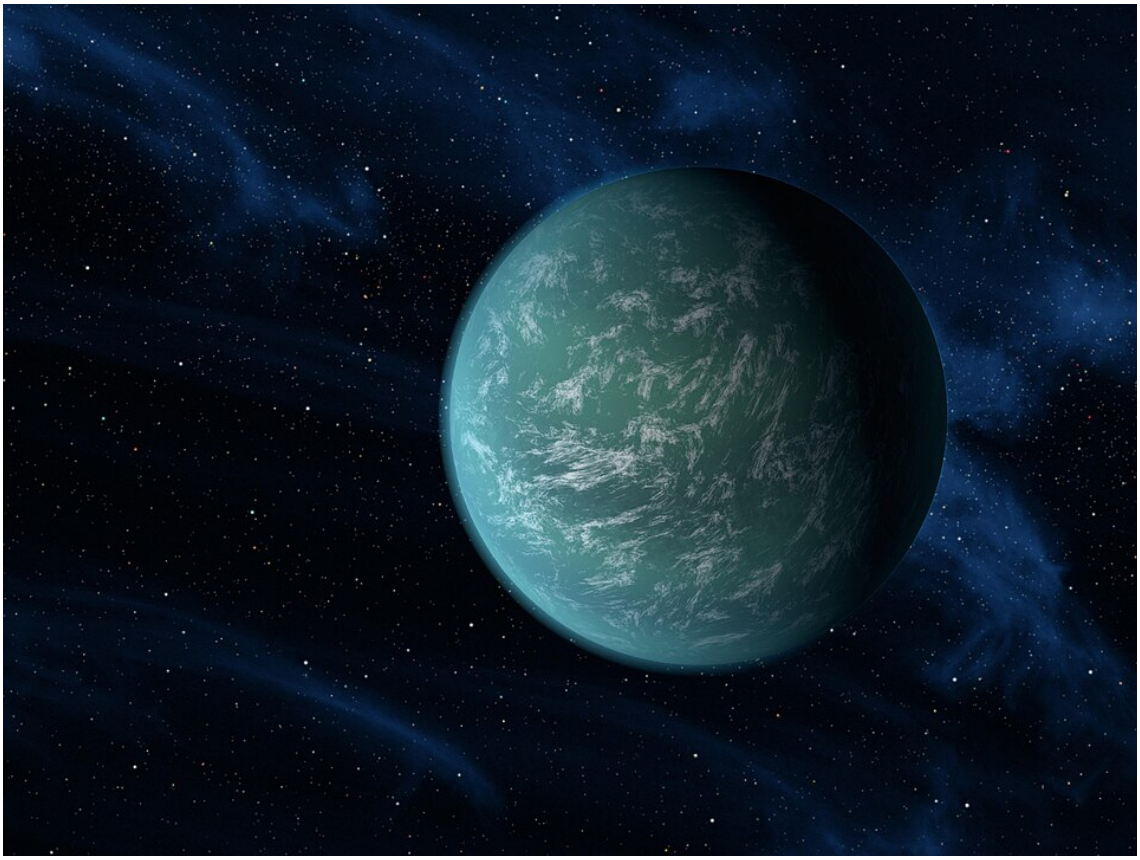

Figure 1.3: *Graphical representation of Kepler-22 b, a super-Earth with size less than* 9 *Earth masses discovered in 2009. It orbits around Kepler-22, a star smaller than our Sun, at* 620 *light years far from the Earth. Kepler-22 b is located in the habitable zone of Kepler-22 stellar system, suggesting a high biological potential. NASA/JPL - Caltech.*

3 Aim of the thesis

In our Solar System there are no super-Earths, so it is impossible to directly study their interior through gravity data or properties of surface materials. The only available approach is by applying theoretical models based on Earth-like internal differentiation, since their observational constraints have a general poor accuracy with respect to Solar System bodies. In this sense, the Earth will not be considered just as a benchmark planet but it will be considered as the lowest mass limit of the super-Earth planetary class, representing their geophysical global properties on smaller scale.

The above-mentioned definition does not include any specific requirements for the compositional nature of a super-Earth: it could be made of gases or rocky materials, or even a combination of both. This opens various possibilities for their physical modeling: in [Wagner et al., 2012], for example, the authors reconstructed the interior of rocky Super-Earths using thermal-state data, while in [Kellermann et al., 2018] a model for fully fluid super-Earths was presented.
Once the interior model is established, the next choice falls on the method to confirm its validity. One of the most relevant approaches that is possible to carry out is the study of planetary deformability. The internal mass distribution of a planet - the source of its gravity field - can be inferred through the evaluation of Love numbers: these dimensionless coefficients indicate the deformability of a celestial body in response to different perturbations [Love, 1909, Love, 1911]. They can be measured by employing various techniques in order to establish constraints on the possible planetary interiors. For exoplanets, some of these techniques are the same used for their detection: for example, the transit method takes advantage of the fall in the observed brightness profile of a star to detect an exoplanet transiting in front of it; a tidally-deformed planet generates anomalies in the standard transit light curve associated with the undeformed planet, and this can be exploited to measure its tidal Love numbers [Correia, 2014, Barros et al., 2022]. New possibilities of measuring tidal Love numbers of exoplanets consider also their orbital precession [Ragozzine and Wolf, 2009]. Focusing on the planetary bodies in our Solar System, their Love numbers have been measured thanks to altimetry and Doppler tracking of orbit variations from the data of past space missions [Konopliv and Yoder, 1996, Goossens and Matsumoto, 2008, Mazarico et al., 2014, Thor et al., 2021].

Nevertheless, it is possible to obtain estimates of Love numbers also employing numerical methods. The numerical evaluation of Love numbers has already been applied to many planetary classes, from the Earth [Longman, 1966, Saito, 1974, Wu and Peltier, 1982] to other solar bodies [Gavrilov and Zharkov, 1977, Sohl et al., 2003, Petricca et al., 2022]. Since exoplanets have been discovered in our galaxy, Love numbers have been estimated for some of their models too [Kramm et al., 2012, van Dijk and Miguel, 2025]. These coefficients also have cosmological importance in studying the deformability of black holes and neutron stars in both classical and relativistic formulations, proving their cross-disciplinarity [Hinderer, 2008, Binnington and Poisson, 2009, Brustein and Sherf, 2022, Rodríguez et al., 2026]. Obtaining an estimate of Love numbers, by applying numerical methods to different interior models, represents the basis for their comparison with future measured datasets. Exoplanetary Love numbers will allow us to confirm or reevaluate the proposed interior models for these remote bodies.

As we have already introduced, there are many works in the past literature that have studied the deformability of terrestrial planets and other kinds of celestial bodies through Love numbers evaluation, proposing many models for each of them [Zhang, 1992]. The motivations that guide this thesis are the same, but focusing on Earth-like exoplanets. I have studied the case of rocky super-Earths in a range from two to eight Earth masses, adapting different Earth-like interior models to higher pressure regimes and evaluating Love numbers associated to different perturbation sources. A new estimation of the Love numbers of the Earth is carried out as well. To the knowledge of the supervisors and the author, this is the first work having the aim of evaluating Love numbers for rocky super-Earths using different interior models and comparing them with the Earth's ones. In *Chapter 2* I review the theory of planetary deformability, from the basic physical equations to the ODEs system that fully describes the problem in three cases: compressible solid layers, incompressible solid layers, and fluid layers. In *Chapter 3* I show the numerical code and setup that I have developed to evaluate Love numbers, whose results are reported and discussed in *Chapter 4*. Finally, I summarize the conclusions in *Chapter 5*, proposing some possible improvements for the future.

Chapter 2

Theory of planetary deformation

In this Chapter the theory that underlies the physics of planetary deformability is presented. We discuss how to obtain the ordinary differential equations system that governs the physics of planetary deformations starting from basic physical relations. This procedure is illustrated for three possible kinds of planetary layer: a compressible solid layer, an incompressible solid layer, and an inviscid fluid layer. In the last Sections we discuss the surface boundary conditions that have to be imposed to reproduce different types of perturbations and we explain how Love numbers describe the planetary response to perturbing forces.
The main contents of the following discussion are based on the previous works of all the geophysicists that developed the topic along the decades, starting from [Love, 1909], each one reported in the most appropriate part of the Chapter. Nevertheless, the general structure of the theory mainly follows [Wu and Peltier, 1982] and [Spada et al., 2025].
Except for where explicitly written, all the theoretical discussion is presented in spherical coordinates (see Appendix A) and is valid for planetary layers assumed in elastic rheology.

1 Compressible homogeneous elastic body

The most general case to consider is the one of a compressible planetary body, *i.e.* a planet whose materials can spatially rearrange modifying their density in response to a volume change.

1.1 Governing laws

Consider a spherically symmetric, self-gravitating, non-rotating, elastic body which is homogeneous and compressible; it could be a spherical shell or a full sphere, for example.

In an unperturbed state, it is fully described by the hydrostatic equation:

$$\vec{\nabla} p_0 = -\rho_0 g_0 \widehat{r}\,, \tag{2.1}$$

where p_0 is pressure, ρ_0 is density, g_0 is gravity acceleration and $\widehat{r}$ is the radial unit vector, and by Poisson's equation for the gravitational potential:

$$\nabla^2 \phi_0 = 4\pi G \rho_0\,, \tag{2.2}$$

where ϕ_0 is gravitational potential and $G = 6.67 \cdot 10^{-11}\,\dfrac{N \cdot m^2}{kg^2}$ is the universal gravitational constant.
The gravity acceleration is:

$$g_0(r) = \frac{G M_{in}(r)}{r^2}\,, \tag{2.3}$$

where $M_{in}(r)$ is the mass included inside a sphere of radius r, so that in spherical symmetry:

$$M_{in}(r) = \frac{4}{3}\pi r^3 \rho(r)\,. \tag{2.4}$$

In such an unperturbed state, there is no deformation of the body. In fact, deformations occur only in the presence of a perturbing source: in the case of a planetary body, it could be another celestial body, a mass load located on its surface or a system of shear forces acting on it.
In the perturbed state, the density shows a variation equal to $\rho_1(r,\gamma)$ and the gravitational potential shows a variation equal to $\phi_1(r,\gamma)$, depending both on radial r and angular position $\gamma = (\theta, \varphi)$, where θ is colatitude and φ is longitude. In addition to these, each point of the body is also subject to a vector displacement $\vec{u}(r,\gamma)$ and a stress field tensor $\tau(r,\gamma)$.

The governing physical laws of the perturbed body are the following:

- *Equation of momentum conservation*

$$\vec{\nabla}\tau - \rho_0 \vec{\nabla}\phi_1 - \vec{\nabla}(\rho_0 g_0 \vec{u} \cdot \widehat{r}) - \rho_1 g_0 \widehat{r} = 0\,, \tag{2.5}$$

  analogous to Eq. (5.32) in [Backus, 1967] in the case of no time dependence and Eq. (4a) in [Wu and Peltier, 1982].

- *Poisson's equation for gravitational potential variation*

$$\nabla^2 \phi_1 = 4\pi G \rho_1\,, \tag{2.6}$$

  analogous to Eq. (5.4) in [Backus, 1967] and Eq. (4b) in [Wu and Peltier, 1982].

- *Linearized continuity equation*

$$\rho_1 = -\rho_0 \vec{\nabla} \cdot \vec{u} - \vec{u}\, \frac{\partial \rho_0}{\partial r}\, \widehat{r}\,, \tag{2.7}$$

analogous to Eq. (5.31) in [Backus, 1967] and Eq. (4c) in [Wu and Peltier, 1982].

- *Constitutive law for elastic bodies*

$$\tau_{ij} = \lambda \epsilon_{kk} \delta_{ij} + 2\mu \epsilon_{ij}\,, \tag{2.8}$$

where λ is Lamé's first parameter, μ is shear modulus (or Lamé's second parameter) and ϵ_{ij} is the infinitesimal strain tensor, defined as:

$$\epsilon_{ij} = \frac{1}{2}\left(\frac{\partial u_i}{\partial x_j} + \frac{\partial u_j}{\partial x_i}\right), \tag{2.9}$$

where x_i , $i = 1, 2, 3$ indicates the position in a given coordinate system. From this definition it follows that: $\epsilon_{kk} = \vec{\nabla} \cdot \vec{u}$.
In isotropic approximation, Lamé's parameters are related through the bulk modulus K as:

$$K = \lambda + \frac{2}{3}\mu\,. \tag{2.10}$$

If the body is homogeneous: $\rho_0 = const.$, then Eq. (2.7) becomes:

$$\rho_1 = -\rho_0 \vec{\nabla} \cdot \vec{u}\,, \tag{2.11}$$

so that density varies only due to volume changes of the material.
It follows from Eq. (2.11) that Eqs. (2.5) and (2.6) can be rewritten as:

$$\vec{\nabla}\tau - \rho_0 \vec{\nabla}\phi_1 - \vec{\nabla}(\rho_0 g_0 \vec{u} \cdot \widehat{r}) + \rho_0 g_0 (\vec{\nabla} \cdot \vec{u})\widehat{r} = 0\,, \tag{2.12}$$

$$\nabla^2 \phi_1 = -4\pi G \rho_0 (\vec{\nabla} \cdot \vec{u})\,. \tag{2.13}$$

Rewriting Eq. (2.8):

$$\tau_{ij} = \lambda \epsilon_{kk} \delta_{ij} + 2\mu \epsilon_{ij} = \lambda(\vec{\nabla} \cdot \vec{u})\delta_{ij} + 2\mu \epsilon_{ij}\,, \tag{2.14}$$

and taking the derivative gives:

$$\begin{aligned}
\frac{\partial \tau_{ij}}{\partial x_j} &= \lambda \frac{\partial}{\partial x_i}(\vec{\nabla} \cdot \vec{u}) + 2\mu \frac{\partial \epsilon_{ij}}{\partial x_j} = \\
&= \lambda \frac{\partial}{\partial x_i}(\vec{\nabla} \cdot \vec{u}) + \mu \left(\frac{\partial}{\partial x_j}\frac{\partial u_i}{\partial x_j} + \frac{\partial}{\partial x_j}\frac{\partial u_j}{\partial x_i} \right) = \\
&= \lambda \frac{\partial}{\partial x_i}\frac{\partial u_k}{\partial x_k} + \mu \left(\frac{\partial^2 u_i}{\partial x_j^2} + \frac{\partial}{\partial x_i}\frac{\partial u_j}{\partial x_j} \right) = \\
&= (\lambda + \mu) \frac{\partial}{\partial x_i}\frac{\partial u_k}{\partial x_k} + \mu \frac{\partial^2 u_i}{\partial x_j^2}\,, \qquad (2.15)
\end{aligned}$$

that in vector form becomes:

$$\vec{\nabla}\tau = (\lambda + \mu)\vec{\nabla}(\vec{\nabla} \cdot \vec{u}) + \mu \nabla^2 \vec{u}\,. \qquad (2.16)$$

Inserting Eq. (2.16) into (2.12), we obtain the last governing law in form:

$$(\lambda + \mu)\vec{\nabla}(\vec{\nabla} \cdot \vec{u}) + \mu \nabla^2 \vec{u} - \rho_0 \vec{\nabla}\phi_1 - \vec{\nabla}(\rho_0 g_0 \vec{u} \cdot \hat{r}) + \rho_0 g_0 (\vec{\nabla} \cdot \vec{u})\hat{r} = 0\,, \qquad (2.17)$$

where the first term at the left hand side can be rewritten as:

$$(\lambda + \mu)\vec{\nabla}(\vec{\nabla} \cdot \vec{u}) = (\lambda + 2\mu)\vec{\nabla}(\vec{\nabla} \cdot \vec{u}) - \mu\vec{\nabla}(\vec{\nabla} \cdot \vec{u})\,, \qquad (2.18)$$

so that:

$$(\lambda + 2\mu)\vec{\nabla}(\vec{\nabla} \cdot \vec{u}) - \mu\vec{\nabla}(\vec{\nabla} \cdot \vec{u}) + \mu \nabla^2 \vec{u} - \rho_0 \vec{\nabla}\phi_1 - \vec{\nabla}(\rho_0 g_0 \vec{u} \cdot \hat{r}) + \rho_0 g_0 (\vec{\nabla} \cdot \vec{u})\hat{r} = 0\,, \qquad (2.19)$$

finally obtaining:

$$\vec{\nabla}\left[(\lambda + 2\mu)\vec{\nabla} \cdot \vec{u} - \rho_0\phi_1 - \rho_0 g_0 \vec{u} \cdot \hat{r}\right] + \rho_0 g_0 (\vec{\nabla} \cdot \vec{u})\hat{r} - \mu \vec{\nabla} \times \vec{\nabla} \times \vec{u} = 0\,, \qquad (2.20)$$

where we have used the well-known vector identity:

$$\vec{\nabla} \times \vec{\nabla} \times \vec{x} = \vec{\nabla}(\vec{\nabla} \cdot \vec{x}) - \nabla^2 \vec{x}\,. \qquad (2.21)$$

In synthesis, the governing laws of deformation of a compressible homogeneous elastic body are Eqs. (2.11), (2.13), (2.20) and the constitutive law for elastic bodies (2.8).
The unknown variables of the problem are the three components of the vector displacement (u_r, u_θ, u_φ), the gravitational potential variation ϕ_1 and the volume change $\vec{\nabla} \cdot \vec{u}$.

1.2 Obtaining the problem ODEs system

Thanks to the spherical symmetry of the body and the axial symmetry of the boundary conditions that we will introduce later, we can assume $\vec{u}$ as an axially symmetric vector depending only on radius r and colatitude θ, which allows an expansion as:

$$\vec{u} = \sum_n \left(uP\,\hat{r} + vP_\theta\,\hat{\theta} \right) , \tag{2.22}$$

where $u = u(r)$ and $v = v(r)$ are radial functions acting as polynomial coefficients and $P = P_n(\cos\theta)$ is the Legendre polynomial of harmonic degree n. The sum has to be considered extended up to a maximum harmonic degree n_{max} that can ideally be infinite. We use the notation P_θ to indicate the first derivative of P with respect to colatitude and $P_{\theta\theta}$ to indicate the second derivative of P with respect to colatitude.
Legendre's differential equation in angular form is valid too:

$$P_{\theta\theta} + \cot\theta\,P_\theta = -n(n+1)P\,. \tag{2.23}$$

A complete discussion on the topic of harmonic decomposition of functions defined on a spherical surface should include complex spherical harmonics Y_{nm} as the main element of decomposition for each component of the functions, where:

$$Y_{nm}(\theta,\varphi) = c_{nm}\,P_{nm}(\cos\theta)\,e^{im\varphi}\,, \tag{2.24}$$

where c_{nm} is a normalization factor, $n = 0, 1, 2, ...$ is the harmonic degree, and $m = 0, 1, ..., n$ is the order. However, for the specific case of spherically symmetric bodies with boundary conditions such as those we treat here, there is no dependence on longitude φ and using Legendre polynomials is formally equivalent to using complex spherical harmonics of order zero.

We can decompose all the other unknown variables of the problem with the same approach and notation used in Eq. (2.22) as follows:

$$u_r = \sum_n u\,P\,, \tag{2.25}$$

$$u_\theta = \sum_n v\,P_\theta\,, \tag{2.26}$$

$$u_\varphi = 0\,, \tag{2.27}$$

$$\phi_1 = \sum_n \phi\,P\,, \tag{2.28}$$

$$\vec{\nabla}\cdot\vec{u} = \sum_n \chi\,P\,, \tag{2.29}$$

where $\phi = \phi(r)$ and $\chi = \chi(r)$ are radial functions acting as polynomial coefficients of the gravitational potential variation and the volume change, respectively.
The relevant stress field components can also be harmonically decomposed as:

$$\tau_{rr} = \sum_n T_r \, P \,, \tag{2.30}$$

$$\tau_{r\theta} = \sum_n T_\theta \, P_\theta \,, \tag{2.31}$$

where $T_r = T_r(r)$ and $T_\theta = T_\theta(r)$ are radial functions acting as polynomial coefficients of the radial stress τ_{rr} and the tangential stress $\tau_{r\theta}$. We will not consider the other components of the stress tensor because they are not necessary to describe the deformation of a spherically symmetric body.

Before proceeding to obtain the Ordinary Differential Equations (ODEs) that define the problem of planetary deformability, we need to obtain the relations between T_r and T_θ and the other radial functions.
From the harmonic decomposition of u_r and u_θ in Eqs. (2.25), (2.26) and the null value of u_φ, applying Eqs. (A.19) and denoting with the prime the derivative with respect to r, we have:

$$\epsilon_{rr} = \frac{\partial u}{\partial r} P = u' P \,, \tag{2.32}$$

$$\epsilon_{\theta\theta} = \frac{v}{r}\frac{\partial P_\theta}{\partial \theta} + \frac{1}{r}\, uP = \frac{v}{r} P_{\theta\theta} + \frac{1}{r}\, uP \,, \tag{2.33}$$

$$\epsilon_{\varphi\varphi} = \frac{v}{r} P_\theta \cot\theta + \frac{u}{r} P \,, \tag{2.34}$$

$$\epsilon_{r\theta} = \frac{\partial v}{\partial r} P_\theta - \frac{v}{r} P_\theta + \frac{u}{r}\frac{\partial P}{\partial \theta} = v' P_\theta - \frac{v}{r} P_\theta + \frac{u}{r} P_\theta \,. \tag{2.35}$$

If we consider the radial and tangential components of stress tensor from Eqs. (A.20), we have:

$$\tau_{r\theta} = \mu\, \epsilon_{r\theta} = \mu \left(v' - \frac{v}{r} + \frac{u}{r} \right) P_\theta \,, \tag{2.36}$$

so that, considering a harmonic decomposition for $\tau_{r\theta}$ as in Eq. (2.31), it leads to:

$$T_\theta = \mu \left(v' - \frac{v}{r} + \frac{u}{r} \right) . \tag{2.37}$$

For radial component τ_{rr}:

$$\begin{aligned}
\tau_{rr} &= (\lambda+2\mu)\epsilon_{rr}+\lambda(\epsilon_{\theta\theta}+\epsilon_{\varphi\varphi}) = \\
&= (\lambda+2\mu)u'P+\lambda\left(\frac{v}{r}P_{\theta\theta}+\frac{u}{r}P+\frac{v}{r}P_\theta\cot\theta+\frac{u}{r}P\right) = \\
&= (\lambda+2\mu)u'P+\frac{\lambda}{r}\left(\,2uP+(P_{\theta\theta}\,+P_\theta\cot\theta)\,v\,\right) = \\
&= (\lambda+2\mu)u'P+\frac{\lambda}{r}(\,2u-n(n+1)\,v)P\,,
\end{aligned} \tag{2.38}$$

where we have used Eq. (2.23).
If we consider a harmonic decomposition for τ_{rr} as in Eq. (2.30), it leads to:

$$T_r = (\lambda+2\mu)u' \,+\frac{\lambda}{r}(\,2u-n(n+1)\,v)\,. \tag{2.39}$$

T_r is also related to χ through Eq. (2.44) - that we will see later - as follows:

$$\begin{aligned}
\chi &= u'+\frac{2}{r}u-\frac{n(n+1)}{r}v \\
\lambda\chi &= \lambda u'+\frac{\lambda}{r}\,(\,2u-n(n+1)\,v) \\
\lambda\chi+2\mu u' &= (\lambda+2\mu)u'+\frac{\lambda}{r}\,(\,2u-n(n+1)\,v\,)\ ,
\end{aligned} \tag{2.40}$$

so that:

$$T_r = \lambda\chi+2\mu u'\,. \tag{2.41}$$

Starting from the equations that we have introduced before, we can obtain the ODEs system of the problem as follows.

1. *Continuity equation*
   Inserting the harmonic decomposition of volume change $\vec{\nabla}\cdot\vec{u}$ into Eq. (2.11), we have:
   $$\rho_1 = -\rho_0\sum_n \chi\,P\,. \tag{2.42}$$
   Using Eqs. (A.10) and (2.23) we can also obtain another harmonic decomposition

of $\vec{\nabla} \cdot \vec{u}$ in form:

$$\begin{aligned}
\vec{\nabla} \cdot \vec{u} &= \vec{\nabla} \cdot \left(\sum_n u\, P\, \widehat{r} + v\, P_\theta\, \widehat{\theta} \right) = \\
&= \sum_n \left[\frac{\partial u}{\partial r} P + \frac{2u}{r} P + \frac{v}{r} (\cot\theta\, P_\theta + P_{\theta\theta}) \right] = \\
&= \sum_n \left[\left(u' + \frac{2u}{r} \right) P + \frac{v}{r} (-n(n+1)) P \right] = \\
&= \sum_n \left(u' + \frac{2u}{r} - \frac{n(n+1)}{r}\, v \right) P\,. \qquad (2.43)
\end{aligned}$$

From a comparison with Eq. (2.29) we have:

$$\chi = u' + \frac{2u}{r} - \frac{n(n+1)}{r}\, v\,. \qquad (2.44)$$

2. *Poisson's equation for gravitational potential variation*
Inserting the harmonic decomposition of volume change $\vec{\nabla} \cdot \vec{u}$ into Eq. (2.13), we have:

$$\nabla^2 \phi_1 = -4\pi G \rho_0 \sum_n \chi\, P\,. \qquad (2.45)$$

If we fully write the laplacian of ϕ_1 using Eqs. (A.13) and (2.23):

$$\begin{aligned}
\nabla^2 \phi_1 &= \nabla^2 \sum_n \phi\, P = \\
&= \sum_n \left[\frac{\partial^2 \phi}{\partial r^2} P + \frac{2}{r} \frac{\partial \phi}{\partial r} P + \frac{1}{r^2} \phi\, P_{\theta\theta} + \frac{\cot\theta}{r^2} \phi\, P_\theta \right] = \\
&= \sum_n \left[\phi'' P + \frac{2}{r} \phi' P + \frac{\phi}{r^2} (-n(n+1)) P \right] = \\
&= \sum_n \left(\phi'' + \frac{2}{r} \phi' - \frac{n(n+1)}{r^2} \phi \right) P\,. \qquad (2.46)
\end{aligned}$$

From a comparison with Eq. (2.45), we have:

$$\phi'' + \frac{2}{r} \phi' - \frac{n(n+1)}{r^2} \phi = -4\pi G \rho_0 \chi\,, \qquad (2.47)$$

and defining a new variable Q as previously done in [Wu and Peltier, 1982], [Vermeersen et al., 1996] and other works as:

$$Q = \phi' + \frac{n+1}{r} \phi + 4\pi G \rho_0 u\,, \qquad (2.48)$$

then:

$$\phi' = -4\pi G\rho_0 u - \frac{n+1}{r}\phi + Q\,. \tag{2.49}$$

Introducing Q is fundamental for the problem so that it becomes the sixth variable that describes the deformability of the body along with the harmonic coefficients-like functions introduced before. Q admits various formulations and it could be found in different forms depending on the author of the paper. This variable is sometimes referred to as "potential traction".

3. *Q definition*
   If we differentiate Eq. (2.48) with respect to r we have:

$$\begin{aligned}
Q' &= \phi'' + \frac{n+1}{r}\phi' - \frac{n+1}{r^2}\phi + 4\pi G\rho_0 u' = \\
&= -4\pi G\rho_0\chi + \frac{n-1}{r}\phi' + \frac{(n+1)(n-1)}{r^2}\phi + 4\pi G\rho_0 u' = \\
&= -4\pi G\rho_0\chi + \frac{n-1}{r}Q - 4\pi G\rho_0\frac{n-1}{r}\,u + 4\pi G\rho_0 u' = \\
&= -4\pi G\rho_0\frac{2u}{r} + 4\pi G\rho_0\frac{n(n+1)}{r}v + \frac{n-1}{r}Q - 4\pi G\rho_0\frac{n-1}{r}\,u\,, \quad (2.50)
\end{aligned}$$

   where we have used in order Eqs. (2.47), (2.48) and (2.44), and finally:

$$Q' = -4\pi G\rho_0\frac{n+1}{r}\,u + 4\pi G\rho_0\frac{n(n+1)}{r}\,v + \frac{n-1}{r}Q\,. \tag{2.51}$$

4. *Equation of momentum conservation*
   Starting from Eq. (2.20) that we recall here below:

$$\vec{\nabla}\left[(\lambda+2\mu)\vec{\nabla}\cdot\vec{u} - \rho_0\phi_1 - \rho_0 g_0\vec{u}\cdot\hat{r}\right] + \rho_0 g_0(\vec{\nabla}\cdot\vec{u})\hat{r} - \mu\vec{\nabla}\times\vec{\nabla}\times\vec{u} = 0\,, \tag{2.52}$$

   we can apply harmonic decompositions (2.22), (2.28) and (2.29) to its terms:

$$\begin{aligned}
&\vec{\nabla}\left[(\lambda+2\mu)\vec{\nabla}\cdot\vec{u} - \rho_0\phi_1 - \rho_0 g_0\vec{u}\cdot\hat{r}\right] = \\
= \; &\vec{\nabla}\left[(\lambda+2\mu)\sum_n \chi\,P - \rho_0\sum_n \phi\,P - \rho_0 g_0\sum_n\left(u\,P\,\hat{r} + v\,P_\theta\,\hat{\theta}\right)\cdot\hat{r}\right] = \\
= \; &\vec{\nabla}\left[\sum_n\left((\lambda+2\mu)\chi - \rho_0\phi - \rho_0 g_0 u\right)P\right], \quad (2.53)
\end{aligned}$$

$$\rho_0 g_0 (\vec{\nabla}\cdot\vec{u})\widehat{r} = \rho_0 g_0 \sum_n \chi\, P\, \widehat{r}\,, \tag{2.54}$$

$$\begin{aligned}
\vec{\nabla}\times\vec{u} &= \vec{\nabla}\times\left(\sum_n \left(u\,P\,\widehat{r} + v\,P_\theta\,\widehat{\theta}\right)\right) = \\
&= \sum_n \frac{1}{r}\left(\frac{\partial}{\partial r}(r\,v\,P_\theta) - \frac{\partial}{\partial\theta}(u\,P)\right)\widehat{\varphi} = \\
&= \sum_n \frac{1}{r}\left(v\,P_\theta + r\,v' P_\theta - u\,P_\theta\right)\widehat{\varphi} = \\
&= \sum_n \left(\frac{v}{r} + v' - \frac{u}{r}\right) P_\theta\,\widehat{\varphi}\,,
\end{aligned} \tag{2.55}$$

where we have used Eqs. (A.15).
If we define a new variable H as:

$$H = v' + \frac{v}{r} - \frac{u}{r}\,, \tag{2.56}$$

we can decompose $\vec{\nabla}\times\vec{u}$ in form:

$$\vec{\nabla}\times\vec{u} = \sum_n H P_\theta\,\widehat{\varphi}\,. \tag{2.57}$$

The last term becomes:

$$\begin{aligned}
\vec{\nabla}\times\vec{\nabla}\times\vec{u} &= \vec{\nabla}\times\left(\sum_n H P_\theta\,\widehat{\varphi}\right) = \\
&= \sum_n \left[\frac{1}{r\sin\theta}\left(\frac{\partial}{\partial\theta}(H P_\theta \sin\theta)\right)\widehat{r} + \frac{1}{r}\left(-\frac{\partial}{\partial r}(r H P_\theta)\right)\widehat{\theta}\right] = \\
&= \sum_n \left[\frac{H}{r\sin\theta}(P_{\theta\theta}\sin\theta + P_\theta\cos\theta)\,\widehat{r} - \frac{1}{r}(H + rH')\,P_\theta\,\widehat{\theta}\right] = \\
&= \sum_n \left[\frac{H}{r}(P_{\theta\theta} + P_\theta\cot\theta)\,\widehat{r} - \frac{1}{r}(H + rH')\,P_\theta\,\widehat{\theta}\right] = \\
&= \sum_n \left[-\frac{H}{r}n(n+1)P\,\widehat{r} - \left(\frac{H}{r} + H'\right)P_\theta\,\widehat{\theta}\right] = \\
&= \sum_n \left(-\frac{n(n+1)}{r}HP\,\widehat{r} - \frac{1}{r}(rH)'\,P_\theta\,\widehat{\theta}\right)\,.
\end{aligned} \tag{2.58}$$

Finally we can rewrite Eq. (2.52) in form:

$$\sum_n \vec{\nabla}\left[((\lambda+2\mu)\chi-\rho_0\phi-\rho_0 g_0 u)\, P\right]+\rho_0 g_0 \chi\, P\,\widehat{r}+\mu\left(\frac{n(n+1)}{r} H P\,\widehat{r}+\frac{1}{r}(rH)'\, P_\theta\,\widehat{\theta}\right)=0\,. \tag{2.59}$$

5. $\widehat{r}$ *component of equation of momentum conservation*
   Consider only the $\widehat{r}$ terms of Eq. (2.59):

$$\vec{\nabla}_r\left[((\lambda+2\mu)\chi-\rho_0\phi-\rho_0 g_0 u)\, P\right]+\rho_0 g_0 \chi\, P\,\widehat{r}+\mu\frac{n(n+1)}{r} H P\,\widehat{r}=0\,, \tag{2.60}$$

then working on radial scalar values we have:

$$(\lambda+2\mu)\chi'-\rho_0\phi'-\rho_0(g_0 u)'+\rho_0 g_0\chi+\mu\frac{n(n+1)}{r}H=0\,. \tag{2.61}$$

χ' can be obtained differentiating Eq. (2.44) with respect to r:

$$\begin{aligned}\chi' &= u''+\frac{\partial}{\partial r}\left(\frac{2u}{r}\right)-\frac{\partial}{\partial r}\left(\frac{n(n+1)}{r}v\right)= \\ &= u''+\frac{2}{r}u'-\frac{2}{r^2}u-\frac{n(n+1)}{r}v'+\frac{n(n+1)}{r^2}v\,,\end{aligned} \tag{2.62}$$

hence:

$$\begin{aligned}(\lambda+2\mu)\chi' &= \lambda\chi'+2\mu\left(u''+\frac{2}{r}u'-\frac{2}{r^2}u-\frac{n(n+1)}{r}v'+\frac{n(n+1)}{r^2}v\right)= \\ &= (\lambda\chi+2\mu u')'+\frac{4\mu}{r}\left(u'-\frac{u}{r}\right)-\frac{2\mu n(n+1)}{r}\left(v'-\frac{v}{r}\right)\,.\end{aligned} \tag{2.63}$$

Remembering Eq. (2.41) we finally obtain:

$$T_r'+\frac{4\mu}{r}\left(u'-\frac{u}{r}\right)-\frac{2\mu n(n+1)}{r}\left(v'-\frac{v}{r}\right)-\rho_0\phi'-\rho_0(g_0u)'+\rho_0 g_0\chi+\mu\frac{n(n+1)}{r}H=0\,, \tag{2.64}$$

and using the H definition (2.56) we can write the fifth starting ODE as:

$$T_r'-\rho_0\phi'-\rho_0(g_0u)'+\rho_0 g_0\chi+\frac{4\mu}{r}\left(u'-\frac{u}{r}\right)+\frac{\mu n(n+1)}{r}\left(\frac{3v}{r}-\frac{u}{r}-v'\right)=0\,. \tag{2.65}$$

6. $\widehat{\theta}$ *component of equation of momentum conservation*
   Consider only the $\widehat{\theta}$ terms of Eq. (2.59):

$$\vec{\nabla}_\theta\left[((\lambda+2\mu)\chi-\rho_0\phi-\rho_0 g_0 u)\, P\right]+\frac{\mu}{r}(rH)'\, P_\theta\,\widehat{\theta}=0\,, \tag{2.66}$$

then working on radial scalar values we have:

$$(\lambda + 2\mu)\chi - \rho_0\phi - \rho_0 g_0 u + \mu(rH)' = 0\,. \tag{2.67}$$

From Eqs. (2.44) and (2.56) we have:

$$\begin{aligned}
&\lambda\chi + 2\mu u' + \frac{4\mu}{r}u - \frac{2\mu n(n+1)}{r}v - \rho_0\phi - \rho_0 g_0 u + \mu(rv' + v - u)' = 0 \\
&\lambda\chi - \rho_0\phi - \rho_0 g_0 u + \mu\left(u' + \frac{4}{r}u - \frac{2n(n+1)}{r}v + rv'' + 2v'\right) = 0\,.
\end{aligned} \tag{2.68}$$

If we differentiate Eq. (2.37) with respect to r we find a new form for rv'' term as:

$$\begin{aligned}
T'_\theta &= \mu\left(v'' - \frac{v'}{r} + \frac{v}{r^2} + \frac{u'}{r} - \frac{u}{r^2}\right) \\
\frac{1}{\mu}r\,T'_\theta &= rv'' - v' + \frac{v}{r} + u' - \frac{u}{r} \\
rv'' &= \frac{1}{\mu}r\,T'_\theta + v' - u' - \frac{v}{r} + \frac{u}{r}\,,
\end{aligned} \tag{2.69}$$

so that Eq. (2.68) becomes:

$$\lambda\chi - \rho_0\phi - \rho_0 g_0 u + rT'_\theta + \mu\left(3v' + \frac{5}{r}u - \frac{2n(n+1)+1}{r}v\right) = 0\,. \tag{2.70}$$

From Eqs. (2.44), (2.49), (2.51), (2.56), (2.65) and (2.70), applying some rearrangements we can reach the final ODEs system of the problem in the (u, v, T_r, T_θ, ϕ, Q) set of unknown radial variables.

- *ODE 1*

  Inserting Eq. (2.44) into T_r relation (2.41) we have:

$$\begin{aligned}
T_r &= \lambda u' + \frac{2\lambda}{r}u - \frac{\lambda n(n+1)}{r}v + 2\mu u' \\
T_r &= (\lambda + 2\mu)u' + \frac{2\lambda}{r}u - \frac{\lambda n(n+1)}{r}v\,,
\end{aligned} \tag{2.71}$$

  hence the first ODE is:

$$u' = -\frac{\lambda}{\lambda + 2\mu}\frac{2}{r}u + \frac{\lambda}{\lambda + 2\mu}\frac{n(n+1)}{r}v + \frac{1}{\lambda + 2\mu}T_r\,. \tag{2.72}$$

- *ODE 2*
  Rearranging Eq. (2.37) in function of v' we obtain the second ODE:

$$v' = -\frac{1}{r}u + \frac{1}{r}v + \frac{1}{\mu}T_\theta\,. \tag{2.73}$$

- *ODE 3*
  The third ODE has already been obtained as Eq. (2.49), that we recall here below:

$$\phi' = -4\pi G\rho_0 u - \frac{n+1}{r}\phi + Q\,. \tag{2.74}$$

- *ODE 4*
  The fourth ODE has already been obtained as Eq. (2.51), that we recall here below:

$$Q' = -4\pi G\rho_0\frac{n+1}{r}\,u + 4\pi G\rho_0\frac{n(n+1)}{r}\,v + \frac{n-1}{r}Q\,. \tag{2.75}$$

- *ODE 5*
  If in Eq. (2.65) we insert in order Eqs. (2.72), (2.73), (2.74), (2.44) and also the differentiation of Eq. (2.3):

$$g_0' = 4\pi G\rho_0 - \frac{2g_0}{r}\,, \tag{2.76}$$

we have:

$$
\begin{aligned}
T_r' &= -4\pi G\rho_0^2\, u - \rho_0 \frac{n+1}{r}\phi + \rho_0 Q + \rho_0(g_0' u + g_0 u') - \rho_0 g_0 \left(u' + \frac{2}{r}u - \frac{n(n+1)}{r}v \right) \\
&\quad - \frac{4\mu}{r}\left(u' - \frac{1}{r}u \right) - \frac{\mu n(n+1)}{r}\left(\frac{3}{r}v - \frac{1}{r}u - v' \right) = \\
&= -\rho_0 \frac{n+1}{r}\phi + \rho_0 Q + \rho_0 \left(-\frac{2g_0}{r}u + g_0 u' \right) - \rho_0 g_0 \left(u' + \frac{2}{r}u - \frac{n(n+1)}{r}v \right) \\
&\quad - \frac{4\mu}{r}\left(u' - \frac{1}{r}u \right) - \frac{\mu n(n+1)}{r}\left(\frac{3}{r}v - \frac{1}{r}u - v' \right) = \\
&= -\rho_0 \frac{n+1}{r}\phi + \rho_0 Q - \frac{2}{r}\rho_0 g_0 u - \rho_0 g_0 \left(\frac{2}{r}u - \frac{n(n+1)}{r}v \right) - \frac{4\mu}{r}\left(u' - \frac{1}{r}u \right) \\
&\quad - \frac{\mu n(n+1)}{r}\left(\frac{3}{r}v - \frac{1}{r}u - v' \right) = \\
&= -\rho_0 \frac{n+1}{r}\phi + \rho_0 Q - \frac{4}{r}\rho_0 g_0 u + \rho_0 g_0 \frac{n(n+1)}{r}v - \frac{4\mu}{r}\left(u' - \frac{1}{r}u \right) \\
&\quad - \frac{\mu n(n+1)}{r}\left(\frac{3}{r}v - \frac{1}{r}u - v' \right) = \\
&= -\rho_0 \frac{n+1}{r}\phi + \rho_0 Q - \frac{4}{r}\rho_0 g_0 u + \rho_0 g_0 \frac{n(n+1)}{r}v \\
&\quad - \frac{4\mu}{r}\left(-\frac{\lambda}{\lambda+2\mu}\frac{2}{r}u + \frac{\lambda}{\lambda+2\mu}\frac{n(n+1)}{r}v + \frac{1}{\lambda+2\mu}T_r - \frac{1}{r}u \right) \\
&\quad - \frac{\mu n(n+1)}{r}\left(\frac{3}{r}v - \frac{1}{r}u + \frac{1}{r}u - \frac{1}{r}v - \frac{1}{\mu}T_\theta \right),
\end{aligned}
\tag{2.77}
$$

and making each unknown variable of the problem explicit:

$$
\begin{aligned}
T_r' &= \left(\frac{4\mu\lambda}{\lambda+2\mu}\frac{2}{r^2} + 4\mu\frac{1}{r^2} - \frac{4}{r}\rho_0 g_0\right) u \\
&\quad + \left(\mu\frac{n(n+1)}{r^2} - \mu\frac{3n(n+1)}{r^2} - \frac{4\mu\lambda}{\lambda+2\mu}\frac{n(n+1)}{r^2} + \rho_0 g_0\frac{n(n+1)}{r}\right) v \\
&\quad - \frac{4\mu}{\lambda+2\mu}\frac{1}{r}T_r + \frac{n(n+1)}{r}T_\theta - \frac{n+1}{r}\rho_0\phi + \rho_0 Q = \\
&= \frac{4}{r}\left(\frac{2\mu\lambda}{\lambda+2\mu}\frac{1}{r} + \mu\frac{1}{r} - \rho_0 g_0\right) u \\
&\quad + \frac{n(n+1)}{r}\left(\mu\frac{1}{r} - 3\mu\frac{1}{r} - \frac{4\mu\lambda}{\lambda+2\mu}\frac{1}{r} + \rho_0 g_0\right) v \\
&\quad - \frac{4\mu}{\lambda+2\mu}\frac{1}{r}T_r + \frac{n(n+1)}{r}T_\theta - \frac{n+1}{r}\rho_0\phi + \rho_0 Q\,, \qquad (2.78)
\end{aligned}
$$

we finally obtain the fifth ODE as:

$$
\begin{aligned}
T_r' &= \frac{4}{r}\left(\frac{\mu}{r}\frac{3\lambda+2\mu}{\lambda+2\mu} - \rho_0 g_0\right) u + \frac{n(n+1)}{r}\left(\rho_0 g_0 - \frac{2\mu}{r}\frac{3\lambda+2\mu}{\lambda+2\mu}\right) v \\
&\quad - \frac{4\mu}{\lambda+2\mu}\frac{1}{r}T_r + \frac{n(n+1)}{r}T_\theta - \frac{n+1}{r}\rho_0\phi + \rho_0 Q\,. \qquad (2.79)
\end{aligned}
$$

- *ODE 6*
  If in Eq. (2.70) we insert Eqs. (2.44), (2.72) and (2.73) we have:

$$
\begin{aligned}
T'_\theta &= -\frac{\lambda}{r}\left(u' + \frac{2}{r}u - \frac{n(n+1)}{r}v\right) + \frac{1}{r}\rho_0\phi + \frac{1}{r}\rho_0 g_0 u \\
&\quad -\frac{\mu}{r}\left(3v' + \frac{5}{r}u - \frac{2n(n+1)+1}{r}v\right) = \\
&= -\frac{\lambda}{r}u' - \frac{2\lambda}{r^2}u + \lambda\frac{n(n+1)}{r^2}v + \frac{1}{r}\rho_0\phi + \frac{1}{r}\rho_0 g_0 u \\
&\quad \frac{3\mu}{r}v' - \frac{5\mu}{r^2}u + \mu\frac{2n(n+1)+1}{r^2}v = \\
&= -\frac{\lambda}{r}\left(-\frac{\lambda}{\lambda+2\mu}\frac{2}{r}u + \frac{\lambda}{\lambda+2\mu}\frac{n(n+1)}{r}v + \frac{1}{\lambda+2\mu}T_r\right) \\
&\quad -\frac{2\lambda}{r^2}u + \lambda\frac{n(n+1)}{r^2}v + \frac{1}{r}\rho_0\phi + \frac{1}{r}\rho_0 g_0 u \\
&\quad -\frac{3\mu}{r}\left(-\frac{1}{r}u + \frac{1}{r}v + \frac{1}{\mu}T_\theta\right) - \frac{5\mu}{r^2}u + \mu\frac{2n(n+1)+1}{r^2}v\,,
\end{aligned}
\tag{2.80}
$$

and making each unknown variable of the problem explicit:

$$
\begin{aligned}
T'_\theta &= \left(\frac{\lambda^2}{\lambda+2\mu}\frac{2}{r^2} - \frac{2\lambda}{r^2} + \frac{1}{r}\rho_0 g_0 + \frac{3\mu}{r^2} - \frac{5\mu}{r^2}\right)u \\
&\quad + \left(-\frac{\lambda^2}{\lambda+2\mu}\frac{n(n+1)}{r^2} + \lambda\frac{n(n+1)}{r^2} - \frac{3\mu}{r^2} + \mu\frac{2n(n+1)+1}{r^2}\right)v \\
&\quad -\frac{\lambda}{\lambda+2\mu}\frac{1}{r}T_r - \frac{3}{r}T_\theta + \frac{1}{r}\rho_0\phi = \\
&= \frac{1}{r}\left(\frac{1}{r}\left(\frac{2\lambda^2}{\lambda+2\mu} - 2\lambda - 2\mu\right) + \rho_0 g_0\right)u \\
&\quad + \frac{1}{r^2}\left(n(n+1)\left(-\frac{\lambda^2}{\lambda+2\mu} + \lambda + 2\mu\right) - 2\mu\right)v \\
&\quad -\frac{\lambda}{\lambda+2\mu}\frac{1}{r}T_r - \frac{3}{r}T_\theta + \frac{1}{r}\rho_0\phi\,,
\end{aligned}
\tag{2.81}
$$

we finally obtain the sixth ODE as:

$$
\begin{aligned}
T_\theta' \;\; &= \;\; \frac{1}{r}\left(\rho_0 g_0 - \frac{2\mu}{r}\frac{3\lambda+2\mu}{\lambda+2\mu}\right)u + \frac{2\mu}{r^2}\left(2n(n+1)\frac{\lambda+\mu}{\lambda+2\mu} - 1\right)v \\
&\quad -\frac{\lambda}{\lambda+2\mu}\frac{1}{r}T_r - \frac{3}{r}T_\theta + \frac{1}{r}\rho_0\phi\,.
\end{aligned}
\tag{2.82}
$$

Summarizing all the ODEs obtained so far:

$$
\begin{cases}
u' = -\dfrac{\lambda}{\lambda+2\mu}\dfrac{2}{r}u + \dfrac{\lambda}{\lambda+2\mu}\dfrac{n(n+1)}{r}v + \dfrac{1}{\lambda+2\mu}T_r \\[2ex]
v' = -\dfrac{1}{r}u + \dfrac{1}{r}v + \dfrac{1}{\mu}T_\theta \\[2ex]
T_r' = \dfrac{4}{r}\left(\dfrac{\mu}{r}\dfrac{3\lambda+2\mu}{\lambda+2\mu} - \rho_0 g_0\right)u + \dfrac{n(n+1)}{r}\left(\rho_0 g_0 - \dfrac{2\mu}{r}\dfrac{3\lambda+2\mu}{\lambda+2\mu}\right)v \\[2ex]
\qquad - \dfrac{4\mu}{\lambda+2\mu}\dfrac{1}{r}T_r + \dfrac{n(n+1)}{r}T_\theta - \dfrac{n+1}{r}\rho_0\phi + \rho_0 Q \\[2ex]
T_\theta' = \dfrac{1}{r}\left(\rho_0 g_0 - \dfrac{2\mu}{r}\dfrac{3\lambda+2\mu}{\lambda+2\mu}\right)u + \dfrac{2\mu}{r^2}\left(2n(n+1)\dfrac{\lambda+\mu}{\lambda+2\mu} - 1\right)v \\[2ex]
\qquad - \dfrac{\lambda}{\lambda+2\mu}\dfrac{1}{r}T_r - \dfrac{3}{r}T_\theta + \dfrac{1}{r}\rho_0\phi \\[2ex]
\phi' = -4\pi G\rho_0 u - \dfrac{n+1}{r}\phi + Q \\[2ex]
Q' = -4\pi G\rho_0\dfrac{n+1}{r}u + 4\pi G\rho_0\dfrac{n(n+1)}{r}v + \dfrac{n-1}{r}Q
\end{cases}
\tag{2.83}
$$

we can also rewrite the problem in vector notation defining a column vector:

$$
\vec{y} = (y_1, y_2, y_3, y_4, y_5, y_6)^T = (u,\, v,\, T_r,\, T_\theta,\, \phi,\, Q)^T\,,
\tag{2.84}
$$

so that we have to solve:

$$
\vec{y}\,' = A\,\vec{y}\,,
\tag{2.85}
$$

where A is the 6×6 coefficients matrix, depending only on body parameters ρ_0, μ, λ, harmonic degree n and radius r:

$$A = \begin{pmatrix} -\dfrac{\lambda}{\lambda+2\mu}\dfrac{2}{r} & \dfrac{\lambda}{\lambda+2\mu}\dfrac{n(n+1)}{r} & \dfrac{1}{\lambda+2\mu} & 0 & 0 & 0 \\ -\dfrac{1}{r} & \dfrac{1}{r} & 0 & \dfrac{1}{\mu} & 0 & 0 \\ \frac{4}{r}\left(\frac{\mu}{r}\frac{3\lambda+2\mu}{\lambda+2\mu} - \rho_0 g_0\right) & \frac{n(n+1)}{r}\left(\rho_0 g_0 - \frac{2\mu}{r}\frac{3\lambda+2\mu}{\lambda+2\mu}\right) & -\dfrac{4\mu}{\lambda+2\mu}\dfrac{1}{r} & \dfrac{n(n+1)}{r} & -\rho_0\dfrac{n+1}{r} & \rho_0 \\ \frac{1}{r}\left(\rho_0 g_0 - \frac{2\mu}{r}\frac{3\lambda+2\mu}{\lambda+2\mu}\right) & \frac{2\mu}{r^2}\left(2n(n+1)\frac{\lambda+\mu}{\lambda+2\mu} - 1\right) & -\dfrac{\lambda}{\lambda+2\mu}\dfrac{1}{r} & -\dfrac{3}{r} & \dfrac{\rho_0}{r} & 0 \\ -4\pi G\rho_0 & 0 & 0 & 0 & -\dfrac{n+1}{r} & 1 \\ -4\pi G\rho_0\dfrac{n+1}{r} & 4\pi G\rho_0\dfrac{n(n+1)}{r} & 0 & 0 & 0 & \dfrac{n-1}{r} \end{pmatrix}. \tag{2.86}$$

This notation, which is traditionally referred to as "y notation", was introduced for the first time by Z. Alterman in [Alterman et al., 1959] and has been used later, with minor but essential modifications, in many other works (the reader is referred to [Spada et al., 2025]). It is important to recall that the ODEs system (2.85) is linear but it is nevertheless characterized by an extraordinary complexity that calls for a very careful approach.

1.3 Starting solutions for numerical integration

To solve problem (2.85) by numerical integration of ODEs (2.83), we need a starting set of solutions.
We can anticipate that the integration will be carried out from the center of the spherical planetary body near $r = 0$ upward to the surface, for stability reasons that were exposed since [Takeuchi and Saito, 1972]. Due to this, the following discussion will focus only on the regular solutions of (2.85) in $r \mapsto 0$ and not on the singular ones, which would introduce infinity values in integration calculations that do not represent the actual physics of the problem.

Consider again Eq. (2.20) and apply the following differential rearrangements to it.

- Applying the curl operator, we have:

$$\rho_0 \vec{\nabla} \times (g_0(\vec{\nabla} \cdot \vec{u})\,\hat{r}) - \mu \vec{\nabla} \times \vec{\nabla} \times \vec{\nabla} \times \vec{u} = 0\,. \tag{2.87}$$

Defining the vector $\vec{\omega} = \vec{\nabla} \times \vec{u}$:

$$\rho_0(\vec{\nabla} \cdot \vec{u})\, \vec{\nabla} \times (g_0\, \hat{r}) + \rho_0(\vec{\nabla}(\vec{\nabla} \cdot \vec{u})) \times (g_0\, \hat{r}) + \mu \nabla^2 \vec{\omega} = 0$$

$$\rho_0(\vec{\nabla} \cdot \vec{u})\, \vec{\nabla} \times (\vec{\nabla}\phi_0) - \rho_0 g_0\, \hat{r} \times (\vec{\nabla}(\vec{\nabla} \cdot \vec{u})) + \mu \nabla^2 \vec{\omega} = 0\,, \tag{2.88}$$

and remembering that the curl of a gradient is null, we finally reach:

$$\frac{\mu}{\rho_0}\nabla^2 \vec{\omega} = g_0\, \hat{r} \times (\vec{\nabla}(\vec{\nabla} \cdot \vec{u}))\,. \tag{2.89}$$

- Applying the divergence operator, we have:

$$\nabla^2 \left[(\lambda + 2\mu)\vec{\nabla} \cdot \vec{u} - \rho_0\phi_1 - \rho_0 g_0 \vec{u} \cdot \hat{r}\right] + \rho_0 \vec{\nabla} \cdot (g_0(\vec{\nabla} \cdot \vec{u})\, \hat{r}) = 0$$

$$\frac{(\lambda + 2\mu)}{\rho_0}\nabla^2(\vec{\nabla} \cdot \vec{u}) - \nabla^2\phi_1 - \nabla^2(g_0\vec{u} \cdot \hat{r}) + \vec{\nabla} \cdot (g_0(\vec{\nabla} \cdot \vec{u})\, \hat{r}) = 0$$

$$\frac{(\lambda + 2\mu)}{\rho_0}\nabla^2(\vec{\nabla} \cdot \vec{u}) + 4\pi G\rho_0\vec{\nabla} \cdot \vec{u} - \nabla^2(g_0\vec{u} \cdot \hat{r}) + \vec{\nabla} \cdot (g_0(\vec{\nabla} \cdot \vec{u})\, \hat{r}) = 0\,. \tag{2.90}$$

We assume that the ratio $\xi = \dfrac{g_0}{r}$ is constant, as presented in [Alterman et al., 1959], [Gilbert and Backus, 1968] and others. In the previous works, this assumption was made in the whole body, while in this case we assume it only at the starting radial location.
Hence:

$$\frac{(\lambda + 2\mu)}{\rho_0}\nabla^2(\vec{\nabla} \cdot \vec{u}) + 4\pi G\rho_0\vec{\nabla} \cdot \vec{u} - \xi\, \nabla^2(\vec{u} \cdot \hat{r}) + \xi\, \vec{\nabla} \cdot ((\vec{\nabla} \cdot \vec{u})\, \hat{r}) = 0\,. \tag{2.91}$$

Consider the last two terms on the right hand side. They are scalar, so their value does not change if we evaluate them in a spherical reference system or in a generic reference system of coordinates x_i, $i = 1, 2, 3$, hence:

$$\begin{aligned}
\nabla^2(\vec{u} \cdot \hat{r}) &= \frac{\partial^2}{\partial x_j^2}(u_i r_i) = \frac{\partial^2 u_i}{\partial x_j^2} r_i + \frac{\partial^2 r_i}{\partial x_j^2} u_i + 2\frac{\partial u_i}{\partial x_j}\frac{\partial r_i}{\partial x_j} = \\
&= \frac{\partial^2 u_i}{\partial x_j^2} r_i + 2\frac{\partial u_i}{\partial x_j}\delta_{ij} = \frac{\partial^2 u_i}{\partial x_j^2} r_i + 2\frac{\partial u_i}{\partial x_i} = \\
&= (\nabla^2\, \vec{u})\hat{r} + 2\, \vec{\nabla} \cdot \vec{u}\,,
\end{aligned} \tag{2.92}$$

$$\begin{aligned}
\vec{\nabla} \cdot ((\vec{\nabla} \cdot \vec{u})\, \hat{r}) &= (\vec{\nabla}(\vec{\nabla} \cdot \vec{u})) \cdot \hat{r} + (\vec{\nabla} \cdot \vec{u})(\vec{\nabla} \cdot \hat{r}) = \\
&= (\vec{\nabla}(\vec{\nabla} \cdot \vec{u})) \cdot \hat{r} + 3\, (\vec{\nabla} \cdot \vec{u}) = \\
&= (\vec{\nabla} \times \vec{\omega}) \cdot \hat{r} + (\nabla^2\vec{u}) \cdot \hat{r} + 3\, (\vec{\nabla} \cdot \vec{u})\,,
\end{aligned} \tag{2.93}$$

where we have used Eq. (2.21).
Inserting Eqs. (2.92) and (2.93) into (2.91) we finally reach:

$$\frac{\lambda + 2\mu}{\rho_0}\nabla^2(\vec{\nabla}\cdot\vec{u}) + (4\pi G\rho_0 + \xi)\vec{\nabla}\cdot\vec{u} + \xi\,\widehat{r}\cdot(\vec{\nabla}\times\vec{\omega}) = 0\,. \tag{2.94}$$

After we have obtained Eqs. (2.89) and (2.94), we can decompose them into harmonic forms as already done with the equations of Subsection 1.2.
Consider Eqs. (2.21), (2.23), (2.58) and (A.7), (A.15), then:

- *Eq. (2.89)*: $\dfrac{\mu}{\rho_0}\nabla^2\vec{\omega} = g_0\,\widehat{r}\times(\vec{\nabla}(\vec{\nabla}\cdot\vec{u}))$

  Decomposing each term as:

$$\begin{aligned}
\nabla^2\vec{\omega} &= -\vec{\nabla}\times\vec{\nabla}\times\vec{\nabla}\times\vec{u} = \\
&= -\vec{\nabla}\times\left(\sum_n\left(-\frac{n(n+1)}{r}HP\,\widehat{r} - \frac{1}{r}(rH)'P_\theta\,\widehat{\theta}\right)\right) = \\
&= \frac{1}{r}\sum_n\left[\frac{\partial}{\partial r}((rH)'P_\theta - \frac{\partial}{\partial\theta}\left(\frac{n(n+1)}{r}HP\right)\right]\widehat{\varphi} = \\
&= \frac{1}{r}\sum_n\left[((rH)'' - \frac{n(n+1)}{r}H\right]P_\theta\,\widehat{\varphi} = \\
&= \frac{1}{r}\sum_n\left[2H' + rH'' - \frac{n(n+1)}{r}H\right]P_\theta\,\widehat{\varphi} = \\
&= \sum_n\left[H'' + \frac{2H'}{r} - \frac{n(n+1)}{r^2}H\right]P_\theta\,\widehat{\varphi}\,,
\end{aligned} \tag{2.95}$$

$$\begin{aligned}
\widehat{r}\times\vec{\nabla}(\vec{\nabla}\cdot\vec{u}) &= \widehat{r}\times\vec{\nabla}\left(\sum_n\chi P\right) = \widehat{r}\times\left(\sum_n\left[\chi' P\,\widehat{r} + \frac{1}{r}\chi P_\theta\,\widehat{\theta}\right]\right) = \\
&= \frac{1}{r}\sum_n\chi P_\theta\,\widehat{\varphi}\,,
\end{aligned} \tag{2.96}$$

  so that:

$$\frac{\mu}{\rho_0}\sum_n\left[H'' + \frac{2H'}{r} - \frac{n(n+1)}{r^2}H\right]P_\theta\,\widehat{\varphi} = \frac{g_0}{r}\sum_n\chi P_\theta\,\widehat{\varphi}\,, \tag{2.97}$$

  and working only on radial scalar values:

$$\frac{\mu}{\rho_0}\left(H'' + \frac{2H'}{r} - \frac{n(n+1)}{r^2}H\right) = \frac{g_0}{r}\chi\,, \tag{2.98}$$

we have:

$$\nabla_r^2 H = \frac{\xi}{v_S^2}\chi\,, \tag{2.99}$$

where we have introduced the speed of S-waves in an elastic medium v_S:

$$v_S = \sqrt{\frac{\mu}{\rho_0}}\,. \tag{2.100}$$

- *Eq. (2.94)*: $\dfrac{\lambda+2\mu}{\rho_0}\nabla^2(\vec{\nabla}\cdot\vec{u}) + (4\pi G\rho_0+\xi)\vec{\nabla}\cdot\vec{u} + \xi\,\hat{r}\cdot(\vec{\nabla}\times\vec{\omega}) = 0$

  Decomposing its terms as:

$$\frac{\lambda+2\mu}{\rho_0}\,\nabla_r^2\left(\sum_n \chi P\right) + (4\pi G\rho_0+\xi)\sum_n \chi P - \xi\,\hat{r}\cdot\sum_n\left(-\frac{n(n+1)}{r}HP\,\hat{r} - \frac{1}{r}(rH)'P_\theta\,\hat{\theta}\right) = 0\,, \tag{2.101}$$

  and working only on radial scalar values:

$$\frac{\lambda+2\mu}{\rho_0}\nabla_r^2\chi + (4\pi G\rho_0+\xi)\chi + \xi\frac{n(n+1)}{r}H = 0\,, \tag{2.102}$$

  we have:

$$(\nabla_r^2+\alpha^2)\chi = \frac{\xi\, n(n+1)}{v_P^2}H\,, \tag{2.103}$$

  where we have introduced the speed of P-waves in an elastic medium v_P:

$$v_P = \sqrt{\frac{\lambda+2\mu}{\rho_0}}\,, \tag{2.104}$$

  and:

$$\alpha^2 = \frac{4\pi G\rho_0+\xi}{v_P^2}\,. \tag{2.105}$$

If we apply the radial laplacian to Eq. (2.103):

$$\nabla_r^2 H = \frac{v_P^2}{\xi\, n(n+1)}\nabla_r^2(\nabla_r^2+\alpha^2)\chi\,, \tag{2.106}$$

and compare this latter with Eq. (2.99):

$$\frac{v_P^2}{\xi\, n(n+1)}\nabla_r^2(\nabla_r^2+\alpha^2)\chi = \frac{\xi}{v_S^2}\chi\,, \tag{2.107}$$

we obtain an equation that is function of only χ:

$$\nabla_r^2(\nabla_r^2+\alpha^2)\chi=\frac{1}{4}\gamma^2\chi\,, \tag{2.108}$$

where:

$$\gamma^2=\frac{4n(n+1)\xi^2}{v_S^2\,v_P^2}\,. \tag{2.109}$$

After some rearrangements, we finally obtain:

$$(\nabla_r^2+k^2)(\nabla_r^2+q^2)\chi=0\,, \tag{2.110}$$

where k and q are wave numbers in form:

$$k^2 = \frac{\alpha^2+\sqrt{\alpha^4+\gamma^2}}{2}\,, \tag{2.111}$$

$$q^2 = \frac{\alpha^2-\sqrt{\alpha^4+\gamma^2}}{2}\,. \tag{2.112}$$

Eq. (2.110) is formally equal to the general: $(\nabla_r^2+p^2)f=0$, that is the radial part of the Helmholtz equation of a function $f=f(pr)$, also called *spherical Bessel differential equation*:

$$(pr)^2\frac{\partial^2}{\partial(pr)^2}f(pr)+2pr\frac{\partial}{\partial(pr)}f(pr)+\left[(pr)^2-n(n+1)\right]f(pr)=0\,. \tag{2.113}$$

The general solution of this class of equations can be written as a linear combination of spherical Bessel functions (see Appendix B):

$$f(pr) = j_n(pr)\,,\ \ regular\ \ in\ \ r=0\,, \tag{2.114}$$

$$f(pr) = y_n(pr)\,,\ \ singular\ \ in\ \ r=0\,, \tag{2.115}$$

hence:

$$\chi(r)=c_1j_n(kr)+c_2j_n(qr)+c_3y_n(kr)+c_4y_n(qr)\,. \tag{2.116}$$

As already presented at the beginning of this Subsection, due to the regularity of planetary deformability problem we will consider only a linear combination of regular spherical Bessel functions j_n as solution of Eq. (2.110):

$$\chi(r)=c_1j_n(kr)+c_2j_n(qr)\,. \tag{2.117}$$

We also have to consider the case of null solution: $\chi=0$, which identically solves Eq. (2.110).

Starting from the different forms of χ, we have to find solutions for all the unknown radial variables (u, v, T_r, T_θ, ϕ, Q) in function of spherical Bessel functions. Each of the three possible solutions for χ is related to a complete set of starting solutions of the problem; the general starting solution of the problem can be obtained as a linear combination of these three starting subsets.

- **Fundamental solutions for $\boldsymbol{\chi = c_1\, j_n(kr)}$**
  Consider χ in form:
  $$\chi(r) = c_1\, j_n(kr)\,. \tag{2.118}$$
  We can find a solution for each unknown variable u, v, T_r, T_θ, ϕ, Q as follows. Note that not all the dependencies on kr of the unknown variables are reported in each passage, while it is done for all the spherical Bessel functions, for clarity.

  1. ϕ
     Inserting (2.118) into the radial component of Eq. (2.45) we have:
     $$\nabla_r^2\,\phi = -4\pi G\rho_0 c_1 j_n(kr)\,, \tag{2.119}$$
     so that we can assume the form: $\phi = A j_n(kr)$, and then using Eq. (B.1) we have:
     $$\begin{aligned}\nabla_r^2\,\phi &= A\left[k^2 j_n''(kr) + \frac{2k}{r} j_n'(kr) - \frac{n(n+1)}{r^2} j_n(kr)\right] = \\ &= \frac{A}{r^2}\left[(kr)^2 j_n''(kr) + 2kr j_n'(kr) - n(n+1) j_n(kr)\right] = \\ &= -Ak^2 j_n(kr)\,. \end{aligned} \tag{2.120}$$
     From the comparison with Eq. (2.119) we have:
     $$A = \frac{4\pi G\rho_0}{k^2} c_1\,, \tag{2.121}$$
     so that the starting solution for ϕ is:
     $$\phi = \frac{4\pi G\rho_0}{k^2} c_1\, j_n(kr)\,. \tag{2.122}$$
  2. u, v
     Inserting (2.118) into Eq. (2.99) we have:
     $$\nabla_r^2 H = \frac{\xi}{v_S^2} c_1\, j_n(kr)\,, \tag{2.123}$$

that is formally equal to Eq. (2.119), so that also the solution for H is in form:

$$H = c_1 C_k \, j_n(kr) \, , \tag{2.124}$$

where:

$$C_k = -\frac{\xi}{v_S^2 \, k^2} \, . \tag{2.125}$$

Starting from Eqs. (2.44), (2.56) and assuming a general form of u, v depending on spherical Bessel functions as:

$$u(r) = A_U \frac{j_n(kr)}{r} + B_U j_n'(kr) \, , \tag{2.126}$$

$$v(r) = A_V \frac{j_n(kr)}{r} + B_V j_n'(kr) \, , \tag{2.127}$$

after some algebra we reach:

$$\begin{aligned} u = {} & \left(\frac{1}{2r} A_U + \frac{kr}{2} \left(\frac{n(n+1)}{(kr)^2} - 1 \right) B_U + \frac{n(n+1)}{2r} A_V + \frac{c_1 r}{2} \right) \quad j_n(kr) \\ & + \left(-\frac{k}{2} A_U + B_U + \frac{n(n+1)}{2} B_V \right) \quad j_n'(kr) \, , \\ v = {} & \left(\frac{1}{2} A_V - kr \left(\frac{n(n+1)}{(kr)^2} - 1 \right) B_V + \frac{1}{r} A_U + c_1 C_k r \right) \quad j_n(kr) \\ & + \left(-k A_V + 2 B_V + B_U \right) \quad j_n'(kr) \, . \end{aligned}$$

If we compare these results with Eqs. (2.126) and (2.127), we can impose a system of four equations in the four unknown variables A_U, B_U, A_V, B_V that, solved after some cumbersome algebra, produces:

$$A_U = -\frac{c_1 C_k n(n+1)}{k^2} \, , \tag{2.128}$$

$$B_U = -\frac{c_1}{k} \, , \tag{2.129}$$

$$A_V = -\frac{1}{k^2} c_1 C_k \, , \tag{2.130}$$

$$B_V = -\frac{c_1 C_k}{k} \, . \tag{2.131}$$

Inserting these constants in Eqs. (2.126) and (2.127) gives us the starting solution for u, v as:

$$u = -\frac{c_1}{k}\left(C_k\frac{n(n+1)}{kr}j_n(kr) + j_n'(kr)\right) , \tag{2.132}$$

$$v = -\frac{c_1}{k}\left((1+C_k)\frac{1}{kr}j_n(kr) + C_k\, j_n'(kr)\right) . \tag{2.133}$$

3. T_r

   Inserting (2.118) and (2.132) into Eq. (2.41) we have:

$$T_r = c_1\left[\lambda j_n(kr) - 2\mu\left(C_k\frac{n(n+1)}{kr}j_n'(kr) - C_k\frac{n(n+1)}{(kr)^2}j_n(kr) + j_n''(kr)\right)\right] ,$$

   so that the starting solution for T_r is:

$$T_r = c_1\left[\lambda j_n(kr) + 2\mu C_k\frac{n(n+1)}{kr}\left(\frac{1}{kr}j_n(kr) - j_n'(kr)\right) - 2\mu j_n''(kr)\right] . \tag{2.134}$$

4. T_θ

   Inserting (2.132) and (2.133) into Eq. (2.37) and using Eq. (B.1) we have:

$$\begin{aligned}
T_\theta &= -\frac{\mu c_1}{k}\left((1+C_k)\frac{1}{r}j_n'(kr) - (1+C_k)\frac{1}{kr^2}j_n(kr) + kC_k\, j_n''(kr)\right) \\
&\quad + \frac{\mu c_1}{kr}\left((1+C_k)\frac{1}{kr}j_n(kr) + C_k\, j_n'(kr)\right) - \frac{\mu c_1}{kr}\left(C_k\frac{n(n+1)}{kr}j_n(kr) + j_n'(kr)\right) = \\
&= \frac{\mu c_1}{k}\left(-\frac{2}{r}j_n'(kr) + \frac{2}{kr^2}(1+C_k)j_n(kr) - \frac{n(n+1)}{kr^2}C_k\, j_n(kr) - kC_k\, j_n''(kr)\right) = \\
&= -\mu c_1\left(\frac{2}{kr}j_n'(kr) - \frac{2}{(kr)^2}(1+C_k)j_n(kr) + \frac{n(n+1)}{(kr)^2}C_k\, j_n(kr) + C_k\, j_n''(kr)\right) = \\
&= -\mu c_1\left(\frac{2}{kr}(1+C_k)j_n'(kr) - \frac{2}{(kr)^2}(1+C_k)j_n(kr) + C_k\, j_n(kr) + 2C_k\, j_n''(kr)\right) ,
\end{aligned}$$

   so that the starting solution for T_θ is:

$$T_\theta = -\mu c_1\left[C_k j_n(kr) - \frac{2}{kr}(1+C_k)\left(\frac{1}{kr}j_n(kr) - j_n'(kr)\right) + 2C_k j_n''(kr)\right] . \tag{2.135}$$

5. Q
   Inserting (2.122) and (2.132) into Eq. (2.48) we have:

$$\begin{aligned} Q &= c_1 \frac{4\pi G\rho_0}{k} j_n'(kr) + c_1 \frac{n+1}{r} \frac{4\pi G\rho_0}{k^2} j_n(kr) \\ & \quad - c_1 \frac{4\pi G\rho_0}{k} \left(C_k \frac{n(n+1)}{kr} j_n(kr) + j_n'(kr) \right) = \\ &= c_1 \frac{4\pi G\rho_0 (n+1)}{k^2 r} j_n(kr) - c_1 C_k \frac{4\pi G\rho_0 n(n+1)}{k^2 r} j_n(kr) = \\ &= c_1 \frac{1}{k^2 r} 4\pi G\rho_0 (n+1)(1 - nC_k) j_n(kr)\,, \end{aligned} \tag{2.136}$$

   so that the starting solution for Q is:

$$Q = c_1 (1 - nC_k) 4\pi G\rho_0 \frac{n+1}{k^2 r} j_n(kr)\,. \tag{2.137}$$

Eqs. (2.132), (2.133), (2.134), (2.135), (2.122) and (2.137) are the first set of starting solutions for (u, v, T_r, T_θ, ϕ, Q), respectively.

- **Fundamental solutions for $\boldsymbol{\chi = c_2\, j_n(qr)}$**
  Consider χ in form:

$$\chi = c_2\, j_n(qr)\,. \tag{2.138}$$

  The second set of starting solutions is formally equal to the one associated to $\chi = c_1\, j_n(kr)$ substituting c_1 with c_2 and k with q, so that C_k has to be substituted with:

$$C_q = -\frac{\xi}{v_S^2\, q^2}\,. \tag{2.139}$$

- **Fundamental solutions for $\boldsymbol{\chi = 0}$**
  Consider the null solution for χ, that is a valid solution to Eq. (2.110) too.
  We can find a solution for each unknown variable u, v, T_r, T_θ, ϕ, Q as follows:

1. ϕ
   Poisson's Eq. (2.45) becomes the following Laplace's equation:

$$\nabla_r^2 \phi = 0\,, \tag{2.140}$$

   so that we can assume a regular starting form for ϕ as:

$$\phi = c_3\, \xi\, r^n\,. \tag{2.141}$$

2. u
If $\chi = 0$ then $\vec{\nabla} \cdot \vec{u} = 0$, and Eq. (2.20) can be written as:

$$\rho_0 \vec{\nabla}(\phi_1 + g_0\, \vec{u} \cdot \hat{r}) + \mu(\vec{\nabla} \times \vec{\nabla} \times \vec{u}) = 0\,. \tag{2.142}$$

Applying the divergence to it we have:

$$\nabla^2(\phi_1 + g_0\, \vec{u} \cdot \hat{r}) = 0\,. \tag{2.143}$$

The radial component of Eq. (2.142) is:

$$\rho_0 \frac{\partial}{\partial r}(\phi_1 + g_0\, \vec{u} \cdot \hat{r}) + \mu(\vec{\nabla} \times \vec{\nabla} \times \vec{u}) \cdot \hat{r} = 0\,. \tag{2.144}$$

Using the harmonic decomposition (2.58), we can work only on radial coefficients of Eqs. (2.142) and (2.144) so that:

$$\nabla_r^2(\phi + \xi\, ru) = 0\,, \tag{2.145}$$

$$\rho_0(\phi + \xi\, ru)' - \mu \frac{n(n+1)}{r} H = 0\,. \tag{2.146}$$

In the case of null χ, Eq. (2.44) becomes:

$$u' + \frac{2}{r}u - \frac{n(n+1)}{r}v = 0\,, \tag{2.147}$$

hence:

$$v = \frac{1}{n(n+1)}(ru' + 2u)\,. \tag{2.148}$$

Eq. (2.56) becomes:

$$\begin{aligned} H &= \frac{1}{n(n+1)}(u' + ru'' + 2u') + \frac{1}{n(n+1)}\left(u' + \frac{2}{r}u\right) - \frac{u}{r} = \\ &= \frac{1}{n(n+1)}\left(ru'' + 3u' + u' + \frac{2}{r}u\right) - \frac{u}{r} = \\ &= \frac{1}{n(n+1)}\frac{1}{r}(r^2u'' + 4ru' + 2u) - \frac{u}{r} = \\ &= \frac{1}{n(n+1)}\frac{(r^2u)''}{r} - \frac{u}{r}\,, \end{aligned} \tag{2.149}$$

Inserting this formulation of H into Eq. (2.146) we obtain:

$$\rho_0(\phi+\xi ru)' - \mu\frac{n(n+1)}{r}\left(\frac{1}{n(n+1)}\frac{(r^2u)''}{r} - \frac{u}{r}\right) = 0$$

$$\rho_0(\phi+\xi ru)' - \mu\frac{(r^2u)''}{r^2} + \mu\frac{n(n+1)}{r^2}u = 0$$

$$\frac{\rho_0 r^2}{\mu}(\phi+\xi ru)' - (r^2u)'' + n(n+1)u = 0\,. \tag{2.150}$$

From Eq. (2.145) we have that $\phi+\xi ru$ is harmonic and we can assume it in form as:

$$\phi+\xi ru = c_4\xi\, r^n\,, \tag{2.151}$$

so that, recalling Eq. (2.141) and rearranging the terms, we can write:

$$u = (c_4 - c_3)r^{n-1}\,. \tag{2.152}$$

Using these decompositions into Eq. (2.150) we have:

$$\frac{\rho_0 r^2}{\mu}(c_4\xi\, r^n)' - (c_4-c_3)(r^{n+1})'' + n(n+1)(c_4-c_3)r^{n-1} = 0$$

$$\frac{\rho_0 r^2}{\mu}c_4\xi\, nr^{n-1} - (c_4-c_3)n(n+1)r^{n-1} + n(n+1)(c_4-c_3)r^{n-1} = 0$$

$$\frac{\rho_0 r^2}{\mu}\xi c_4 = 0\,, \tag{2.153}$$

so that $c_4 = 0$ and:

$$u = -c_3\, r^{n-1}\,. \tag{2.154}$$

3. v

Inserting (2.154) into Eq. (2.148) we have:

$$\begin{aligned} v &= \frac{1}{n(n+1)}\left(-c_3(n-1)r^{n-1} - 2c_3r^{n-1}\right) = \\ &= -\frac{c_3}{n(n+1)}(n-1+2)r^{n-1}\,, \end{aligned} \tag{2.155}$$

hence:

$$v = -\frac{c_3}{n}r^{n-1}\,. \tag{2.156}$$

4. T_r

In the null χ case, inserting (2.154) into Eq. (2.41) we have:

$$T_r = -2\mu c_3(n-1)r^{n-2}\,. \tag{2.157}$$

5. T_θ
   Inserting (2.154) and (2.156) into Eq. (2.37) we have:

$$\begin{aligned} T_\theta &= \mu\left(-\frac{c_3}{n}(n-1)r^{n-2} + \frac{c_3}{n}r^{n-2} - c_3 r^{n-2}\right) = \\ &= \mu c_3\left(-\frac{n-1}{n} + \frac{1}{n} - 1\right) r^{n-2} = \\ &= \mu c_3\left(\frac{-n+1+1-n}{n}\right) r^{n-2}\,, \end{aligned} \tag{2.158}$$

   hence:

$$T_\theta = -2\mu c_3 \frac{n-1}{n} r^{n-2}. \tag{2.159}$$

6. Q
   Inserting (2.141) and (2.154) into Eq. (2.48) we have:

$$\begin{aligned} Q &= c_3\xi n r^{n-1} + \frac{n+1}{r}c_3\xi r^n - 4\pi G\rho_0 c_3 r^{n-1} = \\ &= c_3(\xi n + (n+1)\xi - 4\pi G\rho_0)r^{n-1}\,, \end{aligned} \tag{2.160}$$

   hence:

$$Q = c_3((2n+1)\xi - 4\pi G\rho_0)r^{n-1}\,. \tag{2.161}$$

   Eqs. (2.154), (2.156), (2.157), (2.159), (2.141) and (2.161) are the third set of starting solutions for (u, v, T_r, T_θ, ϕ, Q), respectively.

The general starting solution for each of the six unknown variables of the problem is the linear combination of the three corresponding starting solutions of the three sets obtained above.

We can also rewrite the general starting solution in the y notation using the $\vec{y}$ vector form (2.84) so that:

$$\vec{y} = Y(r)c\,, \tag{2.162}$$

where $c = (c_1, c_2, c_3)^T$ and:

$$Y(r) = [Y_1|Y_2|Y_3]\,, \tag{2.163}$$

$$
Y_1 = \begin{pmatrix}
-\frac{1}{k}\left(C_k \frac{n(n+1)}{kr} j_n(kr) + j_n'(kr)\right) \\
-\frac{1}{k}\left((1+C_k)\frac{1}{kr} j_n(kr) + C_k\, j_n'(kr)\right) \\
\lambda j_n(kr) + 2\mu C_k \frac{n(n+1)}{kr}\left(\frac{1}{kr} j_n(kr) - j_n'(kr)\right) - 2\mu j_n''(kr) \\
-\mu\left[C_k\, j_n(kr) - \frac{2}{kr}(1+C_k)\left(\frac{1}{kr} j_n(kr) - j_n'(kr)\right) + 2C_k\, j_n''(kr)\right] \\
\frac{4\pi G\rho_0}{k^2} j_n(kr) \\
(1 - nC_k) 4\pi G\rho_0 \frac{n+1}{k^2 r} j_n(kr)
\end{pmatrix}, \quad (2.164)
$$

$$
Y_2 = \begin{pmatrix}
-\frac{1}{q}\left(C_q \frac{n(n+1)}{qr} j_n(qr) + j_n'(qr)\right) \\
-\frac{1}{q}\left((1+C_q)\frac{1}{qr} j_n(qr) + C_q\, j_n'(qr)\right) \\
\lambda j_n(qr) + 2\mu C_q \frac{n(n+1)}{qr}\left(\frac{1}{qr} j_n(qr) - j_n'(qr)\right) - 2\mu j_n''(qr) \\
-\mu\left[C_q\, j_n(qr) - \frac{2}{qr}(1+C_q)\left(\frac{1}{qr} j_n(qr) - j_n'(qr)\right) + 2C_q\, j_n''(qr)\right] \\
\frac{4\pi G\rho_0}{q^2} j_n(qr) \\
(1 - nC_q) 4\pi G\rho_0 \frac{n+1}{q^2 r} j_n(qr)
\end{pmatrix}, \quad (2.165)
$$

$$
Y_3 = \begin{pmatrix}
nr^{n-1} \\
r^{n-1} \\
2\mu n(n-1) r^{n-2} \\
2\mu(n-1) r^{n-2} \\
-n\xi r^n \\
(4\pi G\rho_0 - (2n+1)\xi) n r^{n-1}
\end{pmatrix}. \quad (2.166)
$$

The third set of starting solutions reported in (2.166) is multiplied by $-n$ as done in [Wu and Peltier, 1982], taking advantage of the linearity of the problem.

2 Incompressible homogeneous elastic body

The assumption of incompressibility:

$$\vec{\nabla} \cdot \vec{u} = 0 \tag{2.167}$$

is often taken to simplify a planetary model and to study its shape deformations without considering density variation and volume changes. In this case, the problem admits analytical solutions without any additional assumptions, such as the one on the constant ratio ξ made before. The theory underlying the incompressible case is analogous to the one exposed for the compressible deformation model, so we will report here only the main differences and results.

2.1 Governing laws

The unperturbed state of a spherically symmetric, self-gravitating, non-rotating, elastic body that is homogeneous and incompressible is formally equal to the unperturbed state of a compressible body illustrated in Section 1 of this Chapter.
The governing physical laws of the perturbed body are the same too, so Eqs. (2.5), (2.6), (2.7) and (2.8) are still valid.

The main difference is that instead of Eq. (2.11) we have:

$$\rho_1 = 0\,, \tag{2.168}$$

due to the incompressibility of the body (2.167).
In this case, we also have to introduce a new variable Π as done in [Love, 1911]:

$$\Pi = \lim_{\lambda\to\infty\,,\,\vec{\nabla}\cdot\vec{u}\to 0} (\lambda\,\vec{\nabla}\cdot\vec{u})\,, \tag{2.169}$$

because considering the incompressible limit of a body is analogous to working with an infinity-value λ in its compressible case, so that the product of λ and the null volume change is finite. Π represents the average normal stress exerted on the body.

Inserting Eqs. (2.168) and (2.169) into the main governing laws, we obtain the governing physical laws of an incompressible homogeneous elastic body as:

$$\begin{cases} \vec{\nabla} \cdot \vec{u} = 0 \\ \nabla^2 \phi_1 = 0 \\ \vec{\nabla}\,(\Pi - \rho_0 \phi_1 - \rho_0 g_0 \vec{u}\cdot\hat{r}) - \mu\vec{\nabla}\times\vec{\nabla}\times\vec{u} = 0 \\ \tau_{ij} = \Pi\,\delta_{ij} + 2\mu\epsilon_{ij} \end{cases} \tag{2.170}$$

The unknown variables of the problem are the three components of the vector displacement (u_r, u_θ, u_φ), the gravitational potential variation ϕ_1 and the average normal stress Π.

2.2 Problem ODEs system

Following the same harmonic decomposition approach for each unknown variable of the problem, we can reach a formulation in y notation analogous to (2.85):

$$\vec{y}\,' = A^{inc}\,\vec{y}\,, \tag{2.171}$$

where A^{inc} is the 6×6 coefficients matrix defined as:

$$A^{inc} = \begin{pmatrix} -\dfrac{2}{r} & \dfrac{n(n+1)}{r} & 0 & 0 & 0 & 0 \\ -\dfrac{1}{r} & \dfrac{1}{r} & 0 & \dfrac{1}{\mu} & 0 & 0 \\ \dfrac{4}{r}\left(\dfrac{3\mu}{r} - \rho_0 g_0\right) & -\dfrac{n(n+1)}{r}\left(\dfrac{6\mu}{r} - \rho_0 g_0\right) & 0 & \dfrac{n(n+1)}{r} & -\rho_0 \dfrac{n+1}{r} & \rho_0 \\ -\dfrac{1}{r}\left(\dfrac{6\mu}{r} - \rho_0 g_0\right) & -\dfrac{2\mu}{r^2}\left(1 - 2n(n+1)\right) & -\dfrac{1}{r} & -\dfrac{3}{r} & \dfrac{\rho_0}{r} & 0 \\ -4\pi G\rho_0 & 0 & 0 & 0 & -\dfrac{n+1}{r} & 1 \\ -4\pi G\rho_0 \dfrac{n+1}{r} & 4\pi G\rho_0 \dfrac{n(n+1)}{r} & 0 & 0 & 0 & \dfrac{n-1}{r} \end{pmatrix}. \tag{2.172}$$

2.3 Starting solutions for numerical integration

The procedure to find the three sets of starting solutions for numerical integration is formally the same already illustrated in Section 1 of this Chapter, but starting from a regular form of $\phi = y_5$ near $r = 0$ that is:

$$\phi = c_3\, r^n\,, \tag{2.173}$$

thanks to Laplace's equation in Eqs. (2.170).

We can write the general starting solution in y notation so that:

$$\vec{y} = Y^{inc}\, c\,, \tag{2.174}$$

where $c = (c_1,\, c_2,\, c_3)^T$ and:

$$Y^{inc} = \begin{pmatrix} \dfrac{n}{2(2n+3)} r^{n+1} & r^{n-1} & 0 \\ \dfrac{n+3}{2(n+1)(2n+3)} r^{n+1} & \dfrac{1}{n} r^{n-1} & 0 \\ \dfrac{n\rho_0 g_0 r + 2(n^2-n-3)\mu}{2(2n+3)} r^n & (\rho_0 g_0 r + 2(n-1)\mu) r^{n-2} & \rho_0 r^n \\ \dfrac{n(n+2)}{(2n+1)(2n+3)} \mu r^n & \dfrac{2(n-1)}{n} \mu r^{n-2} & 0 \\ 0 & 0 & r^n \\ 2\pi G \rho_0 \dfrac{n}{2n+3} r^{n+1} & 4\pi G \rho_0 r^{n-1} & (2n+1) r^{n-1} \end{pmatrix}. \tag{2.175}$$

3 Fluid layers

We know that the Earth has an outer core made of liquid Fe with a few percent Ni in it [Turcotte and Schubert, 2002, Belardinelli, 2025]. This layer is the source of our planetary magnetic field, thanks to the phenomenon called geodynamo, sustainable only for liquid charged material in motion [Bullard and Gellman, 1954].
In view of this, an Earth-like planetary model that is more consistent with the current knowledge of our planet has to consider the presence of fluid layers inside it. In order to study the physics that underlies this kind of layer and its boundary conditions at the interfaces with solid regions of the planet, we expose the topic as follows.

3.1 Governing laws

Consider a spherically symmetric, self-gravitating, non-rotating, homogeneous and inviscid fluid body.
In both unperturbed and perturbed states, its governing laws are the hydrostatic equation:

$$\vec{\nabla} p = -\rho g_0 \widehat{r} = -\rho \vec{\nabla} \phi \,, \tag{2.176}$$

where p is pressure, ρ is density, g_0 is gravity acceleration and ϕ is gravitational potential, and the Poisson's equation for the gravitational potential:

$$\nabla^2 \phi = 4\pi G \rho \,. \tag{2.177}$$

We indicate the unperturbed values of pressure, density and gravitational potential with the notation p_0, ρ_0, ϕ_0, respectively.
As discussed for the solid layers, in the perturbed state the pressure shows a variation equal to $p_1(r,\gamma)$, the density shows a variation equal to $\rho_1(r,\gamma)$ and the gravitational potential shows a variation equal to $\phi_1(r,\gamma)$, both depending on radial r and angular position $\gamma = (\theta, \varphi)$.

The hydrostatic equation (2.176) is still valid as:

$$\begin{aligned}
\vec{\nabla}(p_0 + p_1) &= -(\rho_0 + \rho_1)\,\vec{\nabla}(\phi_0 + \phi_1) \\
\vec{\nabla} p_0 + \vec{\nabla} p_1 &= -\rho_0 \vec{\nabla}\phi_0 - \rho_0 \vec{\nabla}\phi_1 - \rho_1 \vec{\nabla}\phi_0 - \rho_1 \vec{\nabla}\phi_1 \\
\vec{\nabla} p_1 &= -\rho_0 \vec{\nabla}\phi_1 - \rho_1 \vec{\nabla}\phi_0 \,,
\end{aligned} \tag{2.178}$$

where we have used Eq. (2.176) for unperturbed values and neglected the second order term $\rho_1 \vec{\nabla}\phi_1$.

If we write all the components of Eq. (2.178) we have:

$$\begin{cases} \dfrac{\partial p_1}{\partial r} = -\rho_0 \dfrac{\partial \phi_1}{\partial r} - \rho_1 g_0 \\ \dfrac{\partial p_1}{\partial \theta} = -\rho_0 \dfrac{\partial \phi_1}{\partial \theta} \\ \dfrac{\partial p_1}{\partial \varphi} = -\rho_0 \dfrac{\partial \phi_1}{\partial \varphi} \end{cases} \tag{2.179}$$

and at first order: $\rho(r) = \rho_0(r)$, so that: $p_1 = -\rho_0 \phi_1$, and in radial component (2.179) we have:

$$\begin{aligned} \frac{\partial(-\rho_0\phi_1)}{\partial r} &= -\rho_0 \frac{\partial \phi_1}{\partial r} - \rho_1 g_0 \\ -\frac{\partial \rho_0}{\partial r}\phi_1 - \frac{\partial \phi_1}{\partial r}\rho_0 &= -\rho_0 \frac{\partial \phi_1}{\partial r} - \rho_1 g_0 \\ \rho_0' \phi_1 &= \rho_1 g_0 \,. \end{aligned} \tag{2.180}$$

Poisson's equation is still valid in the perturbed state, so that:

$$\nabla^2 \phi_1 = 4\pi G \rho_1 \,, \tag{2.181}$$

and using Eq. (2.180) we have:

$$\nabla^2 \phi_1 = \frac{4\pi G \rho_0'}{g_0} \phi_1 \,. \tag{2.182}$$

We have to consider the shifting of physical surfaces induced by the perturbation too.
If an equipotential surface in the unperturbed state can be individuated by notation: $\phi_0(r) = const.$, then after the perturbation it will be shifted by ε_ϕ, so that:

$$\phi(r + \varepsilon_\phi) = \phi_0(r) \,, \tag{2.183}$$

and if $\varepsilon_\phi \ll r$ then:

$$\phi(r) = \phi_0(r) - \varepsilon_\phi(r, \gamma)\, \phi_0'(r) \,. \tag{2.184}$$

Similar relations can be obtained for isobaric surfaces $p_0(r) = const.$ and equal-density surfaces $\rho_0(r) = const.$ as:

$$p(r) \quad = p_0(r) - \varepsilon_p(r, \gamma)\, p_0'(r) \,, \tag{2.185}$$

$$\rho(r) \quad = \rho_0(r) - \varepsilon_\rho(r, \gamma)\, \rho_0'(r) \,, \tag{2.186}$$

where ε_p and ε_ρ are their respective shiftings.
As shown in [Spada et al., 2025], at harmonic degrees $n > 0$ all these shiftings are equal to each other:

$$\varepsilon_\phi = \varepsilon_p = \varepsilon_\rho = \varepsilon(r, \gamma) \,. \tag{2.187}$$

The unknown variables of the problem are the gravitational potential variation ϕ_1 and the shifting of physical surfaces ε.

3.2 Obtaining the problem ODEs system

As we shall see in the following discussion, the fluid layer problem has less unknown variables than the solid one, passing from six to only two variables describing the deformation.

We decompose the unknown variables as previously done for solid cases:

$$\phi_1 = \sum_n \phi P\,, \tag{2.188}$$

$$\varepsilon = \sum_n u P\,, \tag{2.189}$$

where $\phi = \phi(r)$ and $u = u(r)$ are radial functions acting as polynomial coefficients of gravitational potential variation and shifting, respectively.

Now starting from two rearranged equations of fluid layers we can obtain the ODEs system of the problem as follows.

1. *Poisson's equation for gravitational potential variation*
   Inserting the harmonic decomposition (2.188) into Eq. (2.182) and using (A.13), (2.23) we have:

$$\begin{aligned}
\nabla^2\left(\sum_n \phi P\right) &= \frac{4\pi G\rho_0'}{g_0}\sum_n \phi P \\
\sum_n\left(\phi'' P + \frac{2}{r}\phi' P + \frac{1}{r^2}\phi P_{\theta\theta} + \frac{\cot\theta}{r^2}\phi P_\theta\right) &= \frac{4\pi G\rho_0'}{g_0}\sum_n \phi P \\
\sum_n\left(\phi'' + \frac{2}{r}\phi' - \frac{n(n+1)}{r^2}\phi\right)P &= \frac{4\pi G\rho_0'}{g_0}\sum_n \phi P\,,
\end{aligned} \tag{2.190}$$

   and working only on radial scalar values we obtain:

$$\phi'' + \frac{2}{r}\phi' - \left(\frac{n(n+1)}{r^2} + \frac{4\pi G\rho_0'}{g_0}\right)\phi = 0\,. \tag{2.191}$$

   This relation is formally equal to Eq. (16) of [Saito, 1974].

2. *Equivalent Bruns' formula*
   Starting from Eq. (2.184), we can obtain an analogous formulation of the Bruns' formula [Spada et al., 2025] as:

$$u = -\frac{\phi}{g_0}\,. \tag{2.192}$$

From Eqs. (2.191) and (2.192), applying some rearrangements we can obtain the final ODEs system of the fluid problem in the (ϕ, y_7) set of unknown radial variables, where y_7 will be properly defined later.

- *ODE 1*
  In the same way as we have defined Q in Eq. (2.48), it is useful to define a new variable y_7 for the fluid case having the same role of Q :

$$y_7 = \phi' + \frac{n+1}{r}\phi + 4\pi G\rho_0 u\,, \tag{2.193}$$

  and using Eq. (2.192) we have:

$$y_7 = \phi' + \left(\frac{n+1}{r} - \frac{4\pi G\rho_0}{g_0}\right)\phi\,, \tag{2.194}$$

  that is formally equal to Eq. (17) of [Saito, 1974], except for the sign choice in the last term. [Saito, 1974] was also the first work to introduce the y_7 formulation to simplify the dimensionality of the fluid layer problem.
  Making ϕ' explicit from the previous equation, we reach:

$$\phi' = \left(\frac{4\pi G\rho_0}{g_0} - \frac{n+1}{r}\right)\phi + y_7\,. \tag{2.195}$$

- *ODE 2*
  If we differentiate Eq. (2.194) with respect to r and use Eqs. (2.191) and (2.76), we have:

$$\begin{aligned}
y_7' &= \phi'' + \left(\frac{n+1}{r} - \frac{4\pi G\rho_0}{g_0}\right)\phi' - \left(\frac{n+1}{r^2} + \frac{4\pi G\rho_0'}{g_o} - \frac{4\pi G\rho_0 g_0'}{g_0^2}\right)\phi = \\
&= \frac{n(n+1)}{r^2}\phi + \left(\frac{n-1}{r} - \frac{4\pi G\rho_0}{g_0}\right)\phi' - \left(\frac{n+1}{r^2} - \frac{4\pi G\rho_0 g_0'}{g_0^2}\right)\phi = \\
&= \left(\frac{n-1}{r} - \frac{4\pi G\rho_0}{g_0}\right)\left[y_7 + \left(\frac{4\pi G\rho_0}{g_0} - \frac{n+1}{r}\right)\phi\right] \\
&\quad + \left(\frac{(n+1)(n-1)}{r^2} + \left(\frac{4\pi G\rho_0}{g_0}\right)^2 - \frac{8\pi G\rho_0}{g_0 r}\right)\phi = \\
&= \left(\frac{n-1}{r} - \frac{4\pi G\rho_0}{g_0}\right)y_7 + \frac{8\pi G\rho_0 n}{g_0 r}\phi - \frac{8\pi G\rho_0}{g_0 r}\phi\,,
\end{aligned} \tag{2.196}$$

  so that:

$$y_7' = \frac{8\pi G\rho_0(n-1)}{g_0 r}\phi + \left(\frac{n-1}{r} - \frac{4\pi G\rho_0}{g_0}\right)y_7\,. \tag{2.197}$$

Summarizing the ODEs obtained so far:

$$\begin{cases} \phi' = \left(\dfrac{4\pi G\rho_0}{g_0} - \dfrac{n+1}{r}\right)\phi + y_7 \\ \\ y_7' = \dfrac{8\pi G\rho_0(n-1)}{g_0 r}\phi + \left(\dfrac{n-1}{r} - \dfrac{4\pi G\rho_0}{g_0}\right) y_7 \end{cases} \tag{2.198}$$

we can also rewrite the problem in y notation using the $\vec{y}$ vector form for the fluid case as:

$$\vec{y}_f = (y_5, y_7)^T = (\phi, y_7)^T \,, \tag{2.199}$$

so that we have to solve:

$$\vec{y}_f{}' = A_f\,\vec{y}_f \,, \tag{2.200}$$

where A_f is the 2×2 matrix of coefficients, depending only on ρ_0, g_0, harmonic degree n and radius r:

$$A_f = \begin{pmatrix} \dfrac{4\pi G\rho_0}{g_0} - \dfrac{n+1}{r} & 1 \\ \dfrac{8\pi G\rho_0(n+1)}{g_0 r} & \dfrac{n-1}{r} - \dfrac{4\pi G\rho_0}{g_0} \end{pmatrix}. \tag{2.201}$$

3.3 Starting solutions for numerical integration

For the sake of completeness, we also report the starting solutions for numerical integration if the starting layer is fluid.

Consider again Eq. (2.191), then we can assume a regular solution in $r = 0$ for ϕ in form:

$$\phi(r) = c_f\, r^n \,. \tag{2.202}$$

Inserting (2.202) into Eq. (2.193) we have:

$$\begin{aligned} y_7 &= n c_f\, r^{n-1} + \frac{n+1}{r} c_f\, r^n - \frac{4\pi G\rho_0}{g_0} c_f\, r^n = \\ &= c_f \left((n r^{n-1} + (n+1) r^{n-1}) - \frac{4\pi G\rho_0}{g_0} r^n \right) , \end{aligned} \tag{2.203}$$

so that:

$$y_7 = c_f \left(\frac{2n+1}{r} - \frac{4\pi G\rho_0}{g_0}\right) r^n \,. \tag{2.204}$$

We can also rewrite the general fluid starting solution in vector notation using the $\vec{y}$ vector form (2.199) so that:

$$\vec{y}_f = Y_f(r)\, c_f \,, \tag{2.205}$$

where:

$$Y_f = \begin{pmatrix} r^n \\ \left(\dfrac{2n+1}{r} - \dfrac{4\pi G \rho_0}{g_0}\right) r^n \end{pmatrix} . \tag{2.206}$$

3.4 Boundary conditions at fluid-to-solid interface

The presence of a fluid layer in the planetary differentiation introduces boundary conditions that must be satisfied at the interfaces between fluid and solid layers.
In the literature, there are many papers that faced this problem with different approaches, assuming the continuity of many $\vec{y}$ components, like in [Takeuchi and Saito, 1972] and [Martens, 2016], or introducing a new variable that reduces the dimensionality of the problem from six unknown variables to two, like in [Saito, 1974] and [Spada et al., 2025]. Here we follow the second, applied to the transition from fluid to solid layers, while in the next Subsection we describe it in the opposite sense, following the theory of [Spada et al., 2025]. For the fluid-to-solid interface inside the Earth, we may think of the case of the transition from the fluid outer core to the solid mantle of our planet.

Integration in the fluid layer is carried out through one set of two variables in vector form: $\vec{y}_f = (y_5,\, y_7)^f$, while when entering the solid layer we need three sets of six variables in vector form: $\vec{y}_{s,i} = (y_1,\, y_2,\, y_3,\, y_4,\, y_5,\, y_6)^s_i\,, \quad i = 1, 2, 3$. Consider an interface at $r = b$, where $r < b$ is fluid and $r > b$ is solid, then we need to write each variable of the solid layer as a linear combination of the fluid variables as follows.

- *Radial displacement* $y_1 = u$
  In the fluid layer, the shifting of all the physical surfaces ϕ_0, p_0, ρ_0 is defined by Eq. (2.192), including the material ones.
  In the solid layer, we have to consider the possibility of an extra-displacement of the surfaces, due to the independence between displacements of equipotential and material surfaces. We assume an arbitrary constant displacement K_2 so that:

$$y_1^s(b_+) = -\frac{y_5^f(b_-)}{g_0(b)} + K_2 \,. \tag{2.207}$$

- *Tangential displacement* $y_2 = v$
  In the fluid layer, no shear stress is allowed so there is no tangential displacement.
  In the solid layer, we have to consider the possibility of free-slip conditions that produce an arbitrary constant tangential displacement K_3 so that:

$$y_2^s(b_+) = K_3 \,. \tag{2.208}$$

- *Radial stress* $y_3 = T_r$
  In the fluid layer, the isobaric surfaces follow a displacement as shown by Eq. (2.192) while in the solid layer we have an extra displacement K_2, as already shown in Eq. (2.207). If we consider the pressure right below the interface $r = b$ for a displacement equal to K_2, from Eqs. (2.185) and (2.1) we have:

$$p(b_-) = p_0(b) + K_2\, p_0'(b) = p_0(b) - \rho_0(b_-)g_0(b)K_2\,, \tag{2.209}$$

  so that:

$$y_3^s(b_+) = \rho_0(b_-)g_0(b)K_2\,. \tag{2.210}$$

- *Tangential stress* $y_4 = T_\theta$
  In the fluid layer, no shear stress is allowed and so also in the solid layer it cannot be present:

$$y_4^s(b_+) = y_4^f(b_-) = 0\,. \tag{2.211}$$

- *Gravitational potential variation* $y_5 = \phi$
  The variation in gravitational potential must be continuous between the fluid and solid layers:

$$y_5^s(b_+) = y_5^f(b_-)\,. \tag{2.212}$$

- *Variable* $y_6 = Q$
  As already presented in [Chinnery, 1975] and [Spada et al., 2025], obtaining the boundary condition for Q is not so trivial.
  If we consider a point A on the solid side and a point B on the fluid side of the boundary, infinitely close to each other, in the unperturbed state the gravitational potential ϕ_0 and its first derivative ϕ_0' are continuous: $\phi_0(A) = \phi_0(B)$, $\phi_0'(A) = \phi_0'(B)$, and the Poisson's equation (2.2) is valid on both sides of the boundary.
  In the perturbed state, A will be displaced in A' and B will be displaced in B', where A' and B' are still infinitely close so that: $\phi_0(A') = \phi_0(B')$, $\phi_0'(A') = \phi_0'(B')$ and from a Taylor expansion we have:

$$\phi'(A') \;= \phi'(A) + u_r(A)\phi_0''(A)\,, \tag{2.213}$$

$$\phi'(B') \;= \phi'(B) + u_r(A)\phi_0''(B)\,, \tag{2.214}$$

  where $u_r(A) = (\overline{AA'})_r = (\overline{BB'})_r$.
  Since the gravitational potential ϕ is the sum of unperturbed gravitational potential ϕ_0 and the gravitational potential variation ϕ_1, then using Eqs. (2.213), (2.214) and the full expression of spherical laplacian in Poisson's equation we obtain:

$$\begin{aligned}\phi_1'(A) - \phi_1'(B) &= \phi'(A) - \phi'(B) = \\ &= u_r(A)\,(\phi_0''(B) - \phi_0''(A)) = \\ &= 4\pi G u_r(A)\,(\rho_0(B) - \rho_0(A))\,. \end{aligned} \tag{2.215}$$

Using the y notation:

$$y_5^{s\,\prime}(A) - y_5^{f\,\prime}(B) = 4\pi G y_1^s(A)\,(\rho_0(B) - \rho_0(A))\;, \tag{2.216}$$

and thanks to Eqs. (2.48), (2.193) and (2.212) we obtain:

$$y_6(A) - y_7(B) = 4\pi G \rho_0(B)\,\left(y_1^s(A) - y_1^f(B)\right)\;, \tag{2.217}$$

where we have omitted the superscripts for y_6 and y_7 because these variables only refer to solid and fluid layers, respectively.
In conclusion, recalling that Eq. (2.207) asserts that: $y_1^s(b_+) = y_1^f(b_-) + K_2$, we have:

$$y_6(b_+) = y_7(b_-) + 4\pi G \rho_0(b_-) K_2\,. \tag{2.218}$$

The previous boundary conditions at the fluid-solid contact can be summarized and displayed in the following three sets of solid solutions necessary to continue the numerical integration:

$$\vec{y}_{s,1} = \begin{pmatrix} -\dfrac{y_5^f(b_-)}{g_0(b)} \\ 0 \\ 0 \\ 0 \\ y_5^f(b_-) \\ y_7(b_-) \end{pmatrix}, \tag{2.219}$$

$$\vec{y}_{s,2} = \begin{pmatrix} 1 \\ 0 \\ \rho_0^f\, g_0(b)\, y_{1,2}^s \\ 0 \\ y_5^f(b_-) \\ y_7(b_-) \end{pmatrix}, \tag{2.220}$$

$$\vec{y}_{s,3} = \begin{pmatrix} 0 \\ 1 \\ 0 \\ 0 \\ 0 \\ 0 \end{pmatrix}, \tag{2.221}$$

so that the general solution that can be numerically integrated into the solid layer is:

$$\vec{y_s} = \vec{y}_{s,1} + K_2\,\vec{y}_{s,2} + K_3\,\vec{y}_{s,3}\,. \tag{2.222}$$

The three sets of boundary solid solutions (2.219), (2.220), (2.221) represent respectively: the solution in continuity with the fluid deformation; the solution due to the extra-displacement of the solid layer; the free-slip solution of the solid layer.

3.5 Boundary conditions at solid-to-fluid interface

Entering the fluid layer from the solid side of the interface is the reverse case of the one discussed in Subsection 3.4, and we may think of the case of the transition from the solid inner core to the fluid outer core of the Earth.

Integration in the solid layer is carried out by three sets of six variables in vector form: $\vec{y}_{s,i} = (y_1,\, y_2,\, y_3,\, y_4,\, y_5,\, y_6)^s_i\,, i = 1, 2, 3$, while when entering the fluid layer we need only one set of two variables in vector form: $\vec{y}_f = (y_5,\, y_7)^f$. Consider an interface at $r = c$, where $r < c$ is solid and $r > c$ is fluid, then we have to impose boundary conditions that constrain the solid solutions to the correct linear combination associated with the fluid solution.

On the solid side of the interface, the general solution for the m component of $\vec{y}$ can be written as:

$$y^s_m(c_-) = c_1\, y^s_{m,1}(c_-) + c_2\, y^s_{m,2}(c_-) + c_3\, y^s_{m,3}(c_-)\,, \tag{2.223}$$

where $m = 1, 2, ..., 6$ and c_1, c_2, c_3 are integration constants.
On the fluid side of the interface, the shear stress is null so that at the interface we have:

$$\begin{aligned} y^s_4 &= c_1\, y^s_{4,1} + c_2\, y^s_{4,2} + c_3\, y^s_{4,3} = 0 \\ c_3 &= -c_1\,\frac{y^s_{4,1}}{y^s_{4,3}} - c_2\,\frac{y^s_{4,2}}{y^s_{4,3}}\,, \end{aligned} \tag{2.224}$$

hence each component of $\vec{y}_s$ is in form:

$$y_m^s(c_-) = c_1 \left[y_{m,1}^s(c_-) - \frac{y_{4,1}^s}{y_{4,3}^s}\, y_{m,3}^s(c_-) \right] + c_2 \left[y_{m,2}^s(c_-) - \frac{y_{4,2}^s}{y_{4,3}^s}\, y_{m,3}^s(c_-) \right] . \tag{2.225}$$

In order to constrain another integration constant, boundary conditions (2.207) and (2.210) are still valid and making K_2 explicit as:

$$K_2 = \frac{y_3^s(c_-)}{\rho_0^f\, g_0(c)} , \tag{2.226}$$

we reach the condition:

$$y_1^s(c_-) = -\frac{y_5^s(c_-)}{g_0(c)} + \frac{y_3^s(c_-)}{\rho_0^f\, g_0(c)} . \tag{2.227}$$

Inserting Eq. (2.225) for each component that appears in Eq. (2.227) we obtain:

$$c_2 = -c_1 \frac{\left[y_{1,1}^s - \frac{y_{4,1}^s}{y_{4,3}^s}\, y_{1,3}^s \right] + \frac{1}{g_0(c)} \left[y_{5,1}^s - \frac{y_{4,1}^s}{y_{4,3}^s}\, y_{5,3}^s \right] - \frac{1}{\rho_0^f\, g_o(c)} \left[y_{3,1}^s - \frac{y_{4,1}^s}{y_{4,3}^s}\, y_{3,3}^s \right]}{\left[y_{1,2}^s - \frac{y_{4,2}^s}{y_{4,3}^s}\, y_{1,3}^s \right] + \frac{1}{g_0(c)} \left[y_{5,2}^s - \frac{y_{4,2}^s}{y_{4,3}^s}\, y_{5,3}^s \right] - \frac{1}{\rho_0^f\, g_o(c)} \left[y_{3,2}^s - \frac{y_{4,2}^s}{y_{4,3}^s}\, y_{3,3}^s \right]} . \tag{2.228}$$

If we rewrite c_2 as: $c_2 = -c_1 W$, where W is the constant fractional term in Eq. (2.228), and insert both c_2 and c_3 into Eq. (2.225), we obtain the relation:

$$\vec{y}_s = c_1 \vec{w} , \tag{2.229}$$

where:

$$\vec{w} = \left[\vec{y}_{s,1} - \frac{y_{4,1}^s}{y_{4,3}^s}\, \vec{y}_{s,3} \right] - W \left[\vec{y}_{s,2} - \frac{y_{4,2}^s}{y_{4,3}^s}\, \vec{y}_{s,3} \right] . \tag{2.230}$$

Thanks to the validity of Eq. (2.222), the solution that is numerically integrated into the fluid layer is:

$$\vec{y}_f = \begin{pmatrix} y_5^f \\ y_7 \end{pmatrix} = \begin{pmatrix} w_5 \\ w_6 - 4\pi G \dfrac{w_3}{g_0(c)} \end{pmatrix} . \tag{2.231}$$

4 Surface boundary conditions

For all the planetary models presented in this thesis, we consider a solid surface as the outermost layer. So, after having carried out the numerical integration from the planetary center upward to the surface, we have a solution of deformation as a linear combination of the three sets of solid solutions integrated up to there. In order to evaluate the constants that define the precise linear combination for the solution vectors (2.162), (2.174) in each perturbing case, we must apply proper surface boundary conditions related to the source of perturbation acting on the planet.
The following surface boundary conditions are valid for both compressible and incompressible cases.

The three possible sources of planetary deformations are:

- **External tidal potential**
  If there is a massive perturbing source located in space outside the planetary body, this will manifest deformations of its surface that are called *tidal deformations* or *tides* [Francioni, 2024]. The main cause of these uplifts and downlifts of the surface is the difference between the gravitational force exerted on material points of the planet and its center. Examples of tidal deformations are the tides that the Moon and the Sun exert on the Earth.

  If we consider a positive unit external gravitational potential, called *tide-raising potential* Ω_2, perturbing a planet of radius a, the planetary surface $r = a$ is a stress-free surface as a direct consequence of the contactless action of Ω_2 on the planet:

$$y_3(r = a) = 0\,, \tag{2.232}$$

$$y_4(r = a) = 0\,. \tag{2.233}$$

  The gravitational potential variation ϕ_1 induced on the planet is the sum of the external gravitational potential ϕ_2, defined conventionally as: $\phi_2 = -\Omega_2$, and the additive potential variation ϕ_3 caused by the redistribution of the mass of the planet associated to the deformation.
  Inserting these considerations into Gauss's law and assuming a harmonic nature for ϕ_3 [Spada et al., 2025], it is possible to write the third surface boundary condition as:

$$y_6(r = a) = \frac{2n+1}{a}\,. \tag{2.234}$$

The tidal surface boundary conditions to obtain the proper linear combination constants are:

$$\begin{cases} y_3(r=a) = 0 \\ y_4(r=a) = 0 \\ y_6(r=a) = \dfrac{2n+1}{a} \end{cases} \tag{2.235}$$

- **Surface mass loading**
  If there is a massive perturbing source located directly on the planetary surface, this becomes deformed under normal stresses. Examples of mass loads that can deform a planetary surface are large mountain chains, glaciers and fluid masses like oceans and atmosphere, too.

  If we consider a positive unit mass loading potential related to a mass load on the planetary surface, the condition (2.234) for y_6 is still valid as in the tidal case. The difference is that now there is a non-null condition for the radial stress, that can be evaluated as in [Spada et al., 2025] as:

$$y_3(r=a) = \frac{(2n+1)\, g_S}{4\pi G a}\,, \tag{2.236}$$

  where $g_S = g_0(r=a)$ is the gravity acceleration at the surface.
  The mass loading boundary conditions to obtain the proper linear combination constants are:

$$\begin{cases} y_3(r=a) = \dfrac{(2n+1)\, g_S}{4\pi G a} \\ y_4(r=a) = 0 \\ y_6(r=a) = \dfrac{2n+1}{a} \end{cases} \tag{2.237}$$

- **Surface shear forces**
  If there is a surface shear forcing, tangentially directed on the surface itself, the planet manifests a deformation response too. An example of shear forcing acting on a planetary scale is the motion of tectonic plates.

  If we consider a positive unit shear force acting on the planetary surface, there are no radial stresses and no potential involved in the deformation. The only condition required for it is related to the tangential stress exerted by the shear force [Saito, 1978]:

$$y_4(r=a) = \frac{(2n+1)\, g_S}{4\pi G a\, n(n+1)}\,. \tag{2.238}$$

The shear forcing boundary conditions to obtain the proper linear combination constants are:

$$\begin{cases} y_3(r = a) = 0 \\ y_4(r = a) = \dfrac{(2n + 1)\, g_S}{4\pi G a\, n(n + 1)} \\ y_6(r = a) = 0 \end{cases} \tag{2.239}$$

5 Love numbers

Love numbers (LNs) are dimensionless coefficients that indicate the intensity of planetary deformability in response to a perturbation source. They depend on the internal structure of the planet to which they refer and this can be used to infer constraints on the differentiation of planetary interiors.
The first formulation of these coefficients was made by A.E.H. Love in [Love, 1911] for tidal deformations. He assumed that, for small deformations, each harmonic component of the radial (vertical) displacement u_r induced on a point on the planetary surface is proportional by a certain factor h to the external tidal potential Ω_2 according to:

$$u_r = h\, \frac{\Omega_2}{g_S}\,. \tag{2.240}$$

Love also hypothesized that the deformation generated by the external tidal potential induces a variation in the total potential acting on the considered point that, for small deformations, is proportional by a factor k to Ω_2 itself:

$$\Omega_3 = k\, \Omega_2\,, \tag{2.241}$$

where we have followed the notation of the subscripts used in Section 4.
A similar relation to Eq. (2.240) was later considered by T. Shida in [Shida, 1912] for the tangential displacement u_θ, with a proportionality factor l:

$$u_\theta = l\, \frac{\Omega_2}{g_S}\,. \tag{2.242}$$

The dimensionless coefficients h, k and l are now known as *tidal Love numbers* (TLNs), or radial, potential and tangential TLN respectively, and they fully describe the deformation response to tidal forces exerted on a planetary body by external potentials [Munk and MacDonald, 1975, Melchior, 1983]. For a perfectly rigid body, $h = k = l = 0$. Love numbers are generally indicated as h_n, k_n and l_n to highlight the harmonic degree n of the external tidal potential to which they refer (this applies also to the other types of LNs that we will see later).

There are only a few simple planetary models that allow analytical formulation for TLNs [Wu and Ni, 1996] due to the complexity of the phenomenon. One of the most important is the Kelvin sphere, *i.e.* a spherically symmetric, self-gravitating, non-rotating, elastic body that is fully homogeneous and incompressible, first introduced by W. Thomson in [Thomson, 1863]. For this specific case, TLNs of generic harmonic degree n can be calculated from the following relations:

$$h_n = \frac{2n+1}{2(n-1)\left(1+\frac{2n^2+4n+3}{n}F\right)}, \tag{2.243}$$

$$k_n = \frac{3}{2(n-1)\left(1+\frac{2n^2+4n+3}{n}F\right)}, \tag{2.244}$$

$$l_n = \frac{3}{2n(n-1)\left(1+\frac{2n^2+4n+3}{n}F\right)}, \tag{2.245}$$

where the non-dimensional number:

$$F = \frac{\mu}{\rho g a} \tag{2.246}$$

represents the ratio between the amplitude of the elastic forces and the gravitational forces manifested by the planet [Francioni, 2024].

The previous discussion is also valid for mass loading deformations and the related LNs are called *Load Love numbers* (LLNs), indicated as h', k', l'. LLNs still verify the Love formulations (2.240), (2.241) and (2.242) illustrated for the tidal case, substituting the tide-raising potential with the potential related to the considered load.
If we consider shear forcing perturbations, the related LNs are called *Shear Love numbers* (SLNs), indicated as h'', k'', l'' and first introduced by M.Saito in [Saito, 1978]. While the vertical and the tangential SLNs still verify the Love formulations (2.240) and (2.242), the potential SLN is slightly different from its tidal and loading counterparts: in fact, shear forces are not related to any perturbing potential and k'' is properly modified to account this, as we will see later.

As previously exposed, in absence of analytical formulas for each planetary model and for each type of LNs, the only possible approach to evaluate these coefficients is obtaining them from a numerical description of the deformation. The formulation of LNs in each perturbative case can be written as follows:

- **TLNs**
  Consider a positive unit tide-raising potential Ω_2, then the TLNs at the surface associated with tidal deformations of the planet can be evaluated as:

$$\begin{cases} h_n = -g_S\, y_1(r=a) \\ k_n = y_5(r=a) - 1 \\ l_n = -g_S\, y_2(r=a) \end{cases} \tag{2.247}$$

  The signs are consistent with Eqs. (C.362) in [Spada et al., 2025].
  TLNs values are obtained applying the tidal boundary conditions (2.235) to produce the correct linear combination for solution $\vec{y} = (y_1,\, y_2,\, y_3,\, y_4,\, y_5,\, y_6)^T$.

- **LLNs**
  Consider a positive unit loading potential, then the LLNs at the surface associated with load deformations of the planet can be evaluated as:

$$\begin{cases} h'_n = -g_S\, y_1(r=a) \\ k'_n = y_5(r=a) - 1 \\ l'_n = -g_S\, y_2(r=a) \end{cases} \tag{2.248}$$

  The signs are consistent with Eqs. (C.362) in [Spada et al., 2025].
  LLNs values are obtained applying the mass loading boundary conditions (2.237) to produce the correct linear combination for solution $\vec{y} = (y_1,\, y_2,\, y_3,\, y_4,\, y_5,\, y_6)^T$.

- **SLNs**
  Consider a unit shear force, then the SLNs at the surface associated with shear deformations of the planet can be evaluated as:

$$\begin{cases} h''_n = g_S\, y_1(r=a) \\ k''_n = y_5(r=a) \\ l''_n = g_S\, y_2(r=a) \end{cases} \tag{2.249}$$

  Due to the absence of a perturbing potential that has opposite sign with respect to the planetary potential variation, the signs are already consistent with the physics of the problem. The conditions are consistent with [Saito, 1978].
  SLNs values are obtained applying the shear forcing boundary conditions (2.239) to obtain the correct linear combination for solution $\vec{y} = (y_1,\, y_2,\, y_3,\, y_4,\, y_5,\, y_6)^T$.

In [Saito, 1978], the author proved the validity of some empirical relations between different types of numerically-integrated Love numbers, valid for spherically symmetric, non-rotating planets. Due to the similar definition of tidal and loading LNs, except for the nature of the perturbing potential, we have:

$$h_n - k_n = -k'_n\,, \tag{2.250}$$

originally reported in Eq. (7) of [Saito, 1978].
Saito also related shear Love numbers to the tidal and load ones as:

$$l_n = -k''_n = h''_n + l'_n\,, \tag{2.251}$$

originally reported in Eq. (10) of [Saito, 1978].

As already introduced, Love numbers depend on the internal differentiation of the planet to which they refer. Even if they represent the global response of the planetary body to perturbations, it is not clear how LNs depend on a specific parameter at each depth [Okubo and Saito, 1983]. Possible solutions have been developed to solve this issue through the years: one of the most meaningful is the evaluation of partial derivatives of Love numbers, first introduced by S.M. Molodensky in [Molodensky, 1976, Molodensky, 1977] and later re-examined also in [Okubo and Saito, 1983]. Due to the complexity of the method, we have chosen another approach to study the dependencies shown by LNs: the generation of a range of values for a selected parameter of the model, as illustrated in the following Chapter.

Chapter 3

Numerical code and models

1 Structure of the code

The code I have developed to numerically evaluate the LNs of an Earth-like planet is structured in many function blocks that, given in input the planetary interior model, integrate the starting sets of deformation solutions via fourth order Runge-Kutta method upward to the surface and produce in output the LNs results. The user can also select a parameter of the model to test in a wide range of realistic values, setting the central value, the width, and the step between adjacent values of this range. The resulting plots show LNs related to different possible values of the selected planetary parameter, not only to a specific value.

The complete MATLAB code is available at:
`https://github.com/lfrancioni/Love-numbers-of-super-Earths` [Francioni, 2026], in two versions: for fully solid models refer to the repository `FS_model`, while for fluid outer core models refer to the repository `FOC_model`, available in both the repositories `Earth_code` and `super-Earths_code`. Each version produces both compressible and incompressible LNs results for the specific planetary model set in the code. In the following discussion, every time we cite a function with the term `solid` or `fluid` in its name, we are referring to the nature of the layer to which the function applies.

1.1 Setting functions

The interior model is set in the following functions.

- In the function `set_parameters`, the planetary radius `a` and the external radii of each layer are set, in units of $[m]$. The density profile `rho_profile`, in units of $\left[\frac{kg}{m^3}\right]$, and the elastic profiles of shear modulus `mu_profile` and Lamé's first parameter lambda_profile, both in units of $[Pa]$, are set too.

- In the function set_integration, the integration step step and the integration starting radius r0 are set, both in units of $[m]$. Then, the vector of the radial variable r, which defines the radial sampling of the planet from r_0 to a, and its length N are initialized from the previous variables.

- In the function normalize, all the previous variables are normalized in order to not generate any NaN or infinite values that would introduce singularities in the code. The scales that can be selected are: the length scale L_scale, in units of $[m]$; the density scale Rho_scale, in units of $\left[\frac{kg}{m^3}\right]$.
  The time scale T_scale, used to normalize the elastic parameters, is obtained as:
$$\texttt{T\_scale} = \frac{1}{\sqrt{\texttt{Rho\_scale} \cdot G\pi}}, \tag{3.1}$$
  following the normalization scheme presented previously in [Martens, 2016].
  The default settings are L_scale = a and Rho_scale = $\overline{\rho}$, where $\overline{\rho}$ is the average density evaluated from the values of rho_profile.

1.2 Get functions

Certain functions are defined in order to extract the correct value of a quantity that is needed at a specified radius value.

- The function get_parameter extracts from the selected profile the value of the specified parameter corresponding to the input radius.

- The function get_g calculates the gravity acceleration g corresponding to the input radius using Eq. (2.3).

1.3 Integration functions

The numerical integration is carried out employing many functions, each one playing a specific role of the theory exposed above.

- In the functions system_solid_com (compressible case), system_solid_incom (incompressible case) and system_fluid, the ODEs matrices (2.86), (2.172) and (2.201) are multiplied by the $\vec{y}$ solution of the considered step to produce its derivative.

- The functions `RK4_solid_com`, `RK4_solid_incom` and `RK4_fluid` compute the $\vec{y}$ solution at the final radius (`index_f`) starting from the known solution `Y_s` at the initial radius (`index_i`). This step-by-step integration is performed using the fourth-order Runge-Kutta method, which is described in detail in Appendix C. Each parameter of the step, *i.e.* the elastic constants and the gravity acceleration, is evaluated in the actual step by the functions `get_parameter` and `get_g`.

- The functions `main_compressible` and `main_incompressible` represent the core of the code. Initially, the setting functions are called to set up the planetary model; in the same code lines, the choice of the parameter that would be studied in a certain range is made. Then, the full expressions of the starting solutions (2.164), (2.165), (2.166) are introduced and collected in the matrix `Y_s0`. Introducing the starting solutions for compressible solid layers implies the definition of spherical Bessel functions and their first and second derivatives in the functions named `spherical_bessel`, `d_spherical_bessel` and `dd_spherical_bessel`, respectively. For the starting solution (2.165), the possibility of pure imaginary wave number q is considered by the definition of modified spherical Bessel functions as discussed in Appendix B, in the functions `spherical_bessel_modified`, `d_spherical_bessel_modified` and `dd_spherical_bessel_modified`.
  The numerical integration is carried out as follows. For fully solid models, it starts from `r0` and ends right at the surface, while for fluid outer core models the boundary conditions (2.222) and (2.231) at the fluid-solid interfaces are applied as exposed in Sections 3.4, 3.5 of the previous Chapter. In this case, a proper matrix `Y_fluid` is initialized and integrated into the fluid layer.
  Once we have obtained the numerical solution `Y_final` at the surface, the correct constants for the linear combination of $\vec{y}$ are evaluated applying the appropriate surface boundary conditions (2.235), (2.237), (2.239) for the specified kind of Love numbers. Finally, the LNs are evaluated by Eqs. (2.247), (2.248), (2.249).

1.4 Launch functions

The functions to launch in order to produce LNs results from the previous code elements are the functions `Love` and `Love_fluid`.
The user should initially select the three main variables of the code:

- the LN type `Love_type`, to numerically reproduce the `Tidal`, `Load`, or `Shear` case.

- the maximum harmonic degree `N_max` to reach, from which the harmonic degree `n` is initialized, starting from $n = 2$.

- the parameter that has to be studied in a range of possible realistic values. The default choice is the shear modulus of the mantle: the central value is initialized as

mu_ref and its range is generated declaring how many values per side (higher and lower than the central value) there will be and the spacing between each of them, named n_steps_per_side and variation, respectively.
This default is chosen according to [Kamata et al., 2016] and other works, which verified how LNs are more sensitive to the characteristics of the mantle and the crust than to the deep interior.

Then, the matrices containing the LNs results for each harmonic degree and each tested parameter value are initialized and filled with the results of main functions.
Finally, the plots for each case are displayed, divided into compressible and incompressible cases.

2 Testing

In order to test the validity of the code, the first check we have carried out is the comparison between the numerical results of Love numbers of the Earth and their analytical formulas for Kelvin sphere, given by Eqs. (2.243), (2.244) and (2.245). The average planetary parameters used in the code for the homogeneous, incompressible case are reported in Tab. 3.1.
The agreement between the two methods is shown in Tab. 3.2 by comparing the results up to the harmonic degree $n = 25$.

	$\boldsymbol{a}\ [\boldsymbol{km}]$	$\boldsymbol{\rho}\ \left[\frac{\boldsymbol{kg}}{\boldsymbol{m^3}}\right]$	$\boldsymbol{\mu}\ [\boldsymbol{GPa}]$
Average value	6370	5500	145

Table 3.1: **Kelvin model of the Earth**
Average values of radius a, density ρ and shear modulus μ of the homogeneous, incompressible Earth adapted from [Wu and Peltier, 1982].

The Kelvin sphere is an useful model to test the code because, even if it is a simple approximation of a realistic planet, it can provide us a first description of the parametric response of Love numbers, at least in the incompressibility hypothesis. For example, by varying the a, ρ, μ values used to define the Kelvin sphere in Tab. 3.1 we can obtain the dependence of h_n as reported in Fig. 3.1. With respect to the reference model, we observe that: an increase in radius will increase h_n, with ρ, μ remaining the same; an increase in density will increase h_n, with a, μ remaining the same; an increase in shear modulus will decrease h_n, with a, ρ remaining the same. These trends confirm the behavior of the analytical formula (2.243), and specifically the role played by the F constant, already defined in Eq. (2.246). It is possible to confirm the same behavior for k_n and l_n too.

TLN	n	**Analytical result**	**Numerical result**
h	2	0.4983	0.4983
	3	0.3097	0.3097
	4	0.2347	0.2347
	...		
	10	0.1035	0.1035
	...		
	25	0.0445	0.0445
k	2	0.2990	0.2990
	3	0.1327	0.1327
	4	0.0782	0.0782
	...		
	10	0.0148	0.0148
	...		
	25	0.0026	0.0026
l	2	0.1495	0.1495
	3	0.0442	0.0442
	4	0.0196	0.0196
	...		
	10	0.0015	0.0015
	...		
	25	$1.0468 \cdot 10^{-4}$	$1.0468 \cdot 10^{-4}$

Table 3.2: **Analytical vs numerical TLNs for Kelvin model**
Analytical results of the TLNs of Kelvin model are computed according to Eqs. (2.243), (2.244) and (2.245). Numerical results of the TLNs of Kelvin model are evaluated by the code according to Eqs. (2.247), using the data in Tab. 3.1.

These parametric response of TLNs have already been observed and verified in literature for many types of solar planetary bodies [Zhang, 1992].

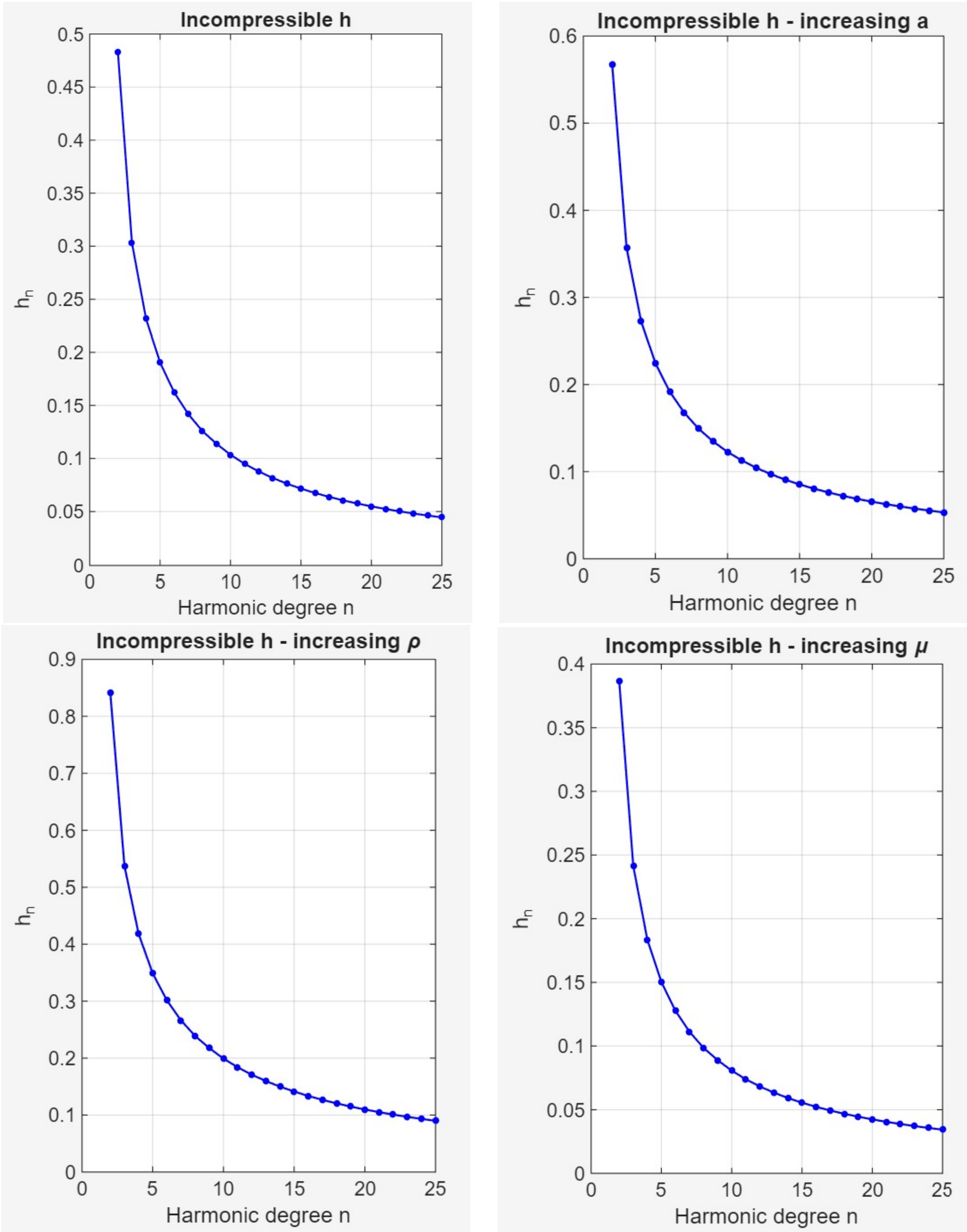

Figure 3.1: *Parametric dependencies of radial tidal Love number h_n for Kelvin sphere. The upper left image reports the reference values for data in Tab. 3.1. The upper right image reports the values for a Kelvin sphere with a larger radius: $a = 7000\,km$. The lower left image reports the values for a Kelvin sphere with a larger density: $\rho = 8000\,\frac{kg}{m^3}$. The lower right image reports the values for a Kelvin sphere with a larger shear modulus: $\mu = 190\,GPa$.*

An useful approximation assumed in the code is the following: for fully solid models, starting the numerical integration near the center of the planet ($r \simeq 0$) produces regular trends for LNs results at low harmonic degrees, but after about $n = 20$ they will start to oscillate under the influence of numerical noise. In order to improve the quality of the results and produce a description of deformation up to $n = 100$ and beyond, we have decided to start the integration right below the Core-Mantle boundary (CMB) in fully solid models. This is possible since we assume that the inner core is homogeneous, hence the starting solutions (2.164), (2.165), (2.166), (2.175) and (2.206) are valid at any radius inside it.
Starting from the CMB, the variations in LNs values we have obtained are at maximum of 0.8 % of the LNs values obtained starting from near the center for the compressible case, and at maximum of 3 % for the incompressible one. We consider this numerical integration to be more reasonable than the one starting from the center, due to the reduction of numerical noise.

3 Input models

In this work, Love numbers evaluation for the Earth and super-Earths of different masses is carried out. Even if LNs values of the Earth have been already presented in geophysical literature, thanks to the code previously introduced we produce a new set of LNs of each type that we will discuss later alongside the results for super-Earths.

Every model we present is made up of various layers with different elastic nature, each one described by four parameters: the radial thickness ΔR inside the planet, starting from the center; the density ρ; the shear modulus μ; and the first Lamé's parameter λ.

3.1 The Earth models

The rheological differentiation of the interior of the Earth presented in [Belardinelli, 2025] is adopted for our models. We set its total radius as: $a = 6370\,km$, for convenience in the implementation of the code. For both compressible and incompressible cases, Earth is initialized through the following two different interior models:

- a fully solid differentiation, made up of a heavy core of pure Fe, a mantle of Mg and Si compounds in the form of olivine and its denser $MgSiO_3$ perovskite structure, and a thin crust of SiO mixed with other elements.
  This interior model, renamed as *E-FS (Earth - Fully Solid)*, is reported in Tab. 3.3 and displayed in Fig. 3.2;

- the second model is formally equal to the previous one, but the core is divided in a solid inner core and a fluid outer core, both of pure Fe. This modeling is more suitable for the current understanding of the interior of the Earth, reconstructed thanks to the seismic waves propagation data [Dziewonski and Anderson, 1981]. This interior model, renamed as *E-FOC (Earth - Fluid Outer Core)*, is reported in Tab. 3.4 and displayed in Fig. 3.2.

The density and elastic parameters have been calculated following the same approach presented in [Poulsen, 2009]: ρ is evaluated in each layer as the average of the density values of PREM [Dziewonski and Anderson, 1981], while μ and λ are indirectly obtained from the PREM seismic velocity data in [Dziewonski and Anderson, 1981] through Eqs. (2.100) and (2.104).

Layer	$\boldsymbol{\Delta R}$ $[\boldsymbol{km}]$	$\boldsymbol{\rho}$ $\left[\frac{\boldsymbol{kg}}{\boldsymbol{m^3}}\right]$	$\boldsymbol{\mu}$ $[\boldsymbol{GPa}]$	$\boldsymbol{\lambda}$ $[\boldsymbol{GPa}]$
Core	$0 - 3480$	11000	0.25	960
Mantle	$3480 - 6290$	4800	190	300
Crust	$6290 - 6370$	3200	57	70

Table 3.3: ***E-FS* model**
Interior model of the Earth made up of three fully solid layers, according to a generalization of [Belardinelli, 2025]. In each layer, ρ, μ, λ are obtained from [Dziewonski and Anderson, 1981] following the approach of [Poulsen, 2009] based on the average data.

Layer	$\boldsymbol{\Delta R}$ $[\boldsymbol{km}]$	$\boldsymbol{\rho}$ $\left[\frac{\boldsymbol{kg}}{\boldsymbol{m^3}}\right]$	$\boldsymbol{\mu}$ $[\boldsymbol{GPa}]$	$\boldsymbol{\lambda}$ $[\boldsymbol{GPa}]$
Inner Core	$0 - 1220$	12900	170	1270
Outer Core	$1220 - 3480$	11000	0	940
Mantle	$3480 - 6290$	4800	190	300
Crust	$6290 - 6370$	3200	57	70

Table 3.4: ***E-FOC* model**
Interior model of the Earth with a fluid outer core, according to [Belardinelli, 2025]. In each layer, ρ, μ, λ are obtained from [Dziewonski and Anderson, 1981] following the approach of [Poulsen, 2009]. In order to state the inviscid fluid nature of outer core, we set $\mu = 0$ in that layer.

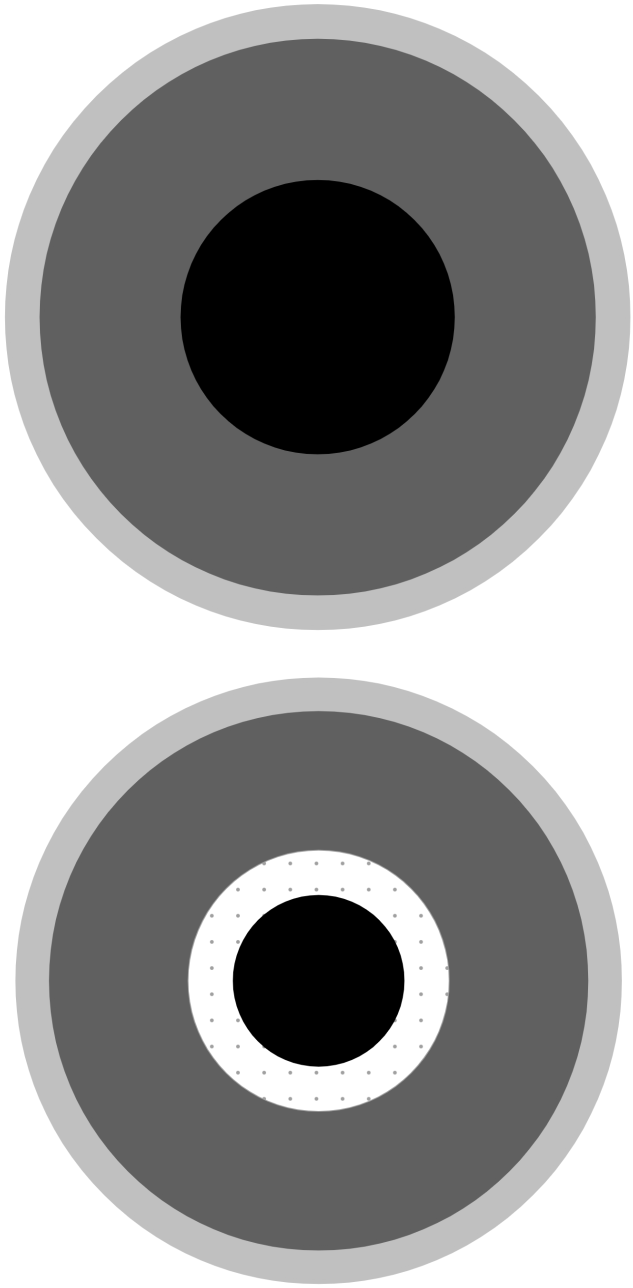

Figure 3.2: *The upper illustration is the graphical representation of a fully solid (FS) model of a rocky planetary interior: the black layer is the core, the dark grey layer is the mantle and the pale grey layer is the crust. The lower illustration is the graphical representation of a fluid outer core (FOC) model of a rocky planetary interior: the black layer is the solid inner core, the dotted white layer is the fluid outer core, the dark grey layer is the mantle and the pale grey layer is the crust. Radial thicknesses are not in scale.*

3.2 Super-Earths models

To produce realistic models for rocky super-Earths of different masses, we expose the complete method we have developed to build such a model, starting only from the mass of the investigated planet.

Consider a rocky super-Earth with mass M. The most general description of the interior of this kind of planet is based on an Earth-like differentiation, except for the main materials that compose the deepest layers: instead of pure Fe, the core is assumed to be made of hpc-Fe, *i.e.* high-pressurized Fe; instead of $MgSiO_3$ perovskite, the higher internal pressure of the mantle of super-Earths induces the transition of $MgSiO_3$ in its post-perovskite structure, that has a different elastic behavior with respect to perovskite; the crust is assumed to be made of SiO and mixed elements, as for the Earth. These materials are assumed to be isotropic so that we can employ the deformation theory exposed in Chapter 2, even though the isotropic assumption simplifies the real anisotropic behavior of post-perovskite structures [Oganov and Ono, 2004]. The elastic properties of these materials were already been confirmed in [Tsuchiya et al., 2004, Singh et al., 2023].

In Fig. 5 of [Valencia et al., 2006] the authors presented a power-law proportionality relation between mass and radius of super-Earths, valid for many internal models based on the materials mentioned above, in form:

$$R \propto M^{\alpha}\,, \tag{3.2}$$

where $0 < \alpha < 1,\ \alpha \in \mathrm{R}$ is an exponent depending on the internal differentiation of the planet.
Similar relations were presented also for core radius R_c and mantle radial thickness ΔR_m with proper exponents β and γ:

$$R_c \propto M^{\beta}\,, \tag{3.3}$$

$$\Delta R_m \propto M^{\gamma}\,. \tag{3.4}$$

As already pointed out, the Earth itself can be considered as a limit case of super-Earth having $M = 1\,M_\oplus$, so that the previous Eqs. (3.2), (3.3) and (3.4) are valid for its radial quantities and mass too. We can obtain the proportionality constants of each relation as:

$$R_\oplus = c\,M_\oplus^{\alpha} \implies c = \frac{R_\oplus}{M_\oplus^{\alpha}}\,. \tag{3.5}$$

Analogous constants can be obtained for core radius and mantle radial thickness relations.

For the specific cases investigated in this work, we have obtained the following relations:

- *Fully solid models*

$$R = R_\oplus \left(\frac{M}{M_\oplus}\right)^{0.268} , \quad R_c = R_{c,\oplus} \left(\frac{M}{M_\oplus}\right)^{0.247} , \quad \Delta R_m = \Delta R_{m,\oplus} \left(\frac{M}{M_\oplus}\right)^{0.294} , \tag{3.6}$$

- *Fluid outer core models*

$$R = R_\oplus \left(\frac{M}{M_\oplus}\right)^{0.271} , \quad R_c = R_{c,\oplus} \left(\frac{M}{M_\oplus}\right)^{0.244} , \quad \Delta R_m = \Delta R_{m,\oplus} \left(\frac{M}{M_\oplus}\right)^{0.3} , \tag{3.7}$$

where each exponent is taken from Fig. 5 of [Valencia et al., 2006].

The density profile of each super-Earth class is taken from Fig. 3 of [Valencia et al., 2006]: for each super-Earth size and for each considered layer, we have obtained the most appropriate average density value by calculating the average density in the range of depths corresponding to that layer.

It is impossible to study in the laboratory the physical properties of materials that compose the deepest layers of super-Earths: the extremely high pressures that characterize these planets, up to $1\,TPa$, are not reproducible with mechanical instrumentation. In [Mao et al., 2001] and [Tsuchiya et al., 2004] the dependence on pressure of shear modulus μ and bulk modulus K are reported for hpc-Fe and $MgSiO_3$ post-perovskite, respectively. In both these works, the pressure range that has been tested is quite far from the pressure regimes found inside super-Earths: it was at maximum until $400\,GPa$ for hpc-Fe and until $180\,GPa$ for $MgSiO_3$ post-perovskite. Using the data reported in these papers, we have reproduced the fitting plots in Figs. 3.3, 3.4 and extended them up to more than $1\,TPa$, in order to reconstruct the appropriate pressures exerted on the internal components of super-Earths.
The most suitable pressure values for each internal layer of super-Earths, depending on the planetary mass, are taken from Fig. 4 of [Sotin et al., 2007]. By extracting the values of μ, K at these specific pressure points, all reported in Tabs. 3.6 and 3.7, we have obtained a profile of μ and λ associated to the different super-Earth models. λ values are obtained from K values applying Eq. (2.10).

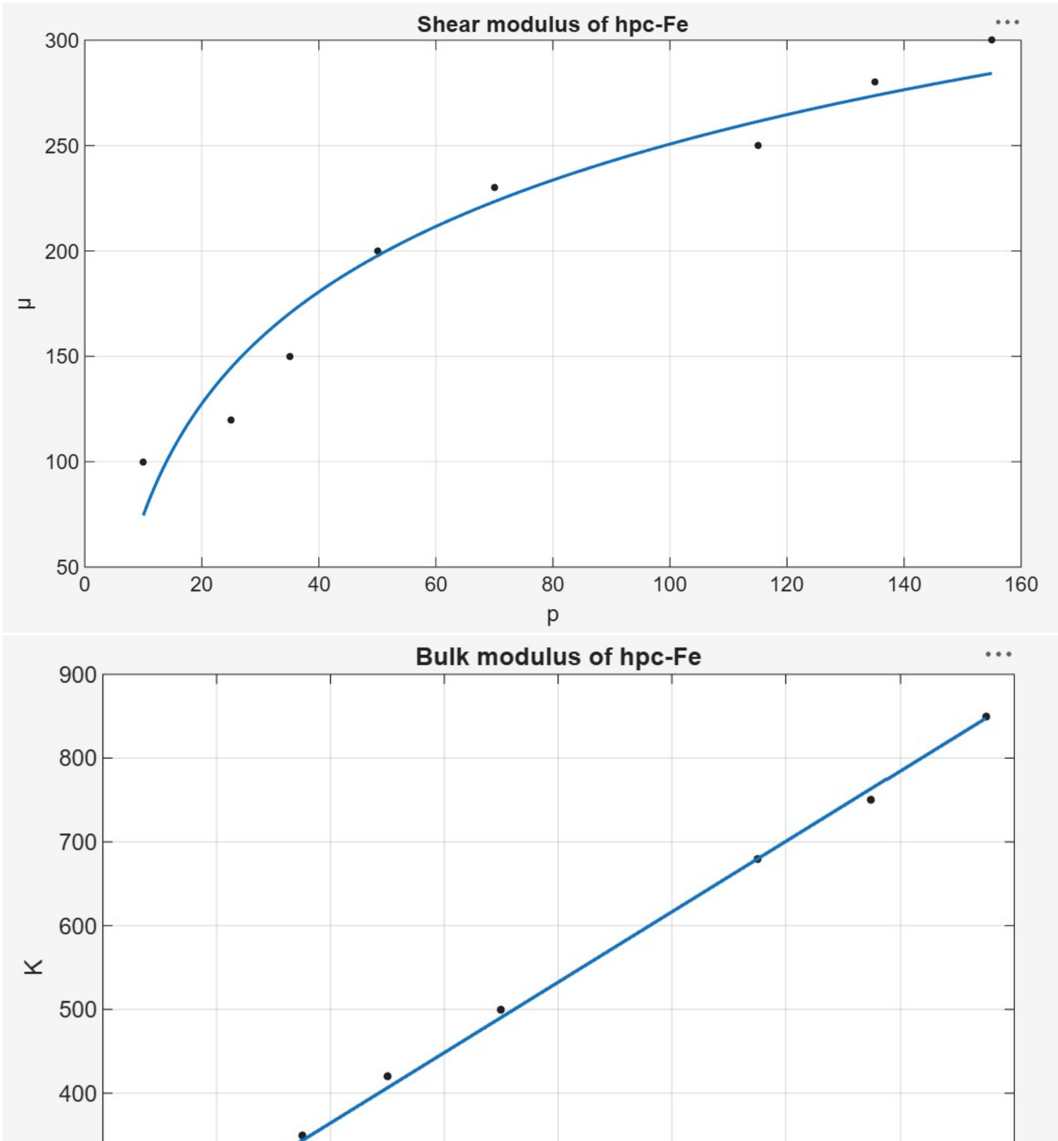

Figure 3.3: *Data fitting of shear modulus μ and bulk modulus K of hpc-Fe using the data originally reported in Fig. 3 of [Mao et al., 2001]. We considered a logarithmic fit as the most representative trend for shear modulus data and a linear fit as the most representative for bulk modulus data.*

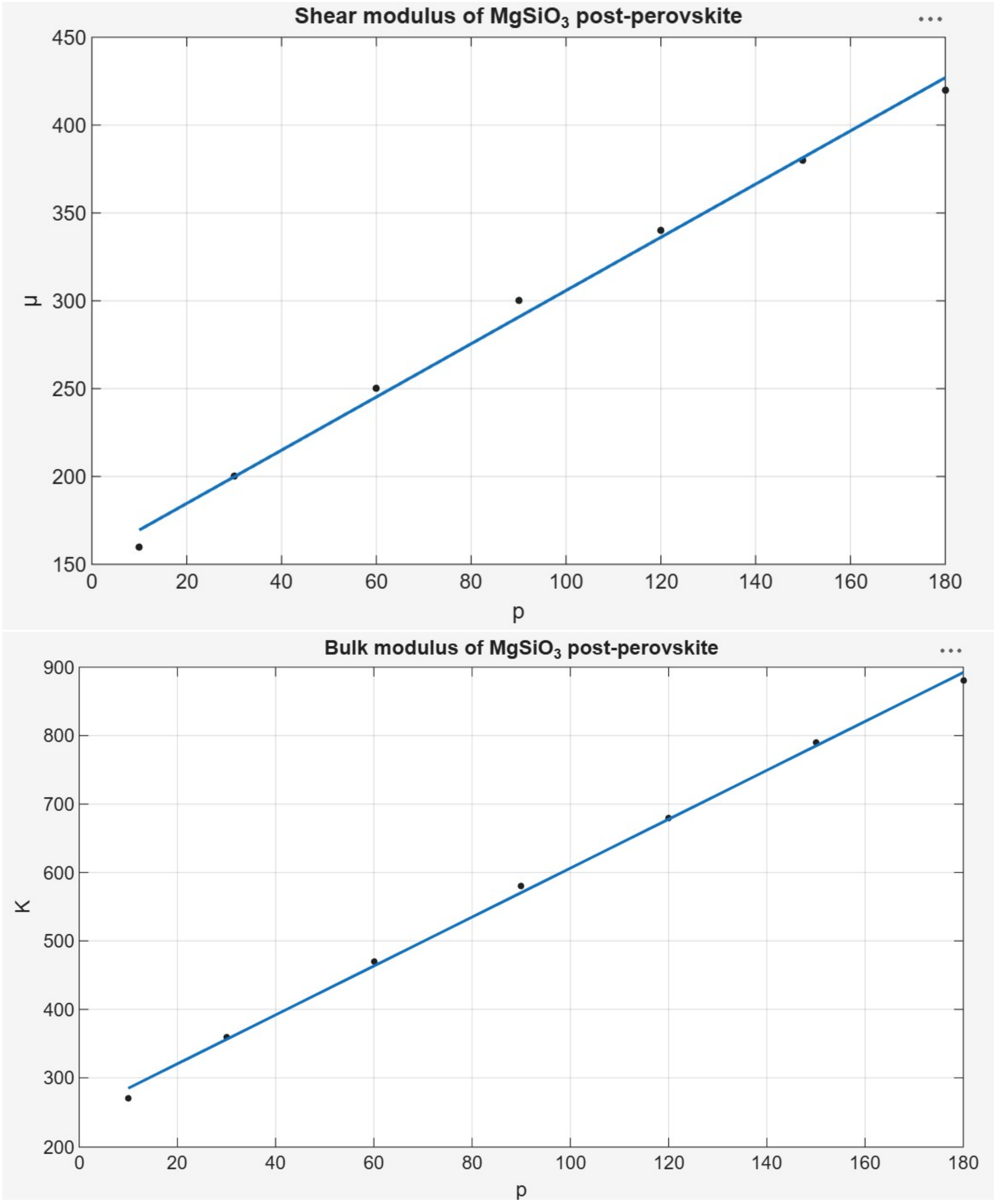

Figure 3.4: *Data fitting of shear modulus μ and bulk modulus K of $MgSiO_3$ post-perovskite using the data originally reported in Fig. 2 of [Tsuchiya et al., 2004]. We considered a linear fit as the most representative trend for both shear modulus and bulk modulus data.*

Based on exoplanetary population statistics reported in Fig. 1.1, we have decided to study three kinds of super-Earths in different mass regimes:

- **super-Earth with $\boldsymbol{M = 2\,M_\oplus}$**, likely to be the most similar in size and structure to the Earth. This kind of planet will be investigated through both a fully solid model, renamed as *SE2-FS (Super-Earth* $2\,M_\oplus$ *- Fully Solid)* and reported in Tab. 3.8, and a fluid outer core model, renamed as *SE2-FOC (Super-Earth* $2\,M_\oplus$ *- Fluid Outer Core)* and reported in Tab. 3.9. As justified by [Valencia et al., 2006], the Earth size is considered as the limit planetary case that allows the presence of a fluid outer core, due to the relatively low pressure regime and the internal heat diffusion. We assume that at least the smallest super-Earth that we are going to study can be investigated in this hypothesis as well;
- **super-Earth with $\boldsymbol{M = 4\,M_\oplus}$**, as it is the most widespread super-Earth size in the observed universe. This planet will be considered only as fully solid, due to the high internal pressure regime. The model is renamed as *SE4-FS (Super-Earth* $4\,M_\oplus$ *- Fully Solid)* and reported in Tab. 3.10;
- **super-Earth with $\boldsymbol{M = 8\,M_\oplus}$**, as an example of an extremely more massive planet than the Earth, potentially very different in deformability response from it. This planet will be considered only as fully solid, due to the high internal pressure regime. The model is renamed as *SE8-FS (Super-Earth* $8\,M_\oplus$ *- Fully Solid)* and reported in Tab. 3.11.

All the calculated planetary radii for each super-Earth model are reported in Tab. 3.5.

Model	$\boldsymbol{a}$ $[\boldsymbol{km}]$
SE2-FS	7670
SE2-FOC	7690
SE4-FS	9240
SE8-FS	11120

Table 3.5: **Planetary radii for SE models**
Planetary radii of each SE class are evaluated from the first of Eqs. (3.6) for FS models and from the first of Eqs. (3.7) for FOC model.

For all the models presented here, the μ and λ values indicate an average value for the layer they refer to. In order to produce deformability results in a wide range of elastic behaviors, and not in a single specific case, those values are considered as the central values of the range that we have tested to produce Love numbers of super-Earths, as it will be clearer in the plots in the next Chapter.

SE Mass	$\overline{p}_{core}$ $[GPa]$	μ $[GPa]$	K $[GPa]$
$2\,M_{\oplus}$	~ 500	374	2334
$4\,M_{\oplus}$	~ 900	419	4052
$8\,M_{\oplus}$	~ 1800	472	7919

Table 3.6: **Pressure-dependent elastic parameters of hpc-Fe**
Shear modulus μ and bulk modulus K values of hpc-Fe extracted from the fit in Fig. 3.3 at the most appropriate pressure of the core $\overline{p}_{core}$ for each super-Earth considered in this work. $\overline{p}_{core}$ values are taken from Fig. 4 of [Sotin et al., 2007] at the depth associated with the middle of the core, for each super-Earth size.

SE Mass	$\overline{p}_{mantle}$ $[GPa]$	μ $[GPa]$	K $[GPa]$
$2\,M_{\oplus}$	~ 150	382	786
$4\,M_{\oplus}$	~ 250	538	1148
$8\,M_{\oplus}$	~ 400	770	1692

Table 3.7: **Pressure-dependent elastic parameters of $MgSiO_3$ post-perovskite**
Shear modulus μ and bulk modulus K values of $MgSiO_3$ post-perovskite extracted from the fit in Fig. 3.4 at the most appropriate pressure of the mantle $\overline{p}_{mantle}$ for each super-Earth considered in this work. $\overline{p}_{mantle}$ values are taken from Fig. 4 of [Sotin et al., 2007] at the depth associated with the middle of the mantle, for each super-Earth size.

Layer	ΔR $[km]$	ρ $\left[\frac{kg}{m^3}\right]$	μ $[GPa]$	λ $[GPa]$
Core	0 – 4130	14000	374	2085
Mantle	4130 – 7580	6000	382	531
Crust	7580 – 7670	3000	57	70

Table 3.8: ***SE2-FS* model**
Interior model of a super-Earth of $M = 2\,M_\oplus$ *made up of three fully solid layers, following the differentiation presented in Subsection 3.2. The thickness of each layer is obtained from Eqs. (3.6).* ρ *in each layer is obtained from Fig. 3 in [Valencia et al., 2006].* μ, λ *are obtained following the method discussed above for the core and the mantle while they are assumed similar to the Earth for the crust.*

Layer	ΔR $[km]$	ρ $\left[\frac{kg}{m^3}\right]$	μ $[GPa]$	λ $[GPa]$
Inner Core	0 – 1445	16000	374	2200
Outer Core	1445 – 4120	14000	0	2085
Mantle	4120 – 7580	6000	382	531
Crust	7580 – 7690	3000	57	70

Table 3.9: ***SE2-FOC* model**
Interior model of a super-Earth of $M = 2\,M_\oplus$ *with fluid outer core, following the differentiation presented in Subsection 3.2. The thickness of each layer is obtained from Eqs. (3.7).* ρ *in each layer is obtained from Fig. 3 in [Valencia et al., 2006].* μ, λ *are obtained following the method discussed above for the inner core and the mantle while they are assumed similar to the Earth for the crust. A null shear modulus is assumed for the fluid outer core, consistently with the inviscid fluid behavior presented in Chapter 2.*

Layer	ΔR $[km]$	ρ $\left[\frac{kg}{m^3}\right]$	μ $[GPa]$	λ $[GPa]$
Core	$0 - 4900$	17000	419	3773
Mantle	$4900 - 9120$	7000	538	789
Crust	$9120 - 9240$	4000	57	70

Table 3.10: ***SE4-FS*** **model**
Interior model of a super-Earth of $M = 4\,M_\oplus$ *made up of three fully solid layers, following the differentiation presented in Subsection 3.2. The thickness of each layer is obtained from Eqs. (3.6).* ρ *in each layer is obtained from Fig. 3 in [Valencia et al., 2006].* μ, λ *are obtained following the method discussed above for the core and the mantle while they are assumed similar to the Earth for the crust.*

Layer	ΔR $[km]$	ρ $\left[\frac{kg}{m^3}\right]$	μ $[GPa]$	λ $[GPa]$
Core	$0 - 5820$	21000	472	7604
Mantle	$5820 - 11000$	8000	770	1179
Crust	$11000 - 11120$	4500	57	70

Table 3.11: ***SE8-FS*** **model**
Interior model of a super-Earth of $M = 8\,M_\oplus$ *made up of three fully solid layers, following the differentiation presented in Subsection 3.2. The thickness of each layer is obtained from Eqs. (3.6).* ρ *in each layer is obtained from Fig. 3 in [Valencia et al., 2006].* μ, λ *are obtained following the method discussed above for the core and the mantle while they are assumed similar to the Earth for the crust.*

Chapter 4

Results and Discussion

1 Results for the Earth

1.1 E-FS model

The integration of *E-FS* model is carried out starting from right under the CMB and using an integration step of $10\,km$. The results are displayed in Figs. 4.1, 4.2, 4.3 and reported up to the fifth harmonic degree in Tabs. 4.1, 4.2, 4.3, respectively for tidal, load and shear LNs.

1.2 E-FOC model

The integration of *E-FOC* model is carried out starting from near the planetary center and using an integration step of $10\,km$. The results are displayed in Figs. 4.4, 4.5, 4.6 and reported up to the fifth harmonic degree in Tabs. 4.4, 4.5, 4.6, respectively for tidal, load and shear LNs.

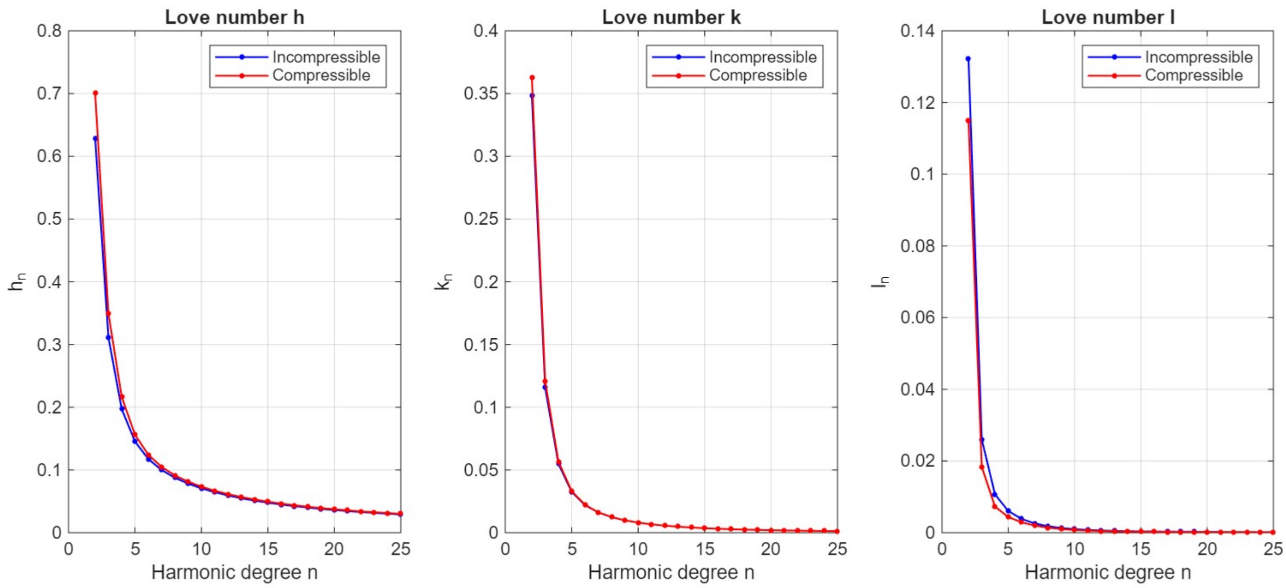

Figure 4.1: *Tidal Love numbers plots for E-FS model up to degree $n = 25$ for both compressible and incompressible cases. The input data of the model are reported in Tab. 3.3.*

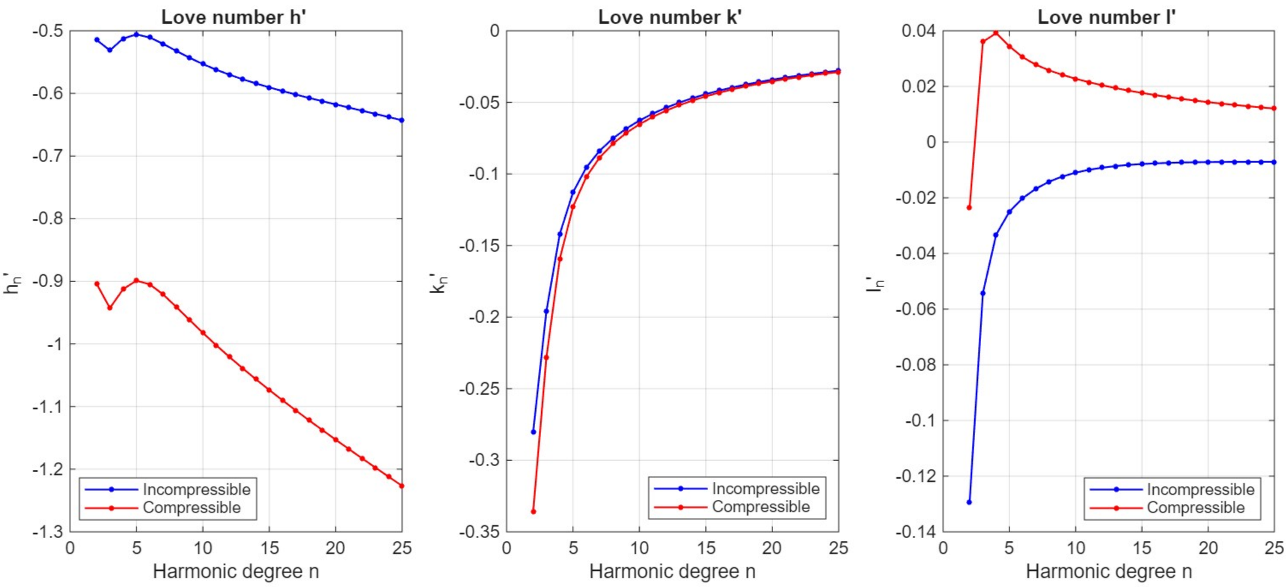

Figure 4.2: *Load Love numbers plots for E-FS model up to degree $n = 25$ for both compressible and incompressible cases. The input data of the model are reported in Tab. 3.3.*

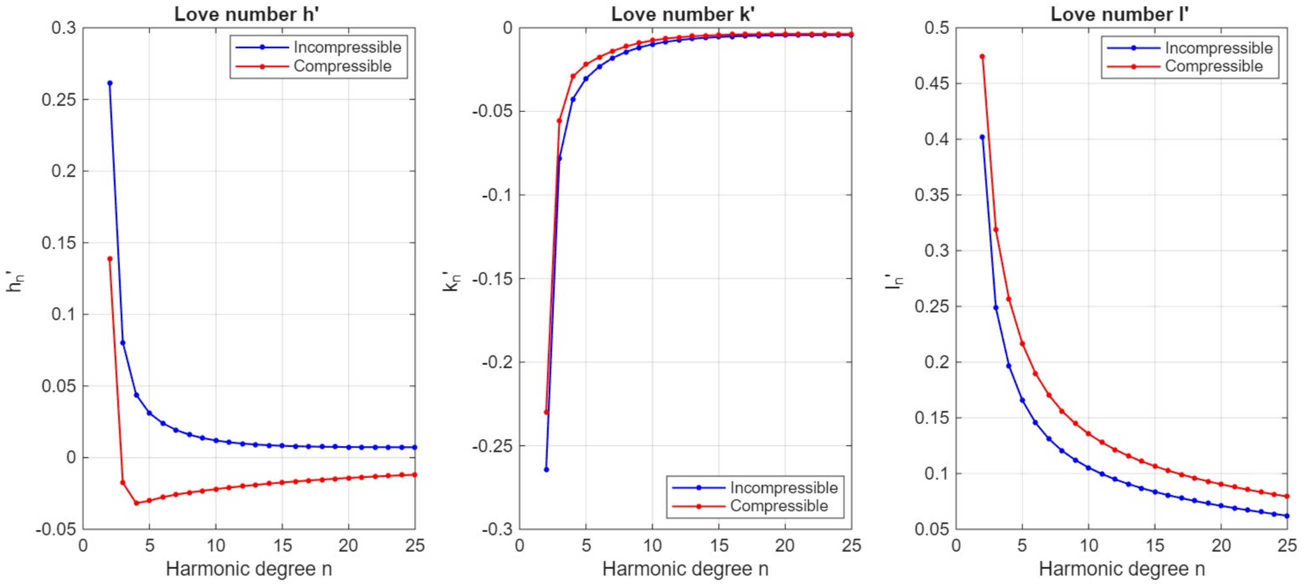

Figure 4.3: *Shear Love numbers plots for E-FS model up to degree $n = 25$ for both compressible and incompressible cases. The input data of the model are reported in Tab. 3.3.*

TLN	n	**Compressible**	**Incompressible**
h_n	2	0.7004	0.6288
	3	0.3498	0.3115
	4	0.2164	0.1970
	5	0.1562	0.1454
k_n	2	0.3625	0.3486
	3	0.1209	0.1157
	4	0.0566	0.0549
	5	0.0331	0.0325
l_n	2	0.1150	0.1322
	3	0.0184	0.0260
	4	0.0073	0.0107
	5	0.0044	0.0061

Table 4.1: **TLNs results for E-FS model**
Tidal Love numbers results for E-FS model for both compressible and incompressible cases are reported up to the fifth harmonic degree.

LLN	n	Compressible	Incompressible
h'_n	2	-0.9038	-0.5146
	3	-0.9428	-0.5313
	4	-0.9125	-0.5123
	5	-0.8990	-0.5058
k'_n	2	-0.3359	-0.2802
	3	-0.2281	-0.1958
	4	-0.1596	-0.1422
	5	-0.1230	-0.1129
l'_n	2	-0.0235	-0.1292
	3	0.0360	0.0543
	4	0.0391	0.0333
	5	0.0344	0.0250

Table 4.2: **LLNs results for E-FS model**
Load Love numbers results for E-FS model for both compressible and incompressible cases are reported up to the fifth harmonic degree.

SLN	n	Compressible	Incompressible
h''_n	2	0.1388	0.2615
	3	-0.0175	0.0803
	4	-0.0319	0.0439
	5	-0.0300	0.0311
k''_n	2	-0.2301	-0.2645
	3	-0.0555	-0.0781
	4	-0.0292	-0.0427
	5	-0.0220	-0.0303
l''_n	2	0.4743	0.4018
	3	0.3185	0.2487
	4	0.2562	0.1964
	5	0.2166	0.1657

Table 4.3: **SLNs results for E-FS model**
Shear Love numbers results for E-FS model for both compressible and incompressible cases are reported up to the fifth harmonic degree.

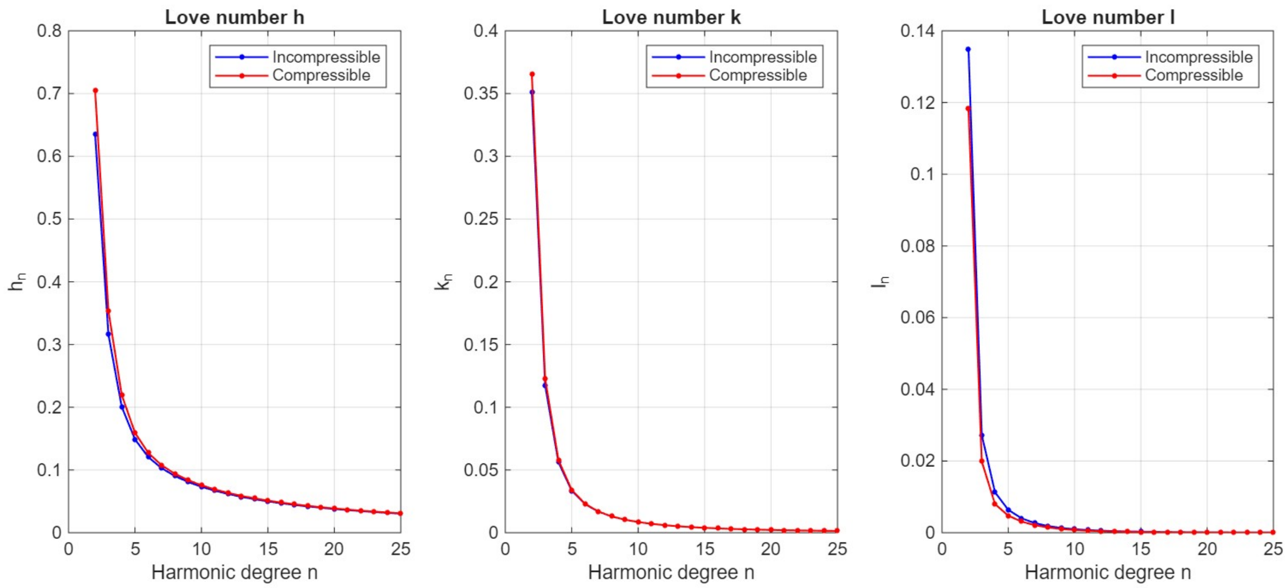

Figure 4.4: *Tidal Love numbers plots for E-FOC model up to degree $n = 25$ for both compressible and incompressible cases. The input data of the model are reported in Tab. 3.4.*

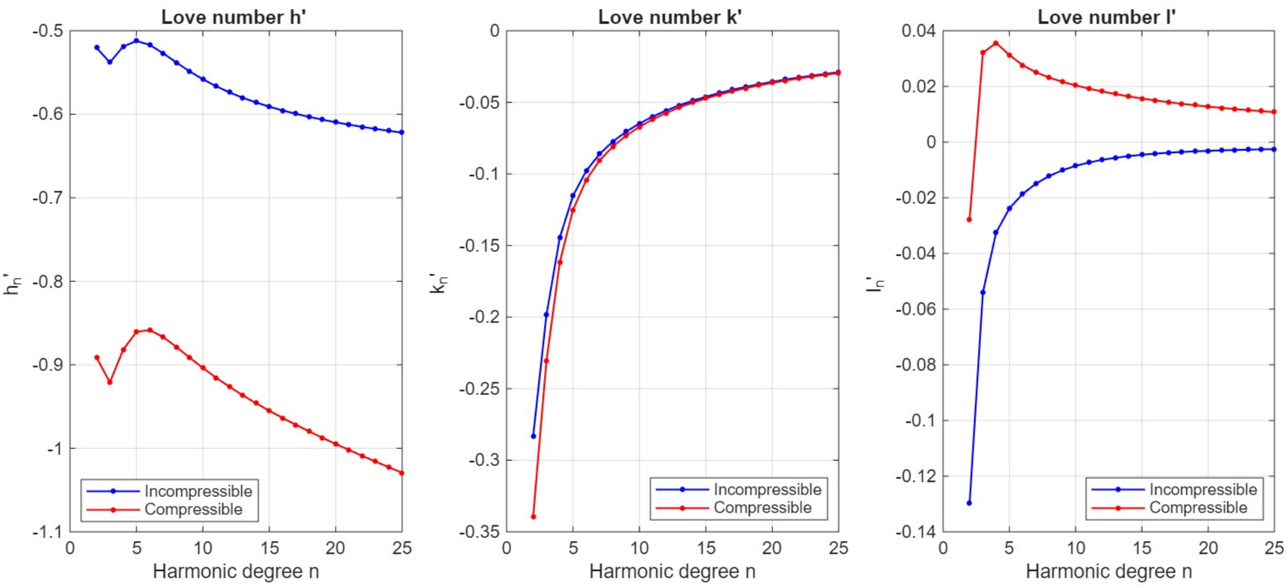

Figure 4.5: *Load Love numbers plots for E-FOC model up to degree $n = 25$ for both compressible and incompressible cases. The input data of the model are reported in Tab. 3.4.*

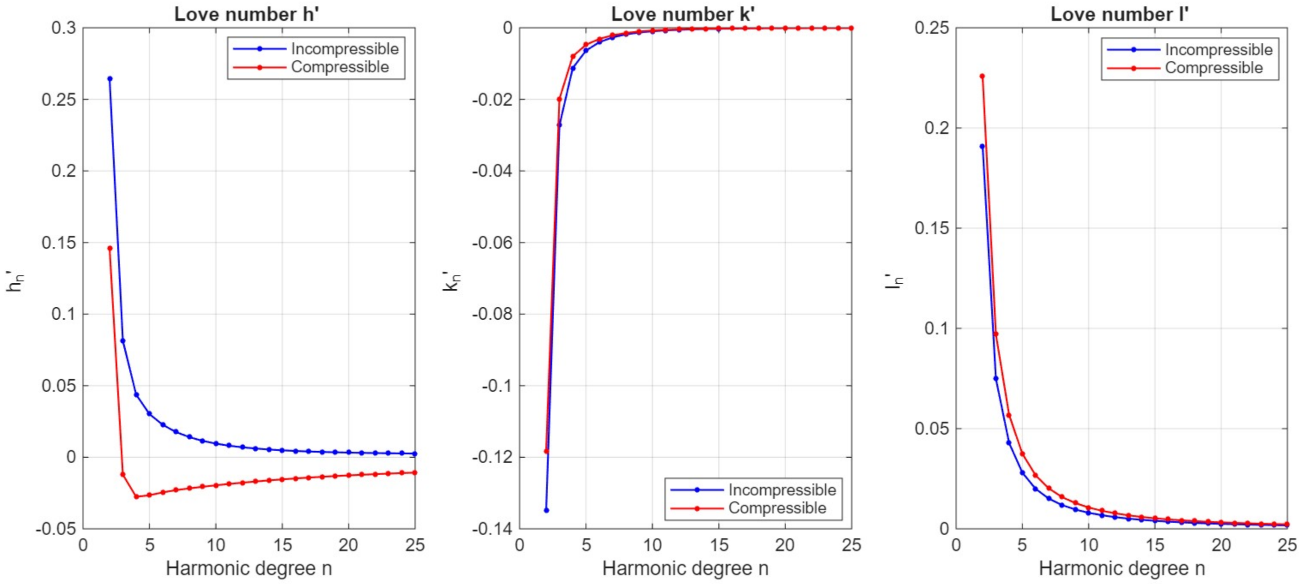

Figure 4.6: *Shear Love numbers plots for E-FOC model up to degree $n = 25$ for both compressible and incompressible cases. The input data of the model are reported in Tab. 3.4.*

TLN	n	Compressible	Incompressible
h_n	2	0.7046	0.6347
	3	0.3536	0.3162
	4	0.2198	0.2009
	5	0.1592	0.1488
k_n	2	0.3651	0.3513
	3	0.1228	0.1175
	4	0.0580	0.0562
	5	0.0341	0.0335
l_n	2	0.1182	0.1349
	3	0.0199	0.0273
	4	0.0080	0.0113
	5	0.0048	0.0064

Table 4.4: **TLNs results for E-FOC model**
Tidal Love numbers results for E-FOC model for both compressible and incompressible cases are reported up to the fifth harmonic degree.

LLN	n	Compressible	Incompressible
h'_n	2	-0.8914	-0.5205
	3	-0.9210	-0.5379
	4	-0.8820	-0.5189
	5	-0.8605	-0.5122
k'_n	2	-0.3395	-0.2834
	3	-0.2308	-0.1986
	4	-0.1619	-0.1447
	5	-0.1251	-0.1153
l'_n	2	-0.0278	-0.1296
	3	0.0321	-0.0540
	4	0.0356	-0.0325
	5	0.0313	-0.0238

Table 4.5: **LLNs results for E-FOC model**
Load Love numbers results for E-FOC model for both compressible and incompressible cases are reported up to the fifth harmonic degree.

SLN	n	Compressible	Incompressible
h''_n	2	0.1460	0.2645
	3	-0.0122	0.0813
	4	-0.0276	0.0438
	5	-0.0265	0.0302
k''_n	2	-0.1182	-0.1349
	3	-0.0199	-0.0273
	4	-0.0080	-0.0113
	5	-0.0048	-0.0064
l''_n	2	0.2257	0.1909
	3	0.0970	0.0750
	4	0.0568	0.0428
	5	0.0375	0.0280

Table 4.6: **SLNs results for E-FOC model**
Shear Love numbers results for E-FOC model for both compressible and incompressible cases are reported up to the fifth harmonic degree.

2 Results for super-Earths

2.1 SE2-FS model

The integration of *SE2-FS* model is carried out starting from right under the CMB and using an integration step of 10 km. The shear modulus of the mantle is tested in a range with three values per side and a spacing equal to half the central value. The results for the incompressible case are displayed in Figs. 4.7, 4.9 and 4.11, respectively for tidal, load and shear LNs. The results for the compressible case are displayed in Figs. 4.8, 4.10 and 4.12, respectively for tidal, load and shear LNs. The results corresponding to the average shear modulus of the mantle are reported in Tabs. 4.7, 4.8 and 4.9.

2.2 SE2-FOC model

The integration of *SE2-FOC* model is carried out starting from near the planetary center and using an integration step of 10 km. The shear modulus of the mantle is tested in a range with three values per side and a spacing equal to half the central value. The results for the incompressible case are displayed in Figs. 4.13, 4.15 and 4.17, respectively for tidal, load and shear LNs. The results for the compressible case are displayed in Figs. 4.14, 4.16 and 4.18, respectively for tidal, load and shear LNs. The results for the average shear modulus of the mantle are reported in Tabs. 4.10, 4.11 and 4.12.

2.3 SE4-FS model

The integration of *SE4-FS* model is carried out starting from right under the CMB and using integration step of 10 km. The shear modulus of the mantle is tested in a range with three values per side and a spacing equal to half the central value. The results for the incompressible case are displayed in Figs. 4.19, 4.21 and 4.23, respectively for tidal, load and shear LNs. The results for the compressible case are displayed in Figs. 4.20, 4.22 and 4.24, respectively for tidal, load and shear LNs. The results for the average shear modulus of the mantle are reported in Tabs. 4.13, 4.14 and 4.15.

2.4 SE8-FS model

The integration of *SE8-FS* model is carried out starting from right under the CMB and using an integration step of 10 km. The shear modulus of the mantle is tested in a range with three values per side and a spacing equal to half the central value. The results for the incompressible case are displayed in Figs. 4.25, 4.27 and 4.29, respectively for tidal, load and shear LNs. The results for the compressible case are displayed in Figs. 4.26, 4.28 and 4.30, respectively for tidal, load and shear LNs. The results for the average shear modulus of the mantle are reported in Tabs. 4.16, 4.17 and 4.18.

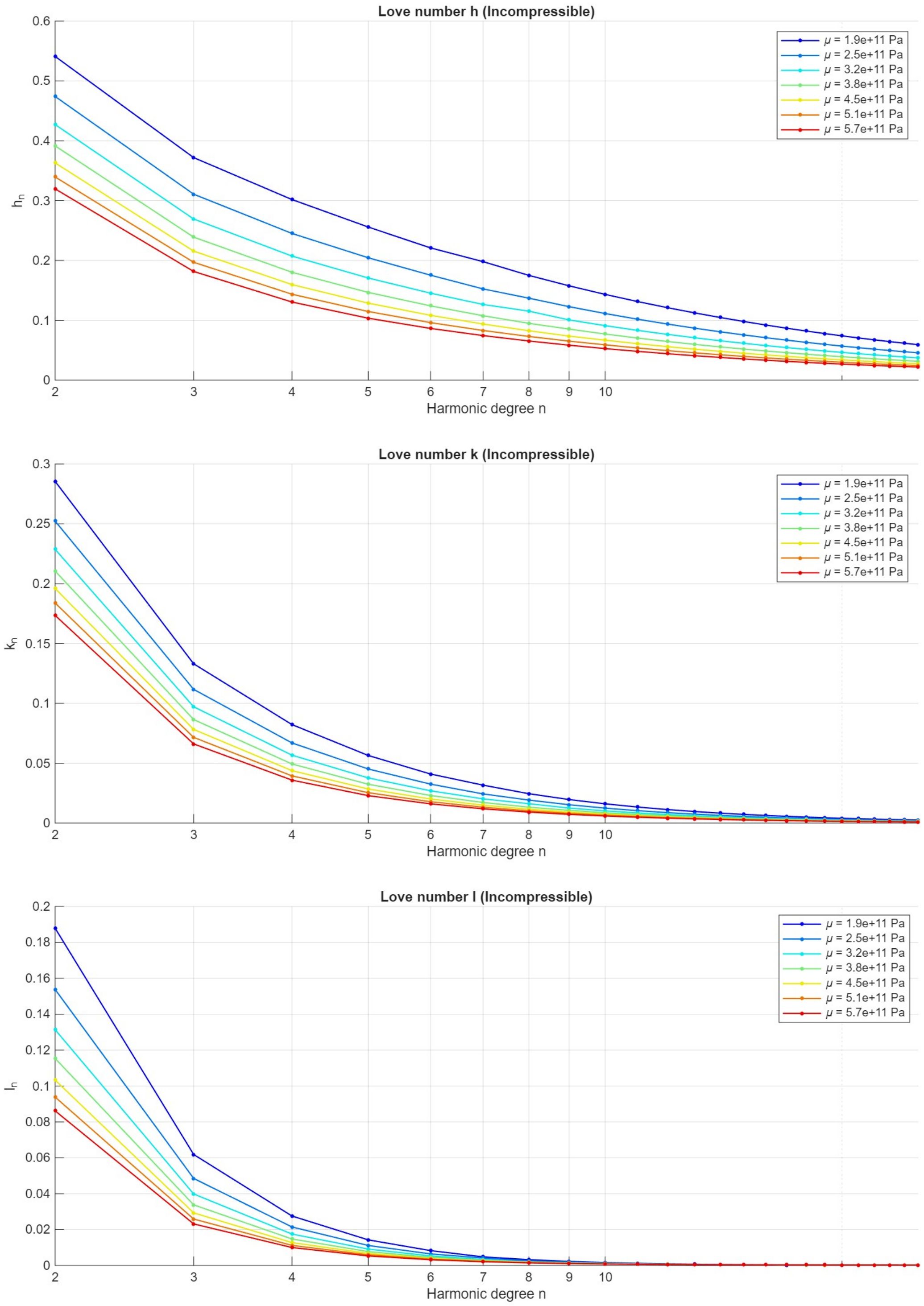

Figure 4.7: *Tidal Love numbers plots for SE2-FS model up to degree $n = 25$ for the incompressible case. The input data of the model are reported in Tab. 3.8.*

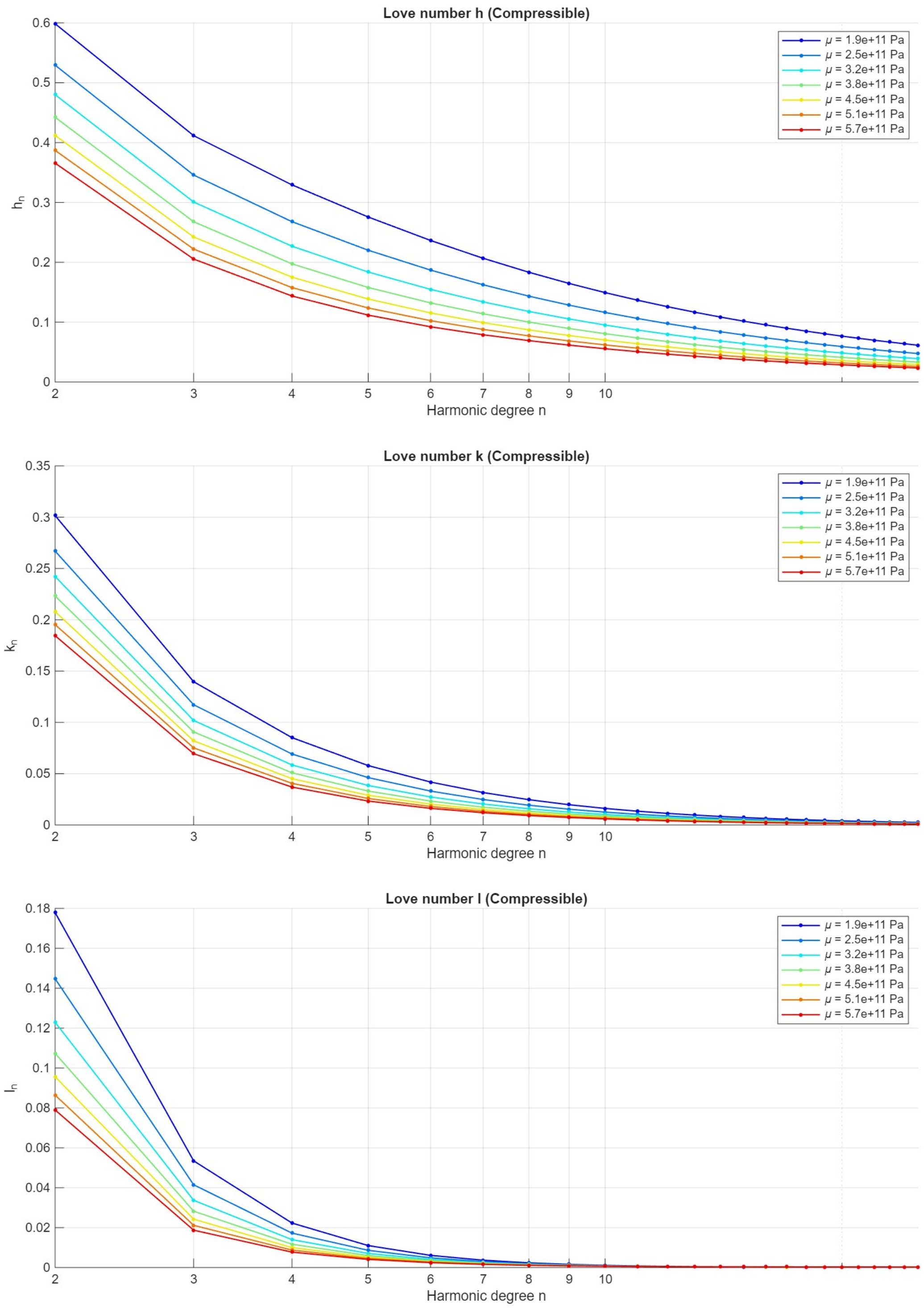

Figure 4.8: *Tidal Love numbers plots for SE2-FS model up to degree $n = 25$ for the compressible case. The input data of the model are reported in Tab. 3.8.*

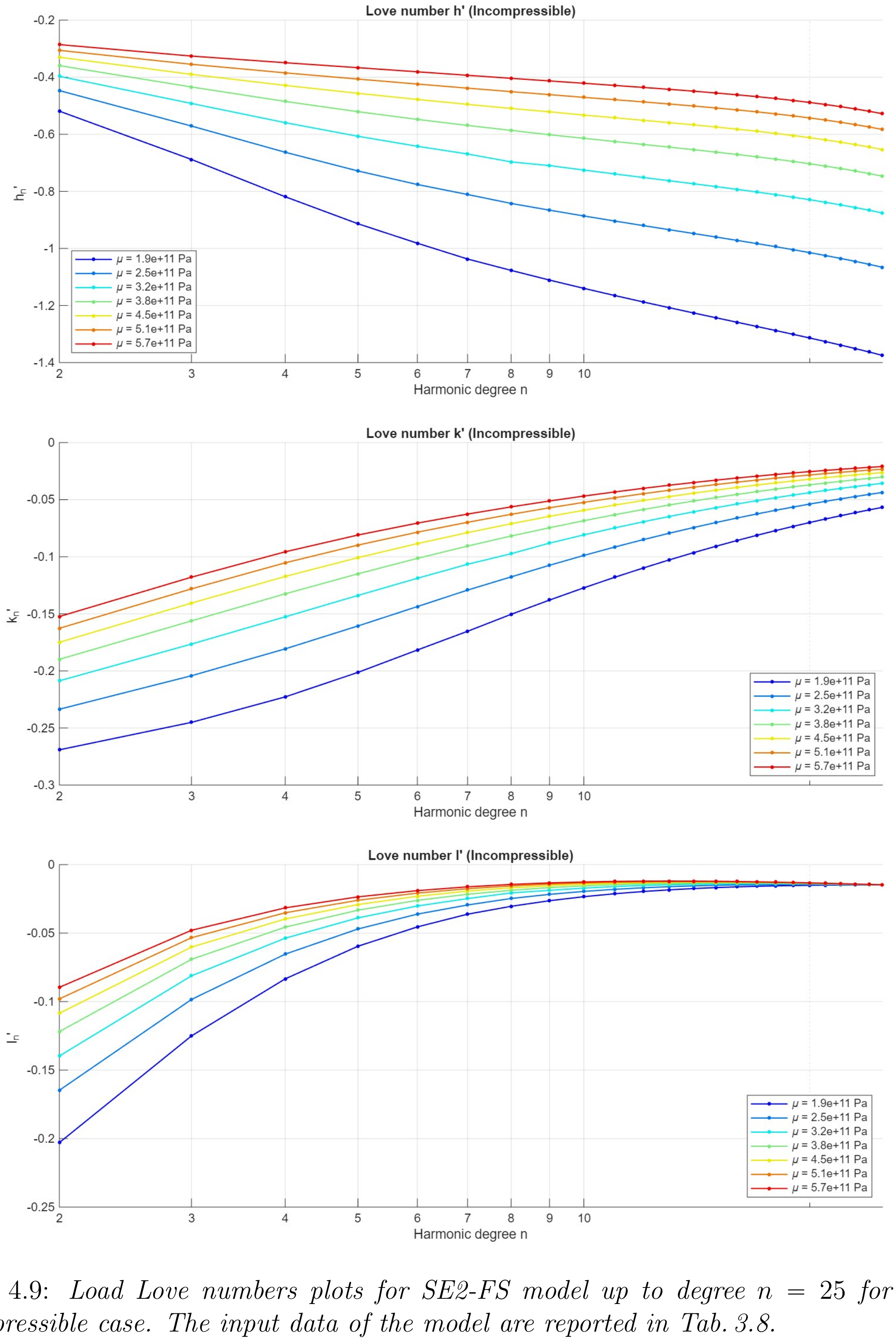

Figure 4.9: *Load Love numbers plots for SE2-FS model up to degree $n = 25$ for the incompressible case. The input data of the model are reported in Tab. 3.8.*

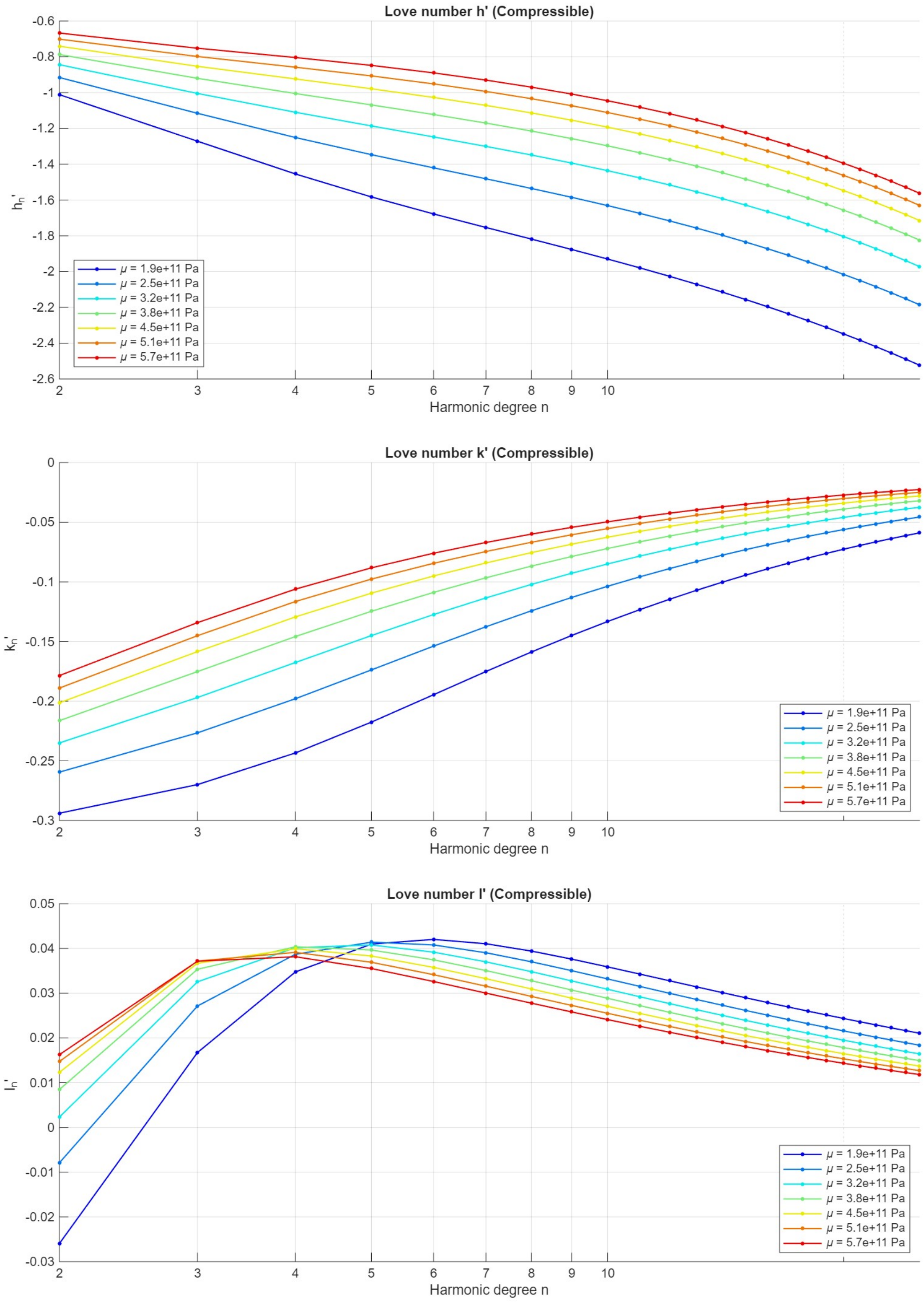

Figure 4.10: *Load Love numbers plots for SE2-FS model up to degree $n = 25$ for the compressible case. The input data of the model are reported in Tab. 3.8.*

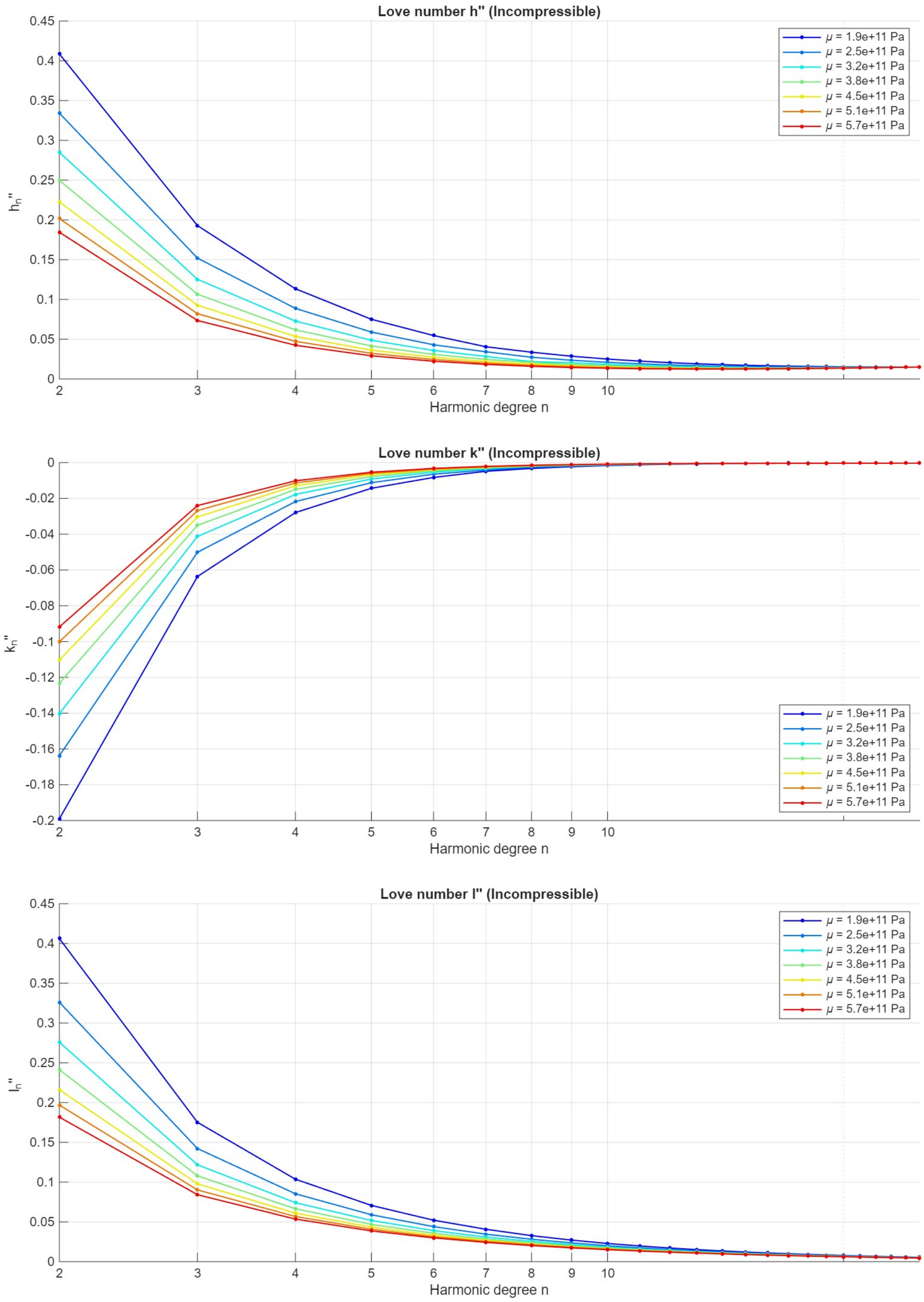

Figure 4.11: *Shear Love numbers plots for SE2-FS model up to degree $n = 25$ for the incompressible case. The input data of the model are reported in Tab. 3.8.*

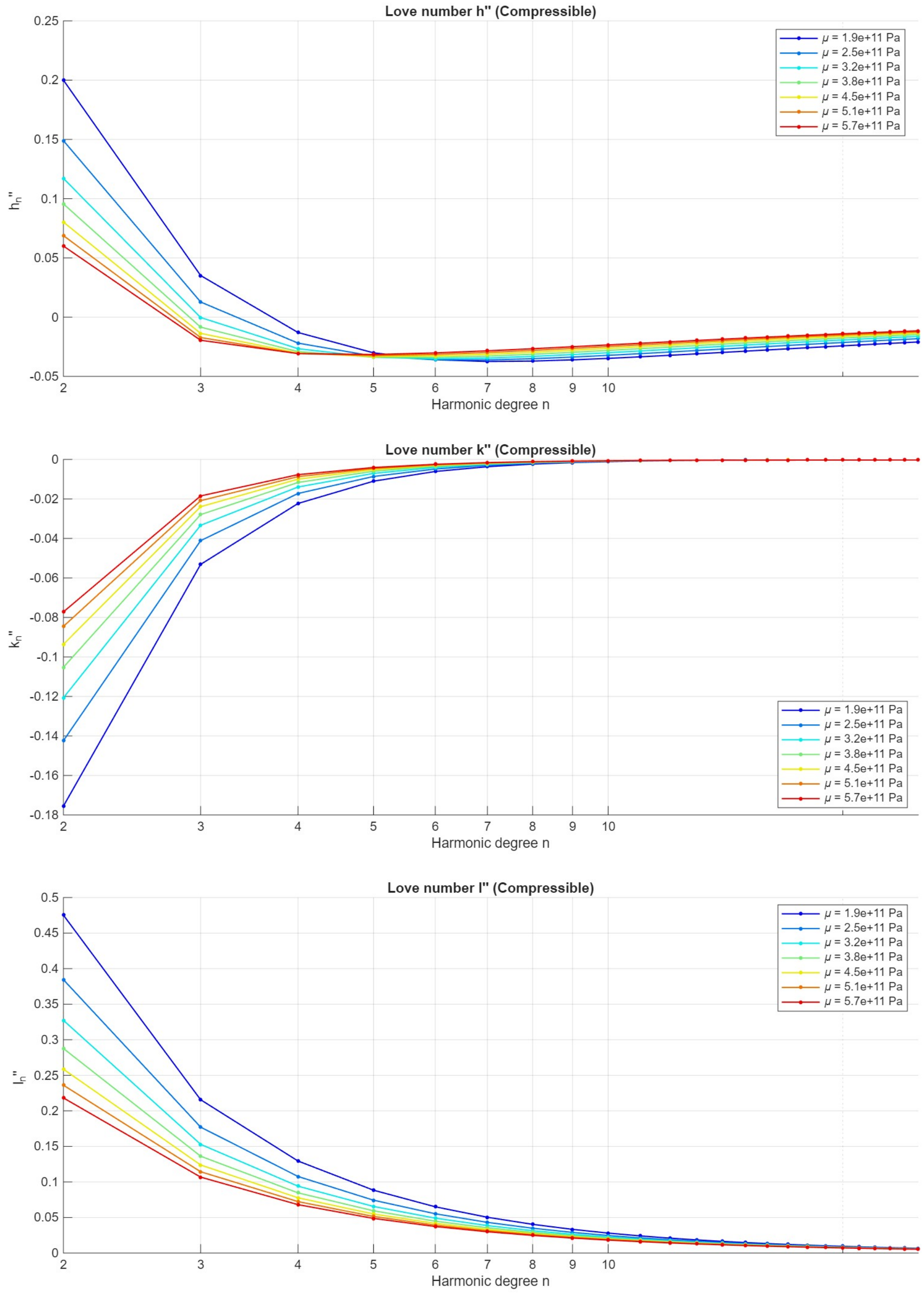

Figure 4.12: *Shear Love numbers plots for SE2-FS model up to degree $n = 25$ for the compressible case. The input data of the model are reported in Tab. 3.8.*

TLN	n	Compressible	Incompressible
h_n	2	0.4424	0.3915
	3	0.2677	0.2390
	4	0.1974	0.1802
	5	0.1579	0.1467
k_n	2	0.2233	0.2106
	3	0.0907	0.0865
	4	0.0509	0.0494
	5	0.0330	0.0324
l_n	2	0.1074	0.1154
	3	0.0282	0.0338
	4	0.0117	0.0148
	5	0.0060	0.0078

Table 4.7: **TLNs results for SE2-FS model**
Tidal Love numbers results for SE2-FS model for both compressible and incompressible cases corresponding to the average shear modulus of the mantle are reported up to the fifth harmonic degree.

LLN	n	Compressible	Incompressible
h'_n	2	-0.7871	-0.3594
	3	-0.9201	-0.4343
	4	-1.0051	-0.4849
	5	-1.0688	-0.5208
k'_n	2	-0.2163	-0.1899
	3	-0.1752	-0.1562
	4	-0.1458	-0.1325
	5	-0.1246	-0.1150
l'_n	2	0.0085	-0.1219
	3	0.0353	-0.0691
	4	0.0404	-0.0456
	5	0.0396	-0.0333

Table 4.8: **LLNs results for SE2-FS model**
Load Love numbers results for SE2-FS model for both compressible and incompressible cases corresponding to the average shear modulus of the mantle are reported up to the fifth harmonic degree.

SLN	n	Compressible	Incompressible
h''_n	2	0.0956	0.2496
	3	-0.0084	0.1066
	4	-0.0291	0.0617
	5	-0.0338	0.0415
k''_n	2	-0.1052	-0.1233
	3	-0.0279	-0.0350
	4	-0.0117	-0.0150
	5	-0.0060	-0.0078
l''_n	2	0.2878	0.2413
	3	0.1362	0.1079
	4	0.0847	0.0665
	5	0.0594	0.0469

Table 4.9: **SLNs results for SE2-FS model**
Shear Love numbers results for SE2-FS model for both compressible and incompressible cases corresponding to the average shear modulus of the mantle are reported up to the fifth harmonic degree.

TLN	n	Compressible	Incompressible
h_n	2	0.5618	0.4892
	3	0.3391	0.2986
	4	0.2252	0.2035
	5	0.1675	0.1546
k_n	2	0.1967	0.1864
	3	0.0940	0.0907
	4	0.0525	0.0512
	5	0.0334	0.0329
l_n	2	0.0977	0.1198
	3	0.0196	0.0291
	4	0.0080	0.0121
	5	0.0047	0.0067

Table 4.10: **TLNs results for SE2-FOC model**
Tidal Love numbers results for SE2-FOC model for both compressible and incompressible cases corresponding to the average shear modulus of the mantle are reported up to the fifth harmonic degree.

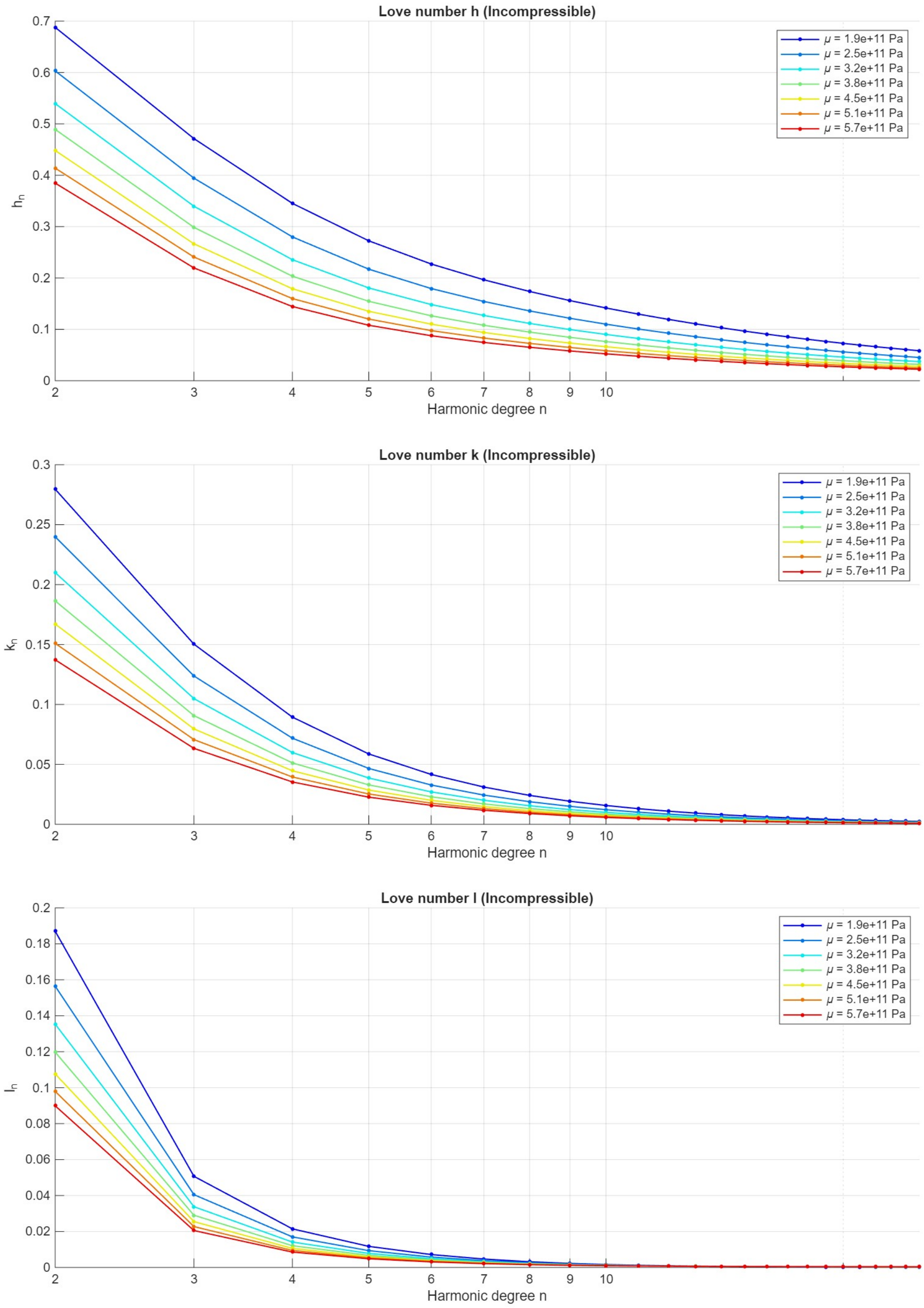

Figure 4.13: *Tidal Love numbers plots for SE2-FOC model up to degree $n = 25$ for the incompressible case. The input data of the model are reported in Tab. 3.9.*

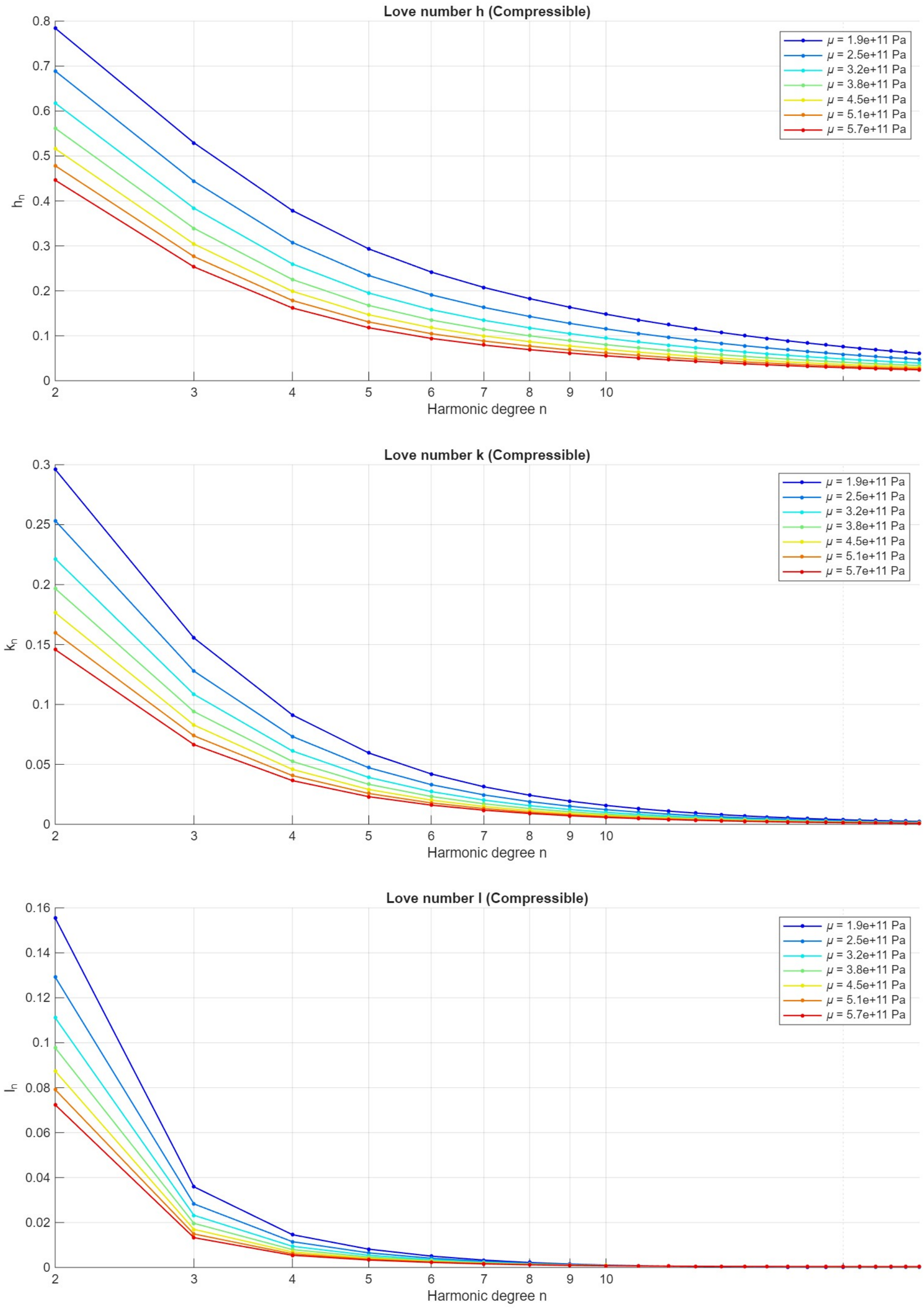

Figure 4.14: *Tidal Love numbers plots for SE2-FOC model up to degree $n = 25$ for the compressible case. The input data of the model are reported in Tab. 3.9.*

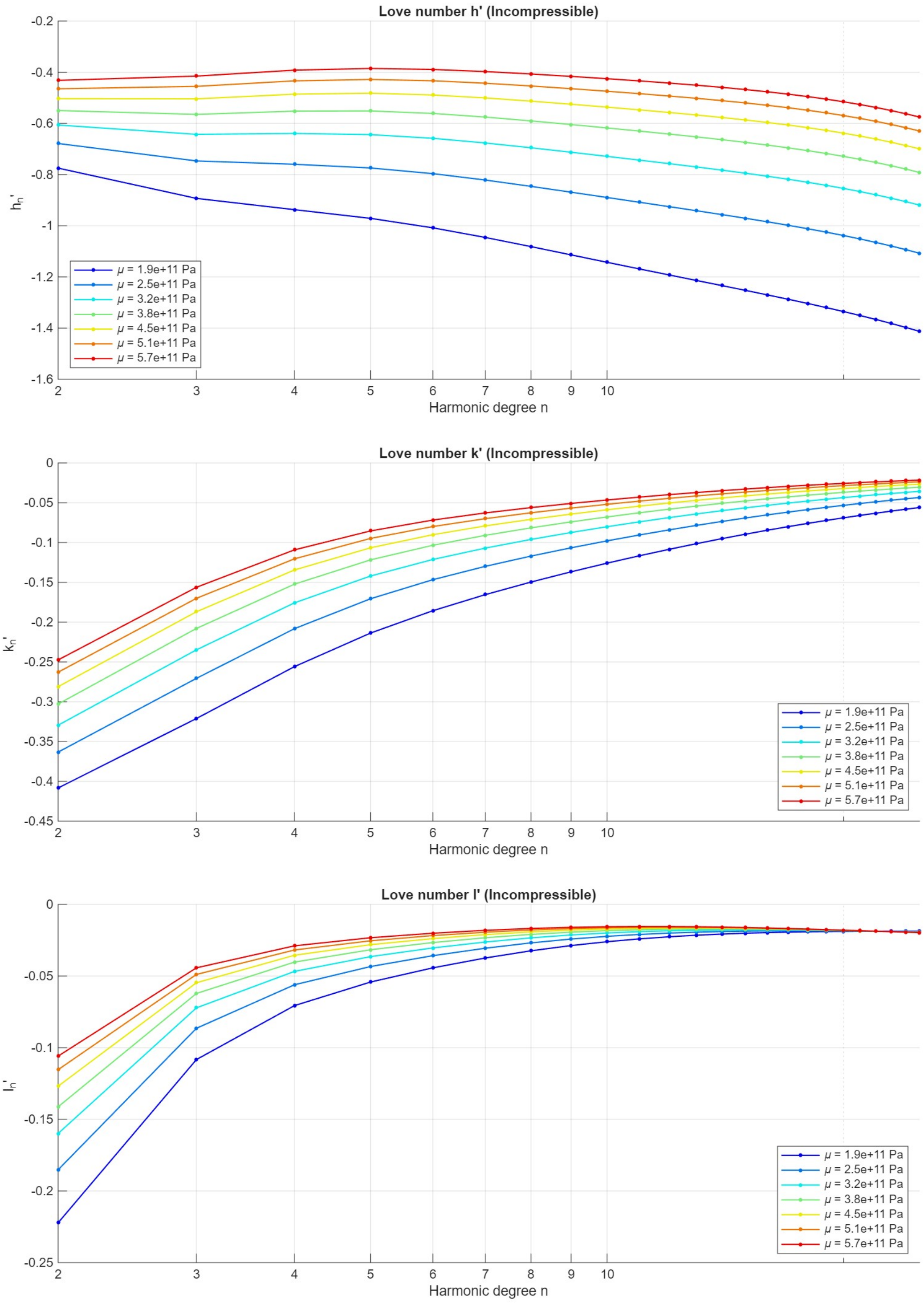

Figure 4.15: *Load Love numbers plots for SE2-FOC model up to degree $n = 25$ for the incompressible case. The input data of the model are reported in Tab. 3.9.*

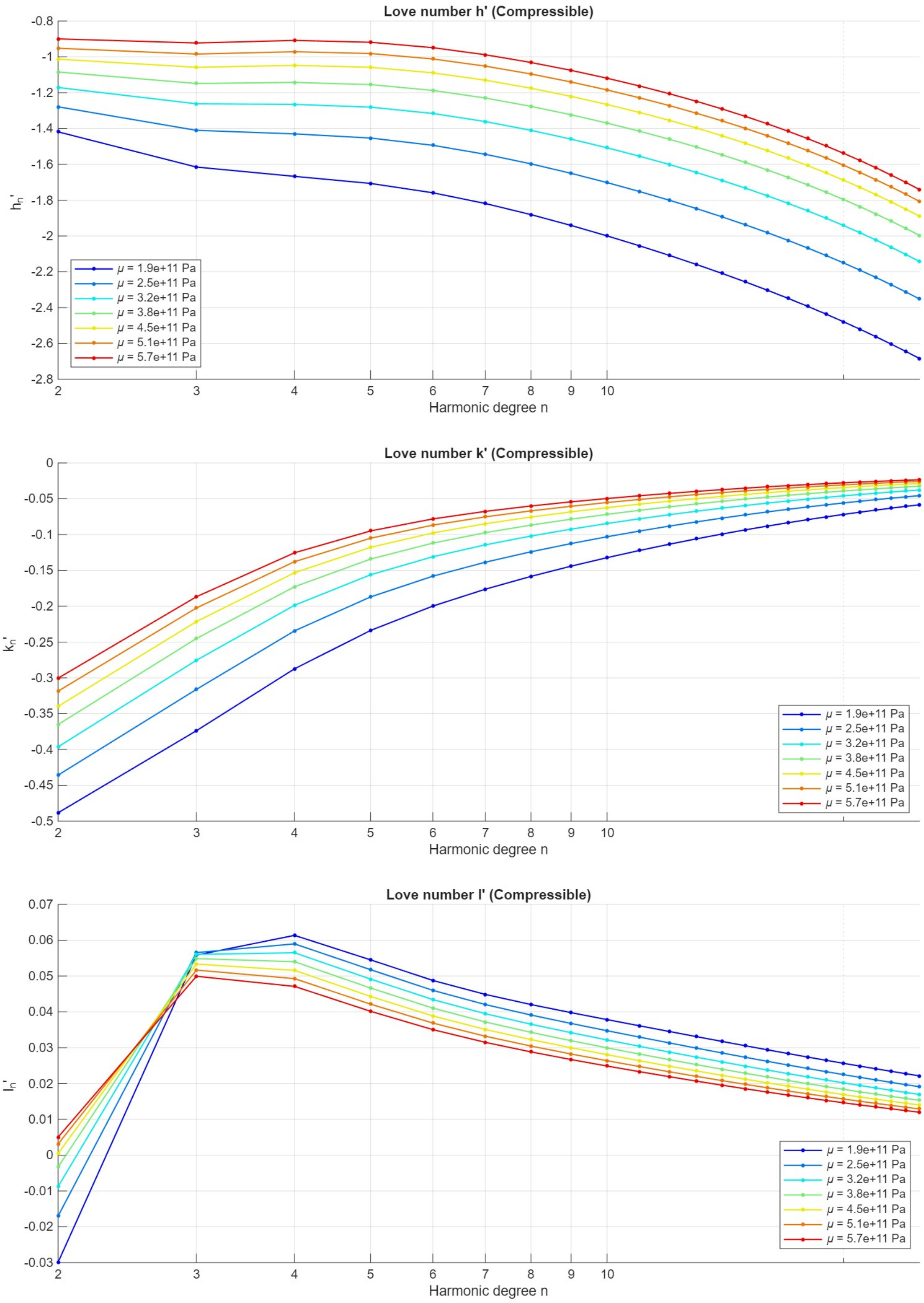

Figure 4.16: *Load Love numbers plots for SE2-FOC model up to degree $n = 25$ for the compressible case. The input data of the model are reported in Tab. 3.9.*

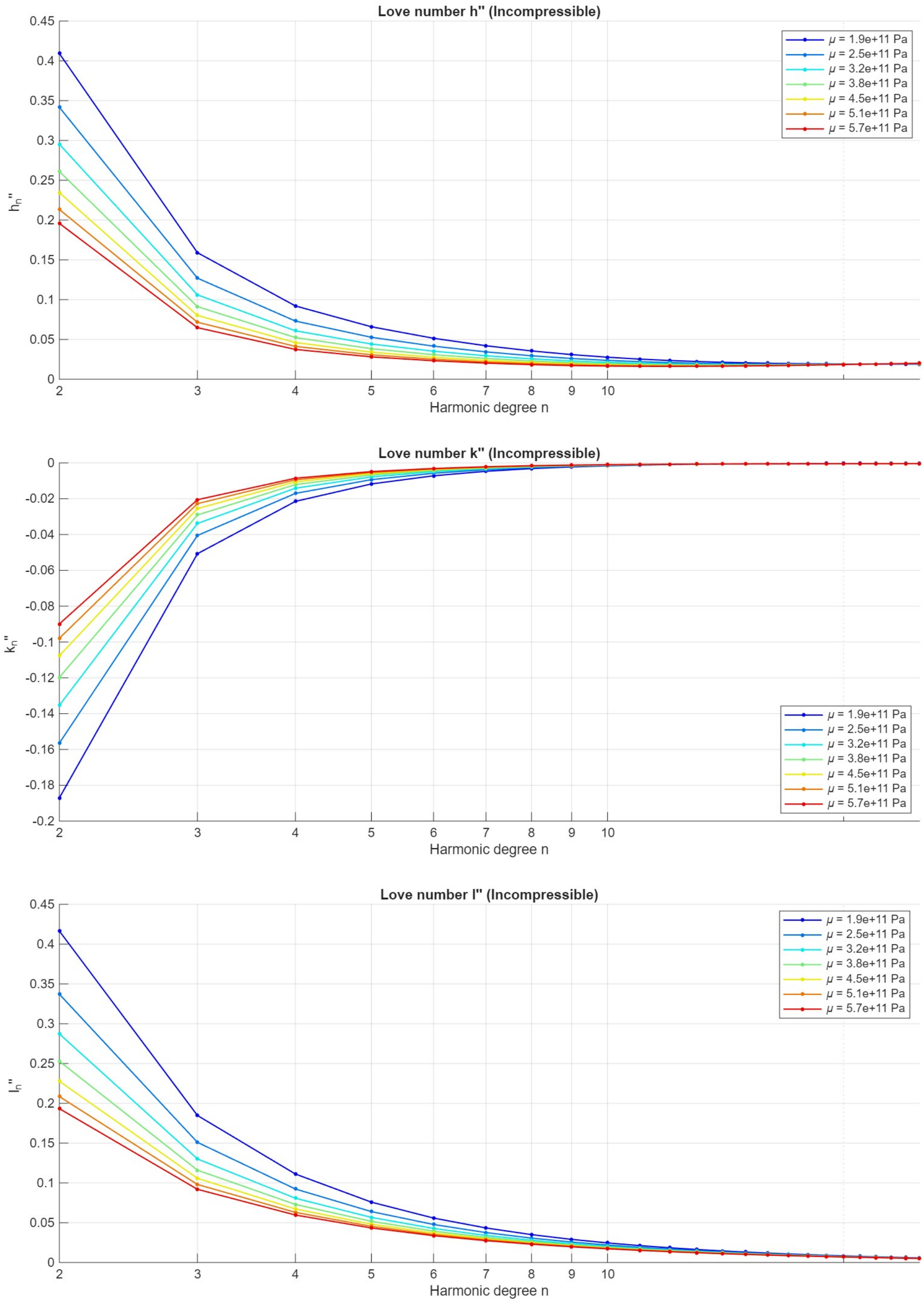

Figure 4.17: *Shear Love numbers plots for SE2-FOC model up to degree $n = 25$ for the incompressible case. The input data of the model are reported in Tab. 3.9.*

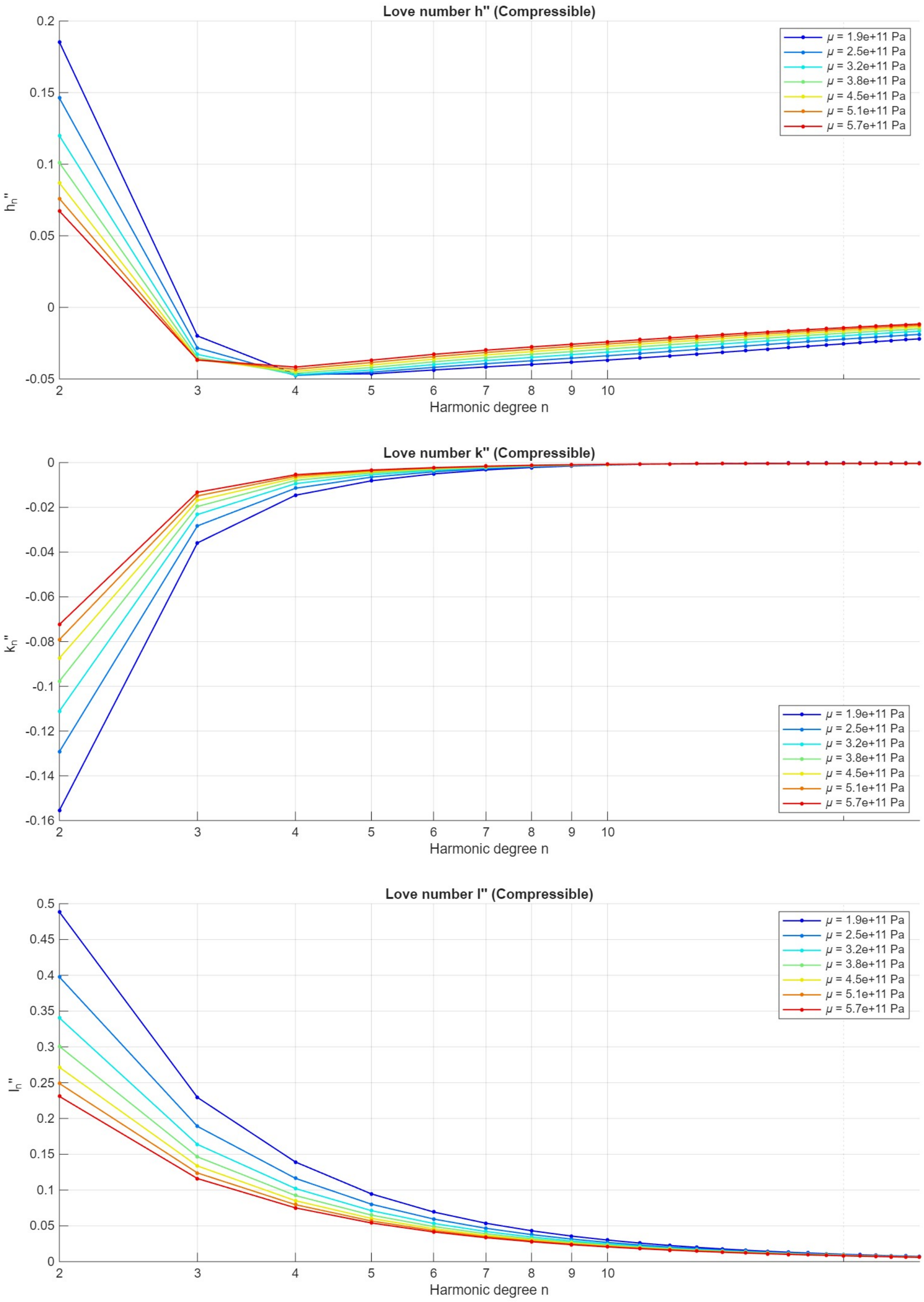

Figure 4.18: *Shear Love numbers plots for SE2-FOC model up to degree $n = 25$ for the compressible case. The input data of the model are reported in Tab. 3.9.*

LLN	n	**Compressible**	**Incompressible**
h'_n	2	-1.0844	-0.5497
	3	-1.1485	-0.5649
	4	-1.1427	-0.5520
	5	-1.1548	-0.5512
k'_n	2	-0.3651	-0.3028
	3	-0.2451	-0.2079
	4	-0.1728	-0.1522
	5	-0.1341	-0.1217
l'_n	2	-0.0033	-0.1413
	3	0.0549	-0.0622
	4	0.0540	-0.0403
	5	0.0466	-0.0316

Table 4.11: **LLNs results for SE2-FOC model**
Load Love numbers results for SE2-FOC model for both compressible and incompressible cases corresponding to the average shear modulus of the mantle are reported up to the fifth harmonic degree.

SLN	n	**Compressible**	**Incompressible**
h''_n	2	0.1010	0.2610
	3	-0.0352	0.0912
	4	-0.0460	0.0524
	5	-0.0420	0.0384
k''_n	2	-0.0977	-0.1198
	3	-0.0196	-0.0291
	4	-0.0080	-0.0121
	5	-0.0047	-0.0067
l''_n	2	0.3008	0.2529
	3	0.1464	0.1160
	4	0.0924	0.0729
	5	0.0650	0.0517

Table 4.12: **SLNs results for SE2-FOC model**
Shear Love numbers results for SE2-FOC model for both compressible and incompressible cases corresponding to the average shear modulus of the mantle are reported up to the fifth harmonic degree.

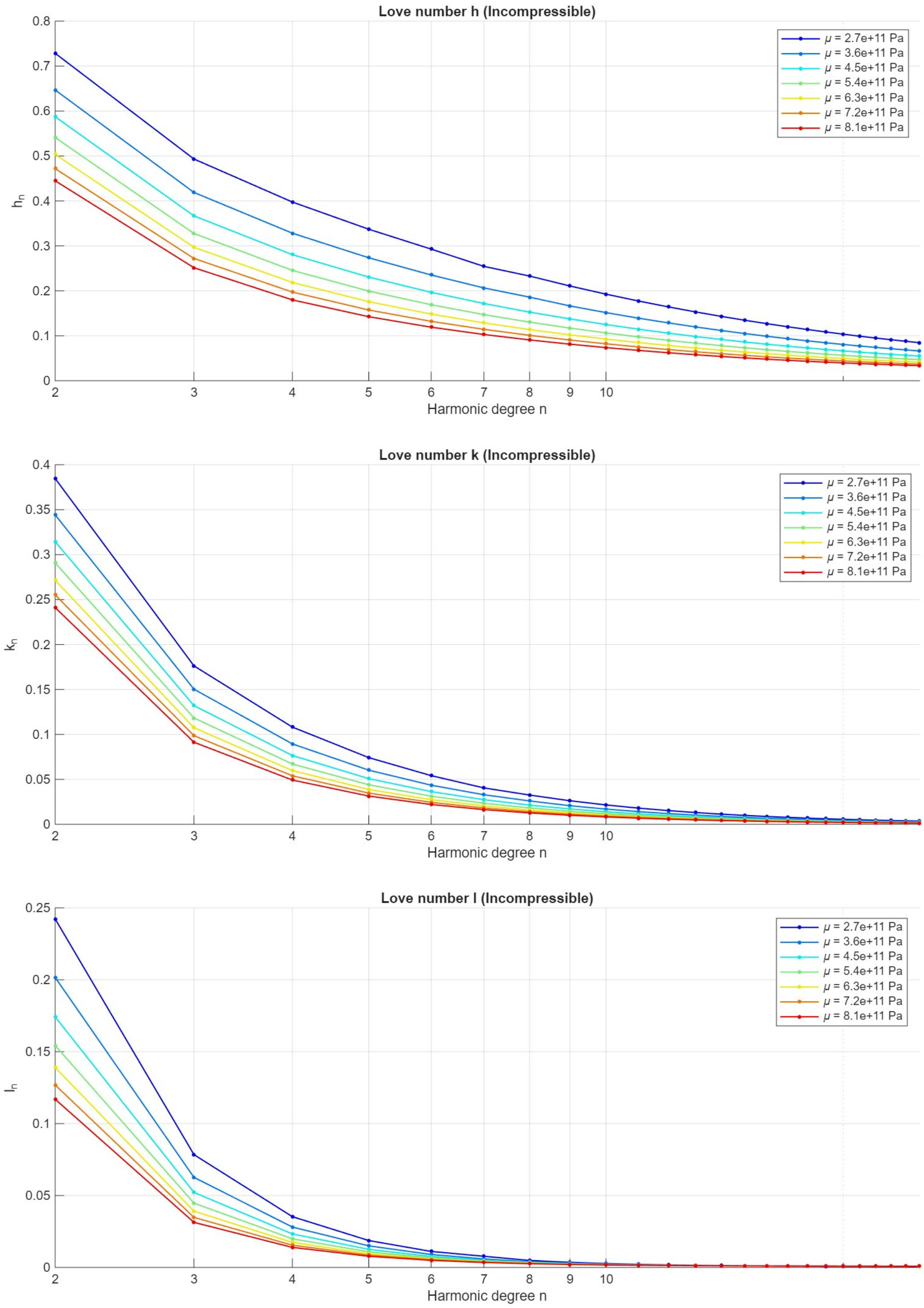

Figure 4.19: *Tidal Love numbers plots for SE4-FS model up to degree $n = 25$ for the incompressible case. The input data of the model are reported in Tab. 3.10.*

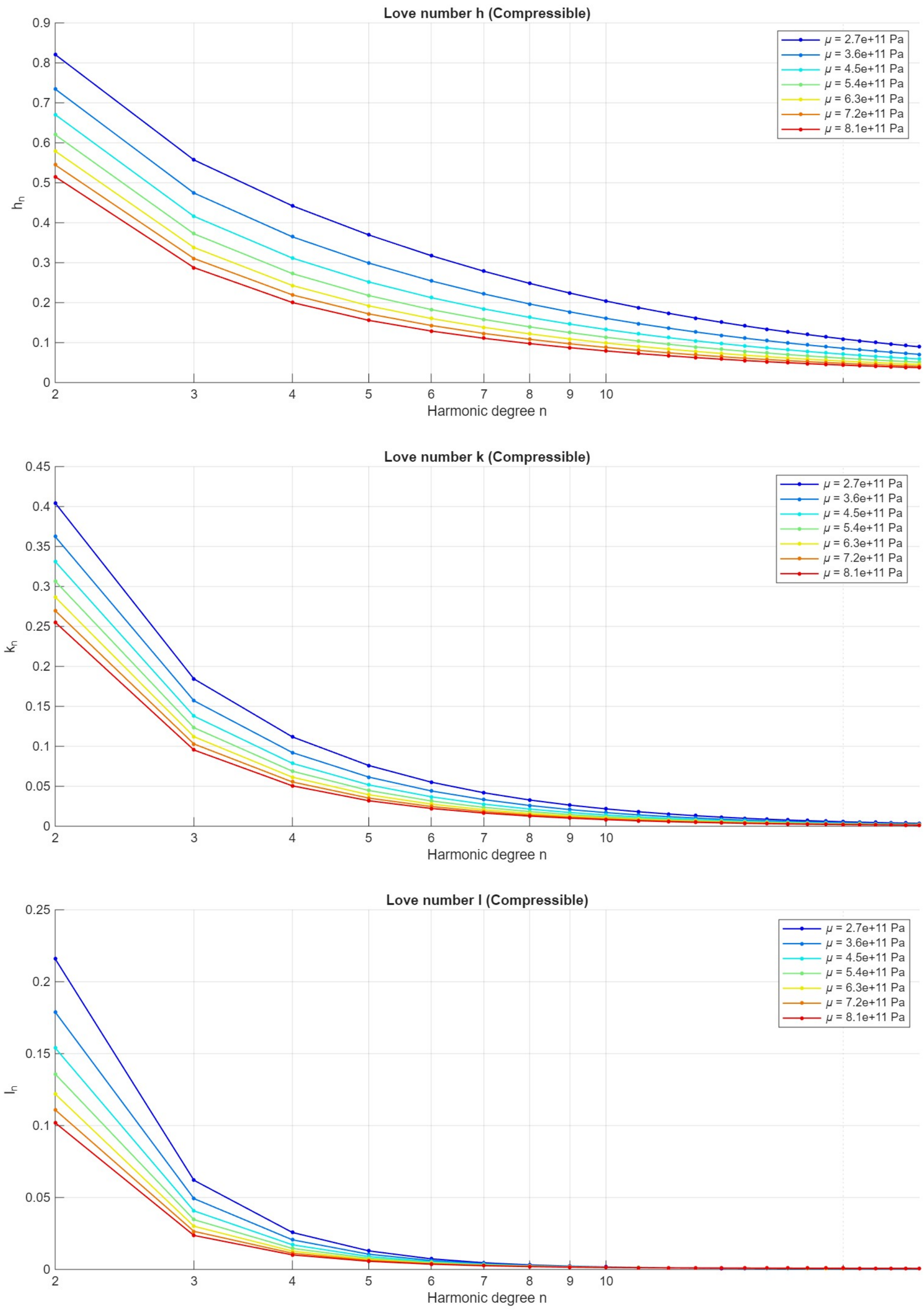

Figure 4.20: *Tidal Love numbers plots for SE4-FS model up to degree* $n = 25$ *for the compressible case. The input data of the model are reported in Tab. 3.10.*

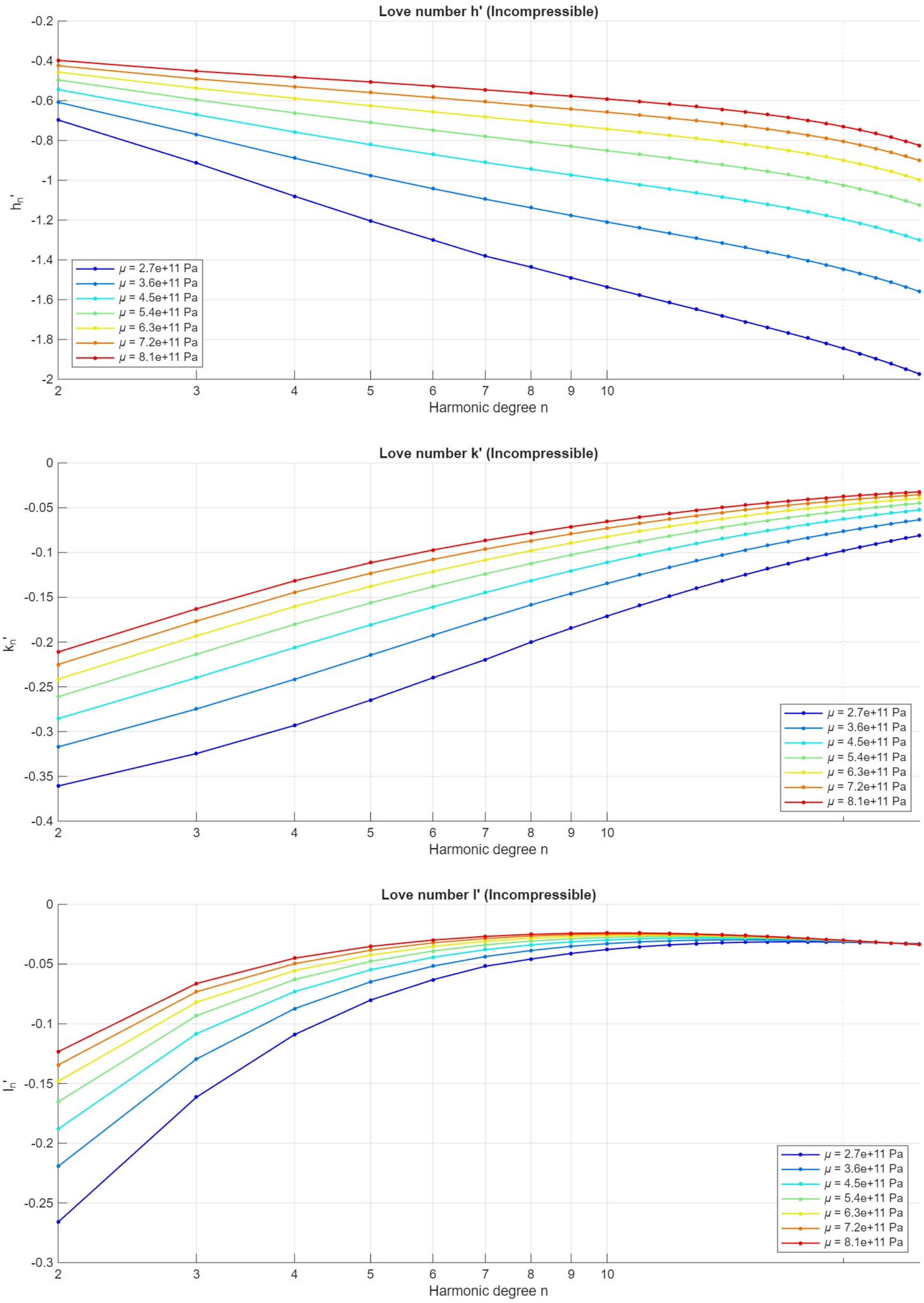

Figure 4.21: *Load Love numbers plots for SE4-FS model up to degree $n = 25$ for the incompressible case. The input data of the model are reported in Tab. 3.10.*

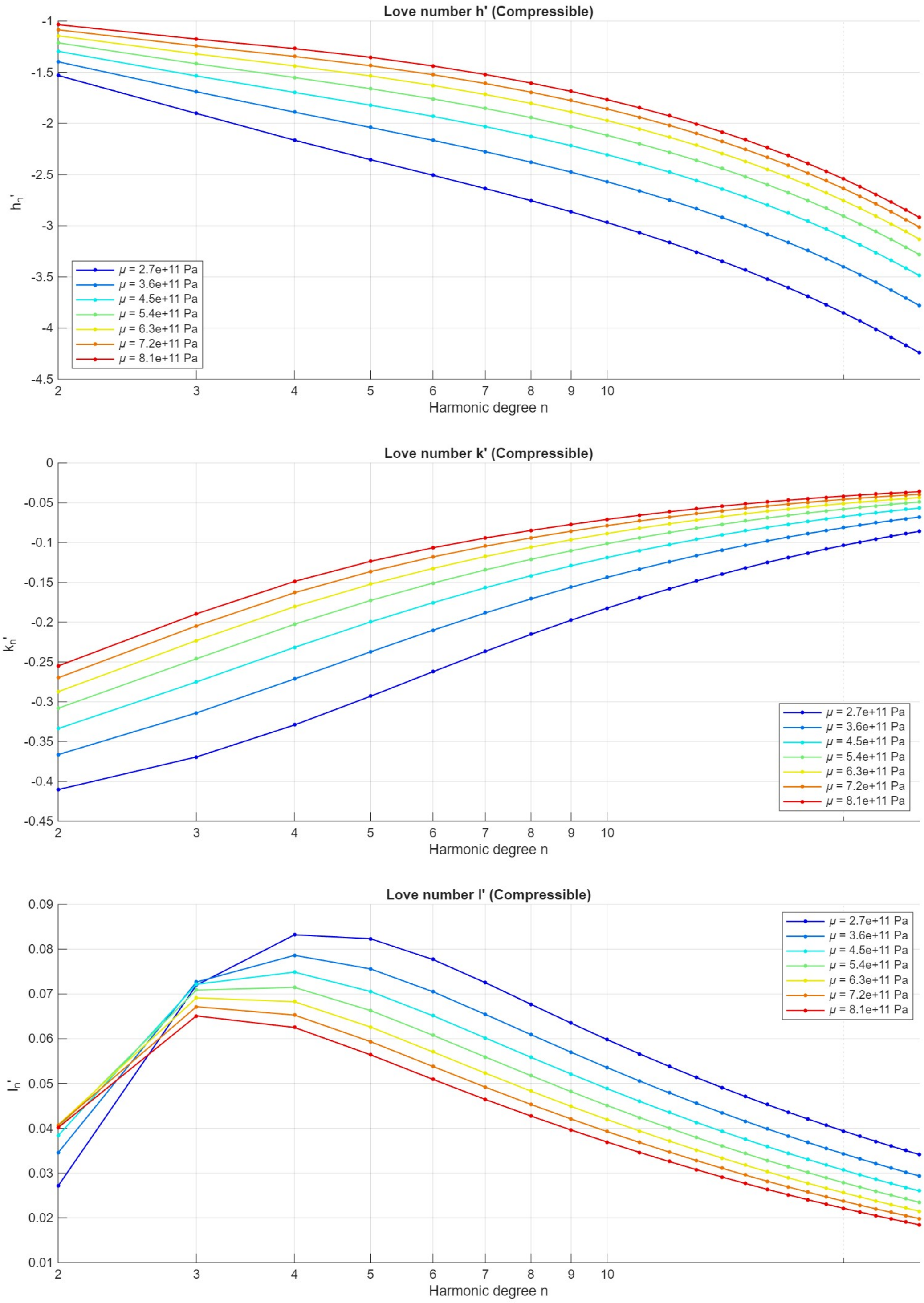

Figure 4.22: *Load Love numbers plots for SE4-FS model up to degree $n = 25$ for the compressible case. The input data of the model are reported in Tab. 3.10.*

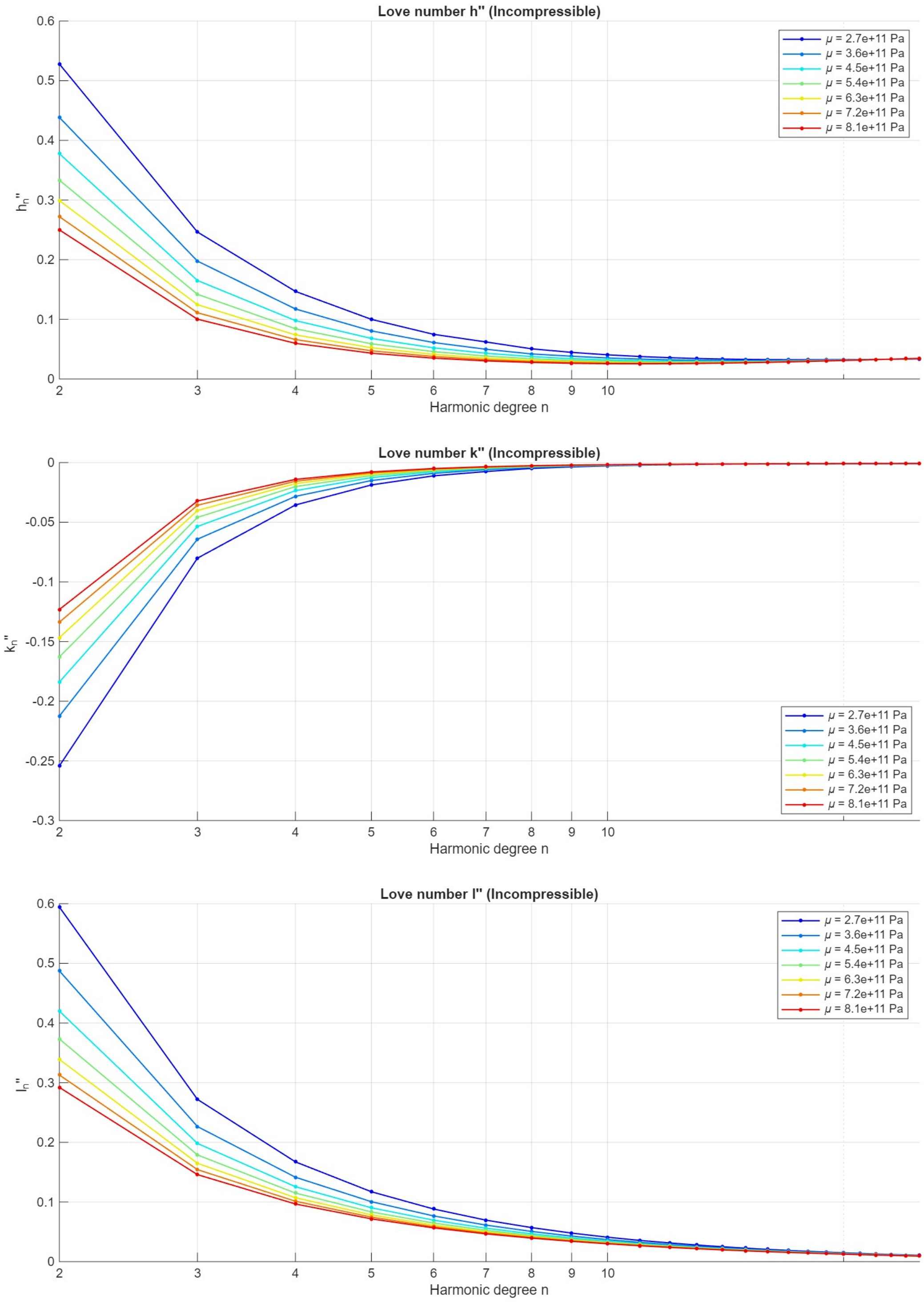

Figure 4.23: *Shear Love numbers plots for SE4-FS model up to degree $n = 25$ for the incompressible case. The input data of the model are reported in Tab. 3.10.*

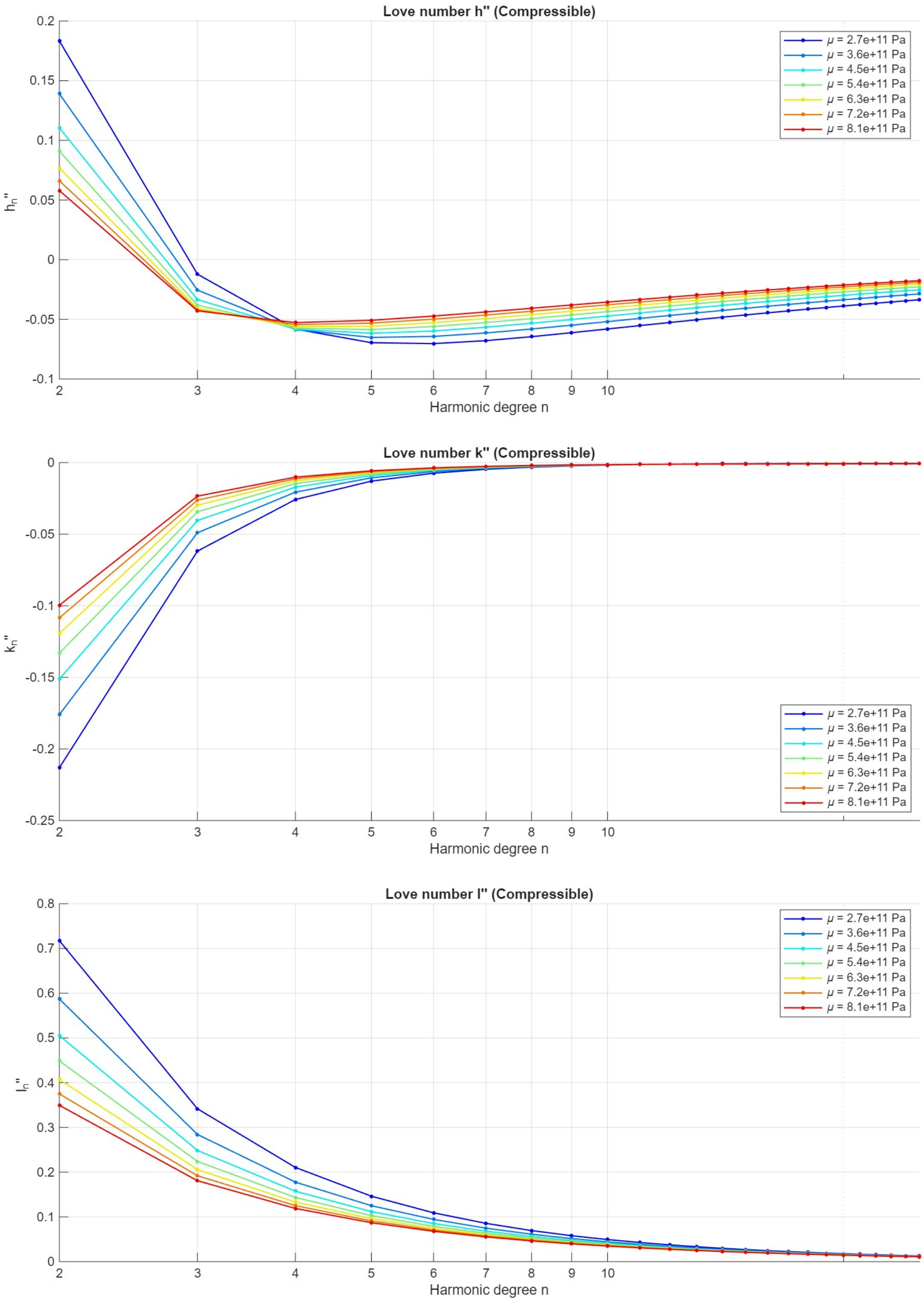

Figure 4.24: *Shear Love numbers plots for SE4-FS model up to degree* $n = 25$ *for the compressible case. The input data of the model are reported in Tab. 3.10.*

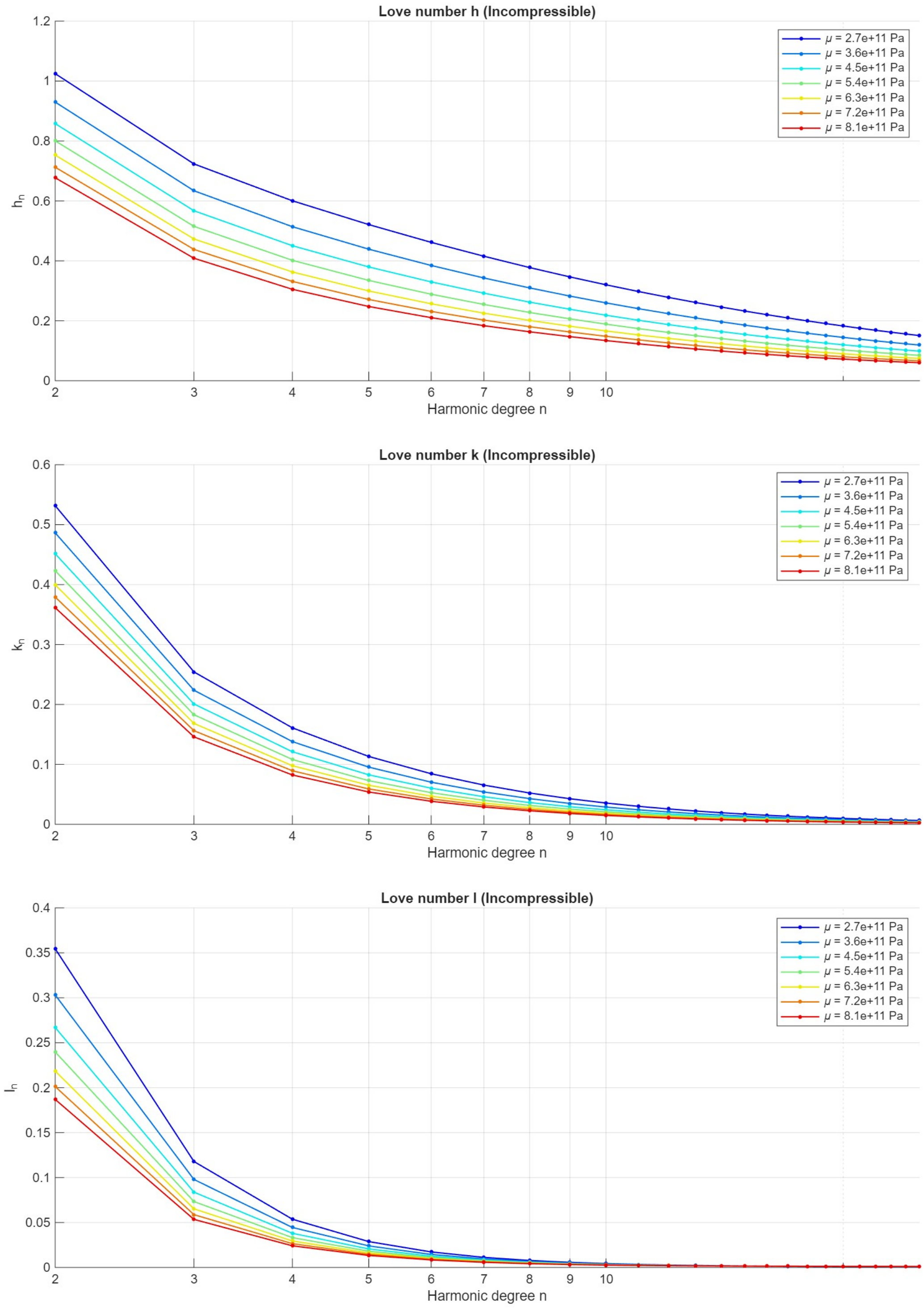

Figure 4.25: *Tidal Love numbers plots for SE8-FS model up to degree $n = 25$ for the incompressible case. The input data of the model are reported in Tab. 3.11.*

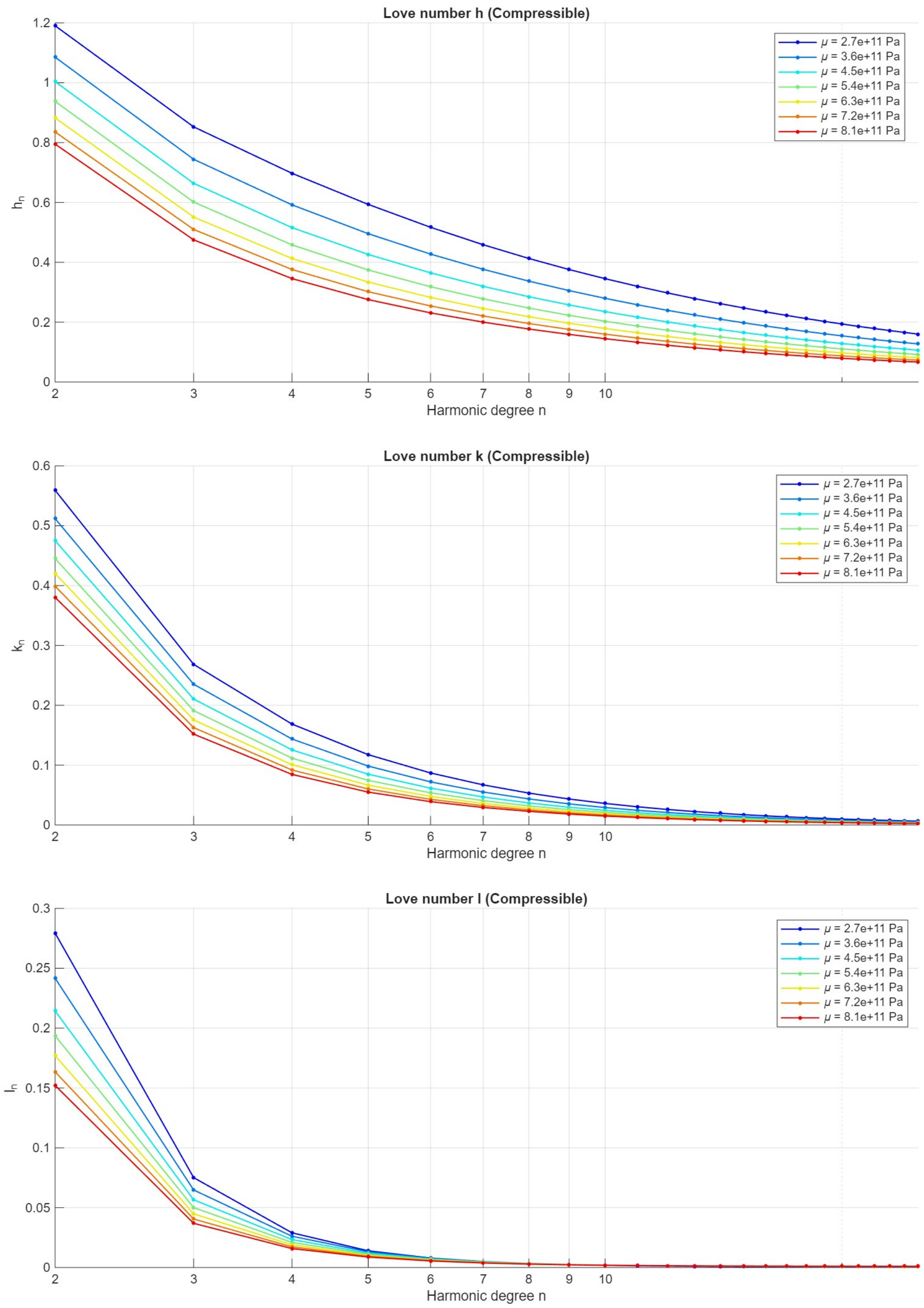

Figure 4.26: *Tidal Love numbers plots for SE8-FS model up to degree $n = 25$ for the compressible case. The input data of the model are reported in Tab. 3.11.*

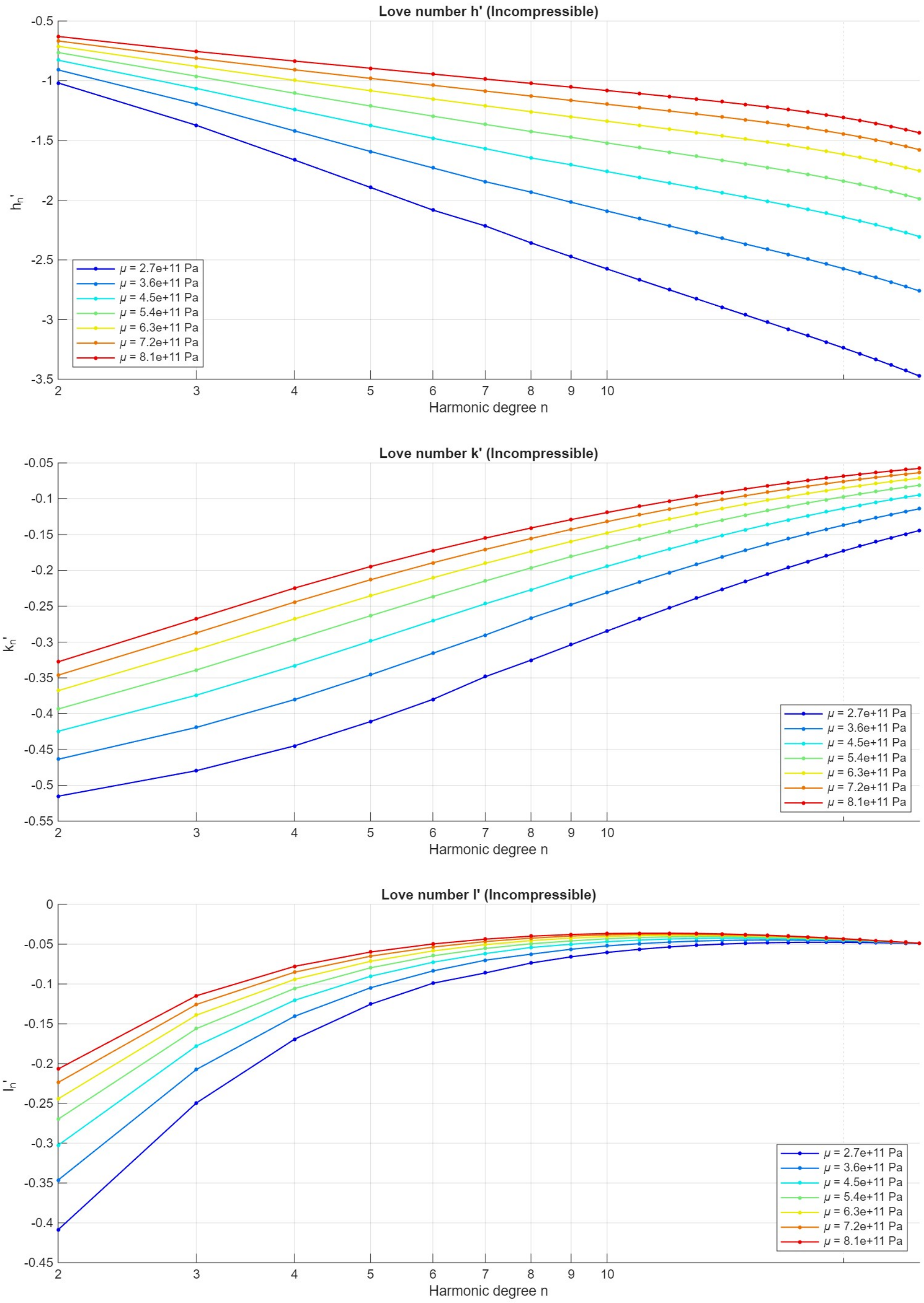

Figure 4.27: *Load Love numbers plots for SE8-FS model up to degree $n = 25$ for the incompressible case. The input data of the model are reported in Tab. 3.11.*

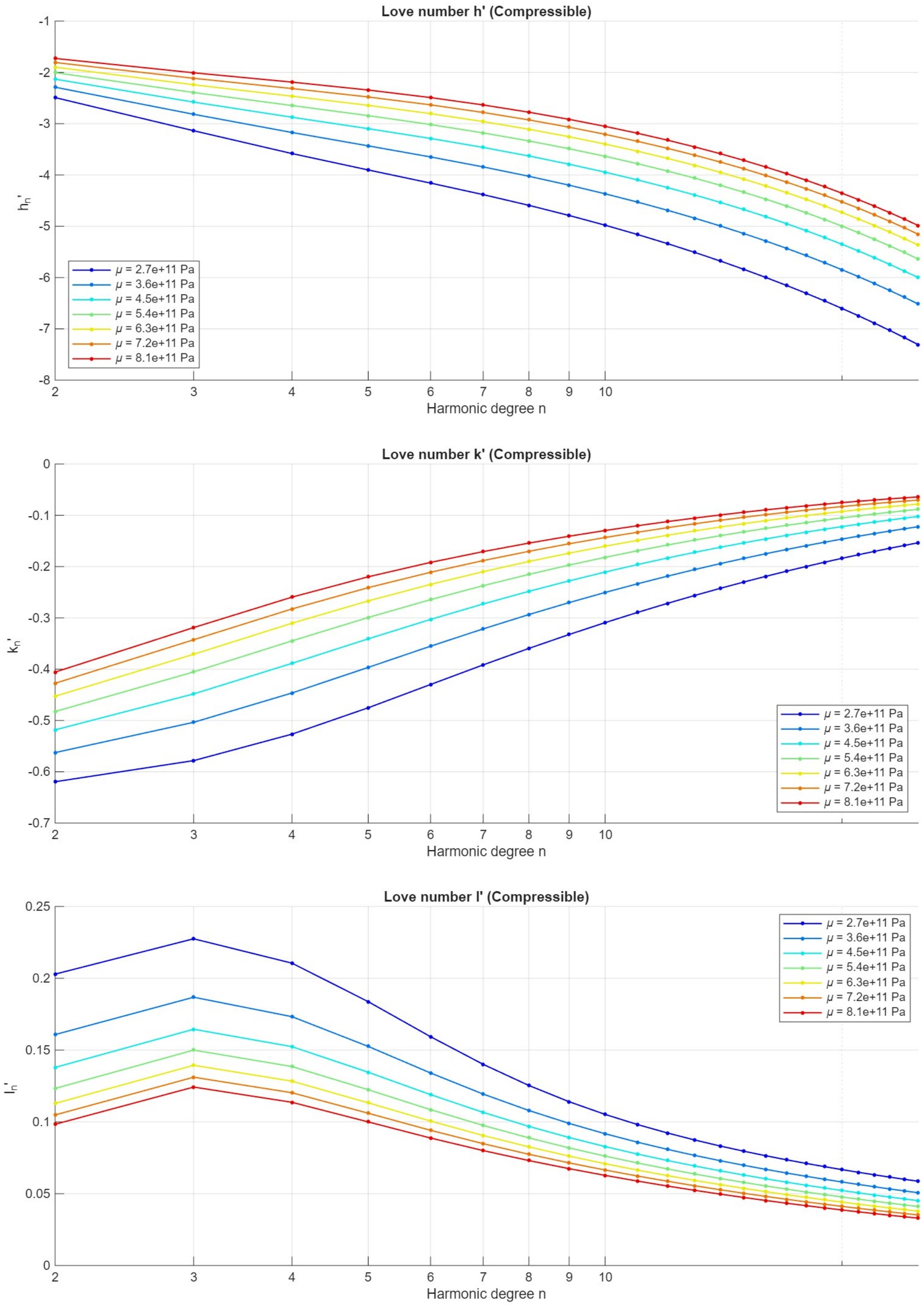

Figure 4.28: *Load Love numbers plots for SE8-FS model up to degree $n = 25$ for the compressible case. The input data of the model are reported in Tab. 3.11.*

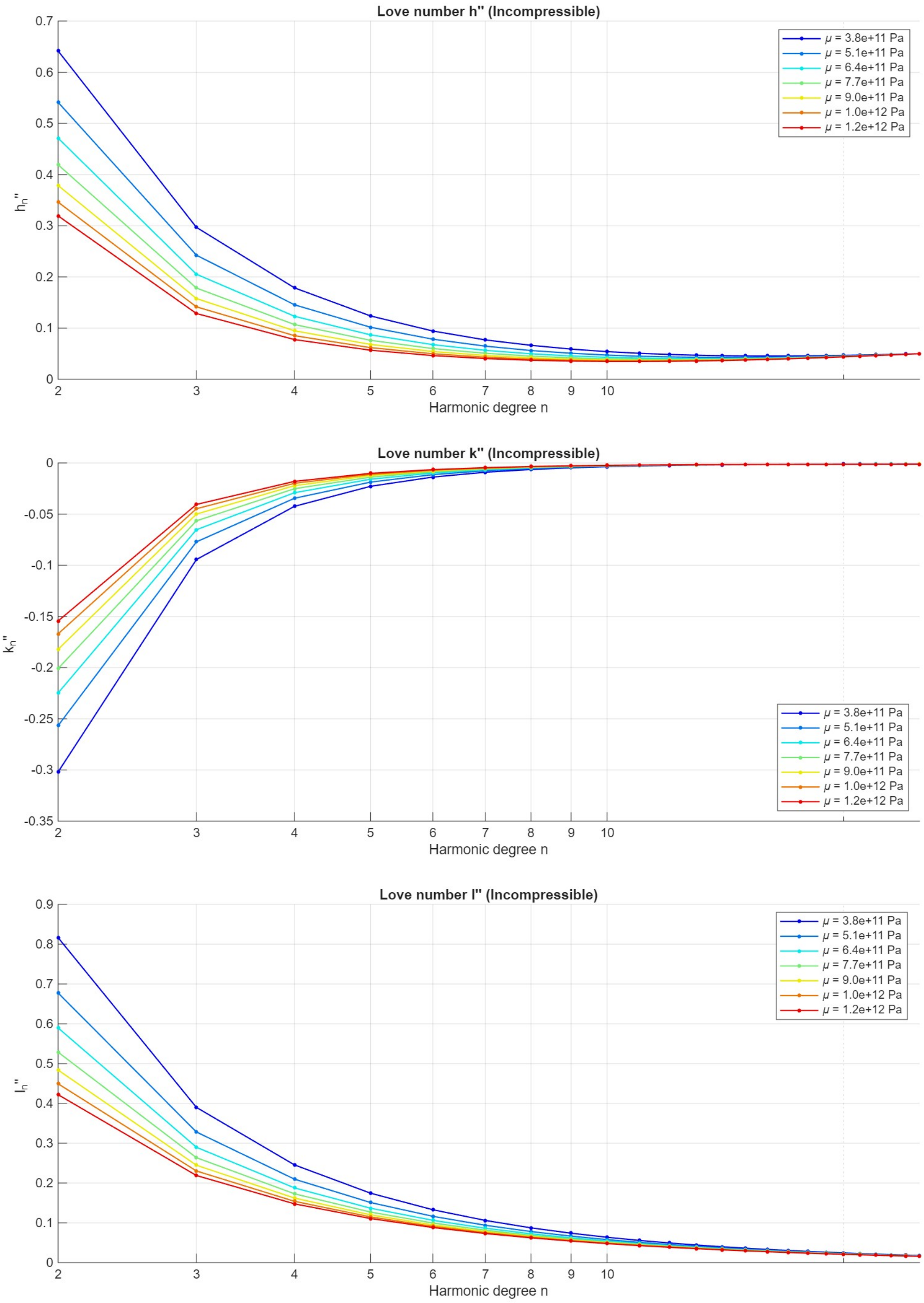

Figure 4.29: *Shear Love numbers plots for SE8-FS model up to degree $n = 25$ for the incompressible case. The input data of the model are reported in Tab. 3.11.*

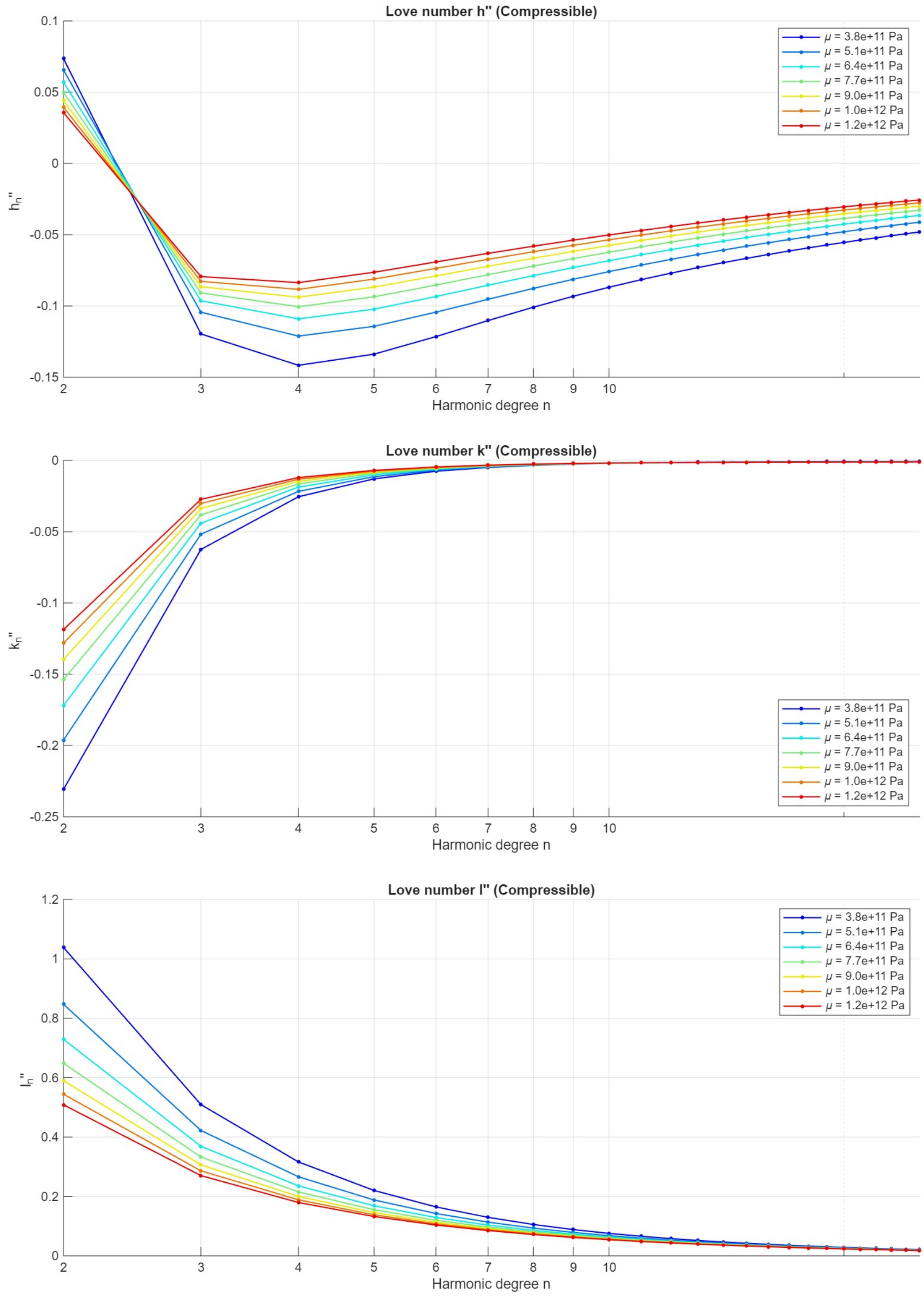

Figure 4.30: *Shear Love numbers plots for SE8-FS model up to degree $n = 25$ for the compressible case. The input data of the model are reported in Tab. 3.11.*

TLN	n	**Compressible**	**Incompressible**
h_n	2	0.6203	0.5410
	3	0.3723	0.3276
	4	0.2727	0.2455
	5	0.2178	0.1994
k_n	2	0.3067	0.2908
	3	0.1234	0.1183
	4	0.0689	0.0671
	5	0.0447	0.0440
l_n	2	0.1359	0.1543
	3	0.0346	0.0447
	4	0.0146	0.0199
	5	0.0078	0.0108

Table 4.13: **TLNs results for SE4-FS model**
Tidal Love numbers results for SE4-FS model for both compressible and incompressible cases corresponding to the average shear modulus of the mantle are reported up to the fifth harmonic degree.

LLN	n	**Compressible**	**Incompressible**
h'_n	2	-1.2125	-0.4956
	3	-1.4171	-0.5955
	4	-1.5519	-0.6616
	5	-1.6613	-0.7099
k'_n	2	-0.3082	-0.2611
	3	-0.2460	-0.2136
	4	-0.2027	-0.1802
	5	-0.1727	-0.1562
l'_n	2	0.0401	-0.1654
	3	0.0709	-0.0932
	4	0.0715	-0.0629
	5	0.0663	-0.0477

Table 4.14: **LLNs results for SE4-FS model**
Load Love numbers results for SE4-FS model for both compressible and incompressible cases corresponding to the average shear modulus of the mantle are reported up to the fifth harmonic degree.

SLN	n	Compressible	Incompressible
h''_n	2	0.0909	0.3333
	3	-0.0381	0.1419
	4	-0.0573	0.0842
	5	-0.0586	0.0590
k''_n	2	-0.1331	-0.1629
	3	-0.0343	-0.0459
	4	-0.0146	-0.0201
	5	-0.0078	-0.0109
l''_n	2	0.4487	0.3733
	3	0.2240	0.1789
	4	0.1434	0.1149
	5	0.1028	0.0834

Table 4.15: **SLNs results for SE4-FS model**
Shear Love numbers results for SE4-FS model for both compressible and incompressible cases corresponding to the average shear modulus of the mantle are reported up to the fifth harmonic degree.

TLN	n	Compressible	Incompressible
h_n	2	0.9377	0.8006
	3	0.6013	0.5152
	4	0.4582	0.4018
	5	0.3743	0.3348
k_n	2	0.4452	0.4232
	3	0.1911	0.1829
	4	0.1116	0.1081
	5	0.0746	0.0728
l_n	2	0.1936	0.2398
	3	0.0501	0.0733
	4	0.0209	0.0332
	5	0.0110	0.0181

Table 4.16: **TLNs results for SE8-FS model**
Tidal Love numbers results for SE8-FS model for both compressible and incompressible cases corresponding to the average shear modulus of the mantle are reported up to the fifth harmonic degree.

LLN	n	Compressible	Incompressible
h'_n	2	-2.0042	-0.7634
	3	-2.3926	-0.9620
	4	-2.6461	-1.1050
	5	-2.8430	-1.2118
k'_n	2	-0.4826	-0.3935
	3	-0.4053	-0.3390
	4	-0.3448	-0.2966
	5	-0.2992	-0.2632
l'_n	2	0.1233	-0.2698
	3	0.1500	-0.1560
	4	0.1386	-0.1056
	5	0.1224	-0.0796

Table 4.17: **LLNs results for SE8-FS model**
Load Love numbers results for SE8-FS model for both compressible and incompressible cases corresponding to the average shear modulus of the mantle are reported up to the fifth harmonic degree.

SLN	n	Compressible	Incompressible
h''_n	2	0.0498	0.4192
	3	-0.0908	0.1783
	4	-0.1005	0.1069
	5	-0.0936	0.0761
k''_n	2	-0.1538	-0.2008
	3	-0.0382	-0.0566
	4	-0.0164	-0.0251
	5	-0.0090	-0.0139
l''_n	2	0.6487	0.5287
	3	0.3327	0.2637
	4	0.2152	0.1729
	5	0.1553	0.1270

Table 4.18: **SLNs results for SE8-FS model**
Shear Love numbers results for SE8-FS model for both compressible and incompressible cases corresponding to the average shear modulus of the mantle are reported up to the fifth harmonic degree.

3 Discussion

3.1 Earth LNs

Looking at TLNs plots in Figs. 4.1 and 4.4, all of them show an exponential decaying trend with the increase of harmonic degree. The most meaningful degree is the second and generally each TLN becomes very small after the fifth degree. These trends are already known in the literature and confirm the validity of the numerical integration performed by the code [Munk and MacDonald, 1975].
Looking at LLNs plots in Figs. 4.2 and 4.5, h' shows a global decreasing trend with the increase of degree after an initial non-monotonic behavior until reaching $n = 5$. k' shows an asymptotic increasing trend towards zero starting from negative values, while l' asymptotically approaches zero starting from negative domain in the incompressible case and from positive domain in the compressible case. Expanding the integration up to degree $n = 300$ and more, it is possible to verify for compressible LLNs the same general behavior shown in Figs. 2.3 and 2.7 of [Spada et al., 2025] by viscoelastic LLNs.
Looking at SLNs plots in Figs. 4.3 and 4.6, l'' appears to be the most meaningful SLN to evaluate the shear response of *FS* model, as justified by theory alone, but it is not so different from the other SLNs in the *FOC* case. h'' and k'' asymptotically reach zero value very fast, even if the radial SLN approaches zero from different positive and negative domains, for the incompressible and compressible case, respectively.

For both *FS* and *FOC* models, considering only the second degree results:

- for tidal perturbations, compressible h_2 and k_2 are larger than the analogous TLNs of incompressible case. This confirms that if a planetary body could locally rearrange its internal mass, the related radial deformations of the surface are larger and the gravitational potential of the body itself amplifies the action of the perturbative external potential more than in the incompressible approximation.
  In Tab. 4.19 the comparison between our *FS* results and TLNs from literature are reported, highlighting their percentage differences. Our results generally overestimate the known values of TLNs. For h_2 and k_2, the difference does not exceed more than 22 % of the referenced values, while for l_2 we have obtained much greater values than the ones reported in past publications. From the comparison, we find out that our incompressible results are more comparable to the latter than the compressible ones, even if all the referenced works assumed compressible models. Due to this and noting that not all of those papers considered the same interior models we have adopted here, we are confident that our code does not overestimate systematically TLNs values, but it is a behavior shown by the selected planetary profiles with respect to those specific works;

- for mass loadings, all the LLNs are negative as expected: in fact, while a positive

tidal potential is related to a mass that does not stay in contact with the planetary body, exerting an outward attractive action on its components, a mass load is in contact with the body, pushing its surface downwards. The loading deformation response is reversed with respect to the tidal deformation response. Despite that, compressible h'_2 and k'_2 are still larger in absolute value than their incompressible counterparts, for the same reason exposed for tidal case.
In Tab. 4.20 the comparison between our *FS* results and LLNs from literature are reported, highlighting their percentage differences. We find out that incompressible results for h'_2 and l'_2 are not comparable anymore with the values from the mentioned papers, due to differences from about 50 % up to more than 400 %. Compressible LLNs agree with the reference values, showing an underestimation of radial LLN at maximum of 11 % and an overestimation of potential LLN of the same percentage. Tangential LLN shows the greatest range of differences from the known values, still remaining under a 25 % difference from them. The best agreement of our compressible results appears to be with LLNs reported in [Na and Baek, 2011], with a percentage difference that remains under 10 % for all the LLNs;

- for perturbations related to shear forces, positive radial SLNs are associated with negative potential SLNs in both compressible and incompressible assumptions and for both *FS* and *FOC* models. Both global models show h''_2, k''_2 values that are lower than the previous h_2, k_2, h'_2, k'_2, in absolute value: this shows that the radial and potential response to shear forcing is limited, even if not null. Note that the incompressible case presents larger radial and potential deformations than the compressible case, but lower tangential LN: if the planet can locally rearrange its mass, the deformations induced by shear forces are more intense tangentially than radially; if the planet is incompressible, deformations occur in all the possible directions with a larger amplitude.
  l''_2 is always positive, confirming that tangential deformations of the planetary surface happen consistently with the direction of the applied shear force.

In the case of tidal and load perturbations, there are no substantial differences between the LNs obtained for *FS* and *FOC* models, even if the results of the latter are a little larger than the *FS* ones in absolute value: for example, *FOC* h_2 is 0.6 % greater than *FS* h_2. This is the consequence of the presence of a fluid outer core in the differentiated model of the Earth: a fluid layer increases the deformability of the planet, but its deep radial location does not allow an increase greater than 1 %, at least with the planetary parameters adopted in this work. Focusing on the second degree compressible LNs, the only result that does not follow this general behavior is *FOC* h'_2, that is 1.37 % lower than its *FS* value.
Considering shear deformations, *FS* SLNs are much larger than *FOC* SLNs, except for the radial one: for compressible models, *FS* k''_2 is 95 % larger than its *FOC* value, *FS* l''_2 is 110 % larger than its *FOC* value, while *FS* h''_2 is 4.9 % lower than its *FOC* value.

Original work	Δh^c	Δh^{inc}	Δk^c	Δk^{inc}	Δl^c	Δl^{inc}
[Kaula, 1963]	+12 %	+0.77 %	+14 %	+10 %	+35 %	+56 %
[Longman, 1966]	+14 %	+2.7 %	+20 %	+15 %	+39 %	+59 %
[Saito, 1974]	+15 %	+3.3 %	+21 %	+16 %	+34 %	+54 %
[Baker, 1984]	+14 %	+1.9 %	+19 %	+14 %	+35 %	+56 %
[Agnew, 2005]	+16 %	+4.2 %	+22 %	+17 %	+37 %	+58 %

Table 4.19: **Second degree TLNs comparison**
Percentage differences between second degree TLNs taken from FS results in Tab. 4.1 and TLNs from mentioned papers are reported, for both compressible and incompressible cases. [Baker, 1984] originally reported a range of validity for TLNs values, so we have chosen to compute and use the central value of each range for the comparison.

Original work	$\Delta h'^{\,c}$	$\Delta h'^{\,inc}$	$\Delta k'^{\,c}$	$\Delta k'^{\,inc}$	$\Delta l'^{\,c}$	$\Delta l'^{\,inc}$
[Kaula, 1963]	−7.9 %	−48 %	+11 %	−7.5 %	−13 %	+379 %
[Longman, 1966]	−10 %	−49 %	+8.4 %	−9.6 %	−22 %	+331 %
[Farrell, 1972]	−9.7 %	−49 %	+9.1 %	−9.0 %	−16 %	+361 %
[Saito, 1974]	−11 %	−49 %	+8.9 %	−9.1 %	+6.3 %	+485 %
[Na and Baek, 2011]	−9.9 %	−49 %	+8.9 %	−9.2 %	−4.1 %	+427 %

Table 4.20: **Second degree LLNs comparison**
Percentage differences between absolute values of second degree LLNs taken from FS results in Tab. 4.2 and LLNs from mentioned papers are reported, for both compressible and incompressible cases. Note that, due to negative signs of LLNs, an increase in absolute value indicates a decrease of the related LLN, and vice versa. Tangential LLN is originally reported having positive sign in all the mentioned papers.

The *E-FOC* results verify the relations (2.250) and (2.251) between LNs of different type. The agreement between the formulas and the numerically-integrated compressible LNs is reported in Tabs. 4.21 and 4.22, respectively. It is possible to verify the same for the incompressible LNs.

$\boldsymbol{n}$	$\boldsymbol{h_n - k_n}$	$\boldsymbol{-k'_n}$
2	0.3395	0.3395
3	0.2308	0.2308
4	0.1618	0.1619
5	0.1251	0.1251

Table 4.21: **Check of Eq. (2.250) for the compressible *E-FOC* LNs**
The two terms of Eq. (2.250) are reported and compared for different harmonic degrees. They coincide within a few parts in the last significant digit, proving the validity of the relation first introduced in [Saito, 1978]. For the calculations, the compressible LNs of the Earth are taken from Tabs. 4.4 and 4.5 up to the fifth harmonic degree.

$\boldsymbol{n}$	$\boldsymbol{l_n}$	$\boldsymbol{-k''_n}$	$\boldsymbol{h''_n + l'_n}$
2	0.1182	0.1182	0.1182
3	0.0199	0.0199	0.0199
4	0.0080	0.0080	0.0080
5	0.0048	0.0048	0.0048

Table 4.22: **Check of Eq. (2.251) for the compressible *E-FOC* LNs**
The two terms of Eq. (2.251) are reported and compared for different harmonic degrees. They coincide, proving the validity of the relation first introduced in [Saito, 1978]. For the calculations, the compressible LNs of the Earth are taken from Tabs. 4.4, 4.5 and 4.6 up to the fifth harmonic degree.

3.2 $2\,M_\oplus$ super-Earth LNs

First of all, consider the super-Earth with $2\,M_\oplus$ size as the most similar in dimension to the Earth.
Its TLNs, displayed in Fig. 4.7, 4.8, 4.13 and 4.14, show the same decaying behavior shown by the TLNs of the Earth, for both incompressible and compressible cases and for both *FS* and *FOC* models.
Its LLNs, displayed in Fig. 4.9, 4.10, 4.15 and 4.16, show the same behavior of the LLNs of the Earth, that is, a decreasing trend for h', an increasing trend towards zero for k' and an asymptotic trend towards a near-zero value for l'. l' tends to reach a near-zero value starting from the positive domain in the compressible case and from the negative domain in the incompressible case, as for the load results of the Earth. If we expand the integration up to $n = 300$ and more, we might see that l' shows an oscillating trend around a near-zero value instead of settling at a constant value, but for the purposes of this work we will focus on lower degree LNs and neglect the asymptotic behavior. Also, we must highlight that *FOC* h' has a stiffer decreasing trend than *FS* h', as the presence of a fluid outer core makes the planet more deformable at lower degrees with respect to a fully solid one.
Its SLNs, displayed in Fig. 4.11, 4.12, 4.17 and 4.18, show the same behavior of the SLNs of the Earth too, *i.e.* asymptotic trends towards zero for them all, faster for the radial and potential LNs than for the tangential one. The compressible h'' shows the same inversion point between degrees 3 and 5, as for the compressible results of the Earth.

Considering only the second degree results:

- for tidal perturbations, both compressible and incompressible TLNs are smaller than the analogous TLNs of the Earth. This result suggests that super-Earths with $2\,M_\oplus$ size manifest a stiffer response to tidal perturbations than the Earth, due to the increase in planetary elastic parameters values. The F ratio (2.246) has been used to describe a simple homogeneous model in the previous Chapter, but it is capable of providing useful hints on complex cases too. Considering this quantity, we can say that the rigidity has more weight than the gravitational terms on a super-Earth of $2\,M_\oplus$, and this prevents the planet from getting deformed as much as the Earth. For example, *SE2-FS* compressible TLNs have the following percentage differences from their counterparts of the Earth: h_2 is 37 % lower than the *E-FS* value; k_2 is 38 % lower than the *E-FS* value; l_2 is 6.6 % lower than the *E-FS* value. The increase in mass and radius of this planetary class is still too low compared to the increase in its rigidity profile to enable a tidal deformation that is similar to or more intense than the solid tides manifested by the Earth;

- for mass loadings, the LLNs of *SE2-FS* model are lower in absolute value than *E-FS* LLNs, and this is still explainable by the previous considerations on tidal perturbations. For the compressible case, h'_2 is 13 % lower than the *E-FS* value; k'_2 is 36 % lower than the *E-FS* value; l'_2 is 64 % lower than the *E-FS* value. However, if we consider LLNs results for *SE2-FOC* model, we find out that they are larger in absolute value than *E-FOC* LLNs: the presence of a more extended fluid outer core than the one of the Earth produces a sensitive increase in load deformations. For compressible LLNs of *SE2-FOC* model, h'_2 is 22 % larger than the *E-FOC* value in absolute value; k'_2 is 7.5 % larger than the *E-FOC* value, in absolute value;

- for perturbations associated with shear forces, SLNs are smaller than the SLNs of the Earth, except for the tangential SLN of *SE2-FOC* model, that is about 33 % larger than its *E-FOC* counterpart. The increase in the rigidity profile of the planet can justify the general decrease in SLNs values, but the presence of a fluid outer core produces a slight increase in the tangential shear deformation manifested by the surface.

The LNs results of *FOC* model are still generally larger than *FS* results, confirming the previous discussion presented for the Earth, even if there are some exceptions. Focusing on the second degree compressible LNs, the results that do not respect this general behavior are: *FOC* k_2, that is 12 % lower than the *FS* value; *FOC* l_2, that is 9.0 % lower than the *FS* value; and *FOC* k''_2, that is 7.1 % lower than the *FS* value.
We have to recall that adopting the fluid outer core hypothesis on a super-Earth of $2\,M_\oplus$ size is not consistent with the discussion presented in [Valencia et al., 2006]. This work proved that the Earth size is the maximum planetary mass allowing the presence of a fluid internal layer, due to the relatively low internal pressure and internal heating state. We have evaluated such a condition for this super-Earth class only to be able to make a comparison between the Earth and the super-Earth most similar in size to it. The realistic LNs results to consider are the values obtained for the *SE2-FS* model.

The *SE2-FOC* results verify the relations (2.250) and (2.251) between LNs of different type. The agreement between the formulas and the numerically-integrated compressible LNs is reported in Tabs. 4.23 and 4.24, respectively. It is possible to verify the same for the incompressible LNs.

Thanks to the generation of the shear modulus of the mantle in a realistic interval of values, we see that the stiffer the mantle (*i.e.* the larger the shear modulus), the faster the decreasing trend of LNs and the lower their absolute values. This behavior is extremely evident for the k', l' and h'' plots, but it is shown by all LNs displayed in the yellow-to-red color scale, *i.e.* the largest shear modulus tested values. This study is repeatable for different planetary parameters in order to obtain all the dependencies on them shown by Love numbers, for many different combinations of internal profiles.

n	$h_n - k_n$	$-k'_n$
2	0.3651	0.3651
3	0.2451	0.2451
4	0.1727	0.1728
5	0.1341	0.1341

Table 4.23: **Check of Eq. (2.250) for the compressible *SE2-FOC* LNs**
The two terms of Eq. (2.250) are reported and compared for different harmonic degrees. They coincide within a few parts in the last significant digit, proving the validity of the relation first introduced in [Saito, 1978]. For the calculations, the compressible LNs of the super-Earth of $2\,M_\oplus$ *are taken from Tabs. 4.10 and 4.11 up to the fifth harmonic degree.*

n	l_n	$-k''_n$	$h''_n + l'_n$
2	0.0977	0.0977	0.0977
3	0.0196	0.0196	0.0197
4	0.0080	0.0080	0.0080
5	0.0047	0.0047	0.0046

Table 4.24: **Check of Eq. (2.251) for the compressible *E-FOC* LNs**
The two terms of Eq. (2.251) are reported and compared for different harmonic degrees. They coincide within a few parts in the last significant digit, proving the validity of the relation first introduced in [Saito, 1978]. For the calculations, the compressible LNs of the super-Earth of $2\,M_\oplus$ *are taken from Tabs. 4.10, 4.11 and 4.12 up to the fifth harmonic degree.*

3.3 4 and 8 $M_\oplus$ super-Earth LNs

The super-Earths of 4 and 8 $M_\oplus$ sizes verify the same global LNs trends discussed before, displayed from Fig. 4.19 to 4.30.

Focusing on the second degree results, we discuss only compressible models due to the fact that planetary high pressure regimes are well-described by taking compressibility into consideration, as shown in [Valencia et al., 2006].
Consider the super-Earth with 4 $M_\oplus$ size. Its LNs are all larger than the respective LNs values of the super-Earth of 2 $M_\oplus$: this suggests that this planetary size of super-Earths has reacquired a balance in the rigidity-on-gravity ratio F and can manifest more intense deformations. Adding to it, comparing *SE4* results with the results we have found for the Earth, the deformation response between them is quite similar and even more intense for certain *SE4* LNs. If we consider the most meaningful LNs for each kind of deformation, we have:

- for TLNs, h_2 is 12 % lower and k_2 is 16 % lower than h_2 and k_2 of the Earth, respectively. The tidal deformability of this super-Earth class is weaker than the one manifested by the Earth, but TLNs still do not differ more than 20 % from each other in the two cases. The increase in gravitational parameters, *i.e.* density profile and internal radii of each layer, is able to balance the increase in rigidity, producing a tidal response that is similar to the one manifested by the Earth;

- for LLNs, h'_2 is 34 % greater than h'_2 of the Earth while k'_2 is 8.2 % lower than k'_2 of the Earth, in absolute value. The loading deformability is radially enhanced with respect to the Earth, while the planetary potential does not show the same positive variation. Despite that, k'_2 still remains under a 10 % difference with terrestrial k'_2;

- for SLNs, l''_2 is 5.4 % lower than the l''_2 of the Earth, confirming a similar deformation response for shear forcing too.

Now consider the second degree results of compressible model of the super-Earth with 8 $M_\oplus$ size. This is the planetary class that shows the most intense response for all the possible deformation sources. In this case, gravitational terms of the planet dominate the F ratio: the increase in shear modulus profile is not sufficient to balance the enormous increase in mass and radius of the super-Earth.
Comparing SE8 results with the results obtained for the Earth, we have:

- for TLNs, h_2 is 34 % greater and k_2 is 23 % greater than h_2 and k_2 of the Earth, respectively. Tidal deformability is considerably increased due to the dominance of gravitational parameters of this super-Earth class;

- for LLNs, h'_2 is 122 % greater and k'_2 is 44 % greater than h'_2 and k'_2 of the Earth, respectively. The loading deformability is the one that increases the most, with a difference over 40 % for both of the most significant Love numbers;
- for SLNs, l''_2 is 37 % greater than l''_2 of the Earth.

In conclusion, we introduce an important discussion about the sensitivity of results for the SE4 and SE8 models to the shear modulus of the mantle. Note that, for these two planetary models, the variation in the shear modulus of the mantle produces much greater variations in LNs values for the decreasing shear modulus side with respect to the increasing side. We can observe this behavior also in *E-FS*, *E-FOC* and *SE2* plots, but it is mostly evident in Figs. 4.21, 4.22, 4.27 and 4.28 and in h'' plot in Figs. 4.29 and 4.30. This suggests that, even if the step of variation is always the same, passing from a higher to a lower rigidity value produce a more intense change in LNs values than passing from a lower to a higher rigidity. We have observed this for the range of shear modulus centered in the average value calculated in Chapter 3, but we cannot exclude that this is a general behavior related to rigidity itself. To sum up, the sensitivity on the shear modulus of the mantle manifested by LNs variations is stronger by decreasing such value than increasing it to stiffer values.

A qualitative comparison between the deformation responses of the Earth and super-Earths is displayed in Fig. 4.31: blue arrows indicate deformations occurring on the Earth, while red arrows indicate deformations occurring on the three classes of super-Earths considered in this work. The deformation forces under which these planets get deformed are assumed to be unitary and normalized to the gravitational acceleration of each planet, in order to display the mutual differences in LNs of each model in the figure. The lengths of the arrows are proportional to the deformation induced on the surface, that is, to each type of Love number. For each planet, the most suitable model is considered for the representation of the deformation results, *i.e.* the compressible *FOC* Earth and the compressible *FS* super-Earths of 2, 4 and 8 $M_\oplus$ sizes.

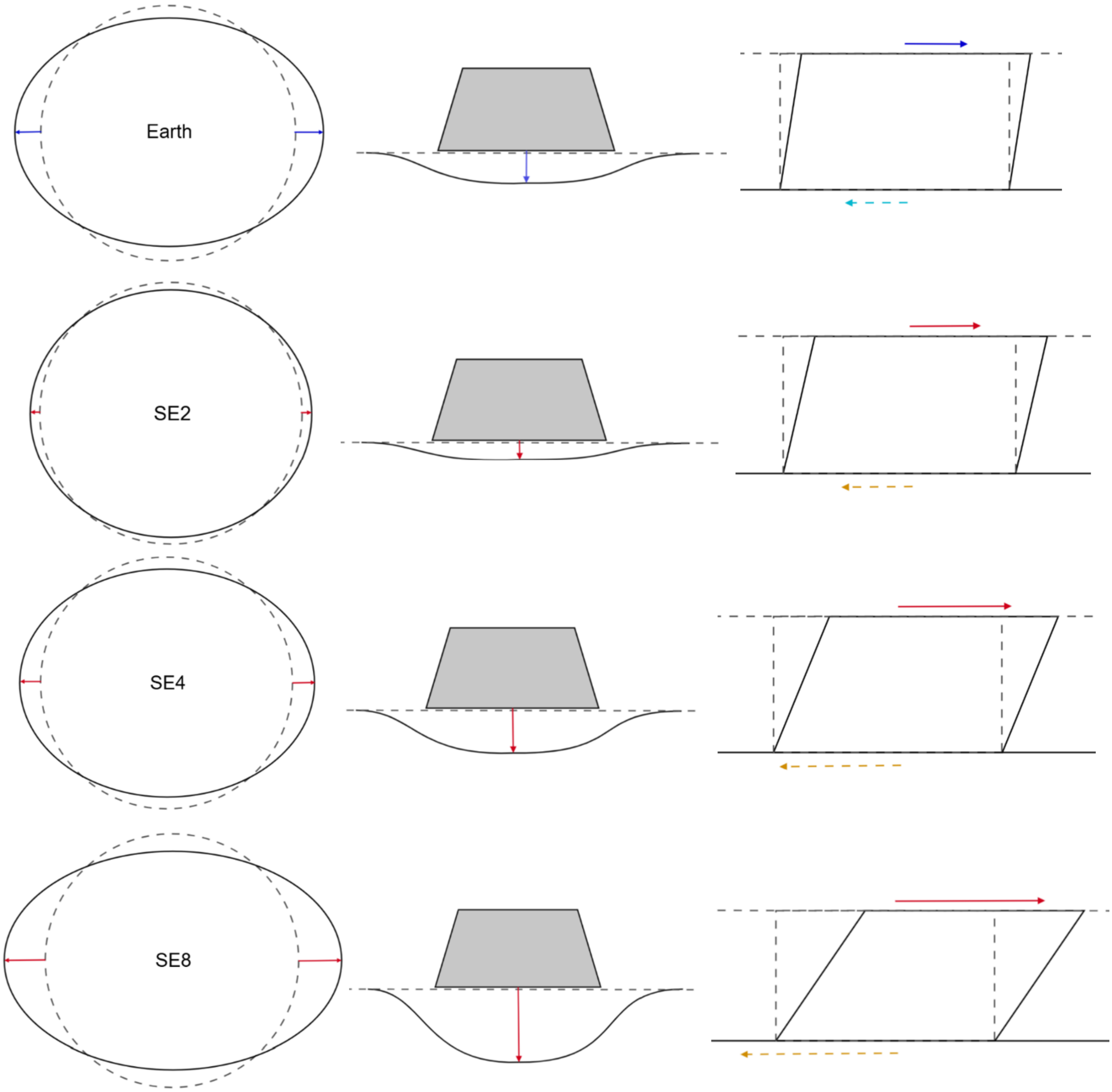

Figure 4.31: *Graphical representation of the different responses of the Earth and super-Earths to deformation. In each row, the Earth and the three sizes of super-Earth are represented, respectively. In each column, tidal, loading and shear deformations are represented, respectively. For tidal deformations, the dotted line denotes the unperturbed spherical planet while the continuous line denotes the deformed planet. For loading deformations, the dotted line denotes the unpertubed surface while the continuous line denotes the surface of the planet deformed under the grey surface load. For shear deformations, the dotted lines denote an unpertubed portion of the planetary surface while the continuous lines denote the deformation of the same portion. All the deformations are exaggerated in amplitude.*

Chapter 5

Conclusions

After the discussion on the models we have adopted and on the analysis we have carried out, I can now recall the results obtained in this study.

- Firstly, we have presented the code developed to carry out the numerical integration of planetary deformation. Adopting a classical Runge-Kutta integration structure, it provides a useful method for the evaluation of LNs of a three- or four-layered rocky planet, accounting for the possible presence of fluid layers, too. The user is free to select the profiles of internal parameters to associate with the rocky interior to be reproduced. We have also shown how we have tested the code to prove its validity.
  In addition, we have presented the method through which we have been able to reconstruct the internal properties of super-Earths of different sizes.

- Then, we have evaluated a new set of Love numbers of the Earth, for all the three possible perturbation sources acting on the planet. The results are obtained for both incompressible and compressible models and for the two main internal differentiations assumed for our planetary model. For the PREM-based parameters adopted for the Earth, we have obtained TLNs values that overestimate the values presented in the past literature, while LLNs values generally underestimate the previously-known LLNs, except for compressible k' and incompressible l'. The past works mentioned for the comparison mainly presented LNs values of compressible models, so that we consider our compressible LNs results to be the most representative for such a comparison.
  We have also verified the relations between Love numbers of different type for the *FOC* results.

- Successively, we have evaluated the Love numbers for three classes of super-Earths depending on their size, of 2, 4 and 8 Earth masses, respectively. For all of them, the compressible results of fully solid interior models have been considered as the

most suitable Love numbers datasets to represent their deformability. For super-Earths of $2\,M_\oplus$, we have inferred that this super-Earth has a lower tidal and load deformation response with respect to the Earth, if we assume it to be fully solid. The deformation of the planet is controlled by the elastic response. If we assume it to have a fluid outer core, then LLNs are larger than their counterparts of the Earth, probably due to the larger extension of the fluid layer in the internal structure. In this case, we have verified again the validity of the relations between Love numbers of different types.
For super-Earths of $4\,M_\oplus$, LNs are comparable with LNs of the Earth in a range of at maximum $35\,\%$ difference. There is no dominance of rigidity or gravity over each other, and the deformability is quite similar to the one of the Earth despite the difference in global mass.
For super-Earths of $8\,M_\oplus$, we have observed a completely different response: this planetary class is so massive that gravitational terms rule over the rigidity, which does not increase sufficiently to balance the increase in mass and radius. The increases in the deformation responses are all larger than $20\,\%$ of LNs of the Earth.

- In the end, we have discussed the possibility of varying one of the parameters that describe the planetary model and its consequences on LNs variations. We have proposed the shear modulus of the mantle as the default choice, but the study can be repeated with all the other parameters to estimate to which of them LNs are the most sensitive and how.

In the future, many improvements can be made in the methods and approximations presented in this work. First, we would like to remind the reader that the code developed here is a basic implementation of numerical integration of planetary deformations. Currently, there are many codes and frameworks that allow the evaluation of Love numbers for planets having complex rheological models and internal differentiation [Martens et al., 2019, Melini et al., 2022, Renaud, 2025]. My code can be greatly improved with more stable and advanced integration techniques in order to provide a complete interface for solving the Love numbers evaluation problem.
Secondly, before considering the shear Love numbers obtained in this work as fully reliable, we recommend the reader to reproduce them independently employing other codes. We have not been able to find references in the past literature on the explicit evaluation of SLNs, so we could not properly compare them with any known dataset, as we have done for TLNs and LLNs instead. The only work that considered SLNs is [Saito, 1978], but it related them to the other Love numbers without proposing any explicit datasets, so we do not have any reference results to validate the output of our code. An independent estimation of these parameters is necessary to produce a critical comparison between shear Love numbers and to understand their differences under various conditions.
Last, a complete study of the parametric major control on Love numbers is strongly suggested. As done in [Kamata et al., 2016] for Ganymede, by studying LNs in different

parametric regimes, *i.e.* varying the testing ranges for different planetary parameters, it would be possible to obtain which planetary parameter is the one exerting the major control on Love numbers of different types. By relating different Love numbers values to various internal models of super-Earths, we would be able to infer constraints for the interiors of this class of exoplanets, in view of future possibility of indirect estimates of exoplanetary LNs.

Super-Earths are an emerging planetary class in the future research scenario: they represent one the most widespread planet classes in the universe, show Earth-like features on larger scales, and present potential suitable-to-life conditions. Studying their deformability is just one step closer to achieving a complete description of this exoplanetary class. The scientific community has developed advanced observational capabilities to study the furthest celestial bodies just in the last decades, and we expect that there will be massive improvements in these techniques in the next years. Only in 2026, for example, a study presented in [Zieba et al., 2026] reconstructed the surface composition of a super-Earth named *LHS 3844 b* for the first time, employing near-IR spectroscopy data. In the same year, [Conzo et al., 2026] revealed the presence of a super-Earth with estimated mass of about $8\,M_{\oplus}$ not so far from the Solar System, at 28 light years from it. Future results like these will be decisive for our knowledge on super-Earths and on the Earth too: understanding the nature of our planet is not completely independent from the understanding of the nature of the bigger rocky planetary bodies in the universe.

Appendix A
Spherical coordinate system

From cartesian to spherical coordinates

The most natural coordinate system (c.s.) to study a planetary problem is not the classic cartesian c.s. in (x, y, z) coordinates but the spherical c.s. in (r, θ, φ) coordinates, where $r \geqslant 0$ is the radial distance from the origin of the c.s., $0 \leqslant \theta \leqslant \pi$ is the colatitude and $0 \leqslant \varphi \leqslant 2\pi$ is the longitude.
Conversion from the spherical c.s. to the cartesian one is possible through the following relations:

$$\begin{cases} x = r\,\sin\,\theta\,\cos\,\varphi \\ y = r\,\sin\,\theta\,\sin\,\varphi \\ z = r\,\cos\,\theta \end{cases}, \tag{A.1}$$

and *vice versa*:

$$\begin{cases} r = \sqrt{x^2 + y^2 + z^2} \\ \theta = \arctan\,\left(\dfrac{\sqrt{x^2 + y^2}}{z}\right) \\ \varphi = \arctan\,\left(\dfrac{y}{x}\right) \end{cases}. \tag{A.2}$$

A generic vector $\vec{a}$ can be written as:

$$\vec{a} = a_x\,\widehat{x} + a_y\,\widehat{y} + a_z\,\widehat{z} = a_r\,\widehat{r} + a_\theta\,\widehat{\theta} + a_\varphi\,\widehat{\varphi}\,, \tag{A.3}$$

where the two sets of components can be put in relation via:

$$\begin{pmatrix} u_x \\ u_y \\ u_z \end{pmatrix} = \begin{pmatrix} \sin\theta\,\cos\varphi & \cos\theta\,\cos\varphi & -\sin\varphi \\ \sin\theta\,\sin\varphi & \cos\theta\,\sin\varphi & \cos\varphi \\ \cos\theta & -\sin\varphi & 0 \end{pmatrix} \begin{pmatrix} u_r \\ u_\theta \\ u_\varphi \end{pmatrix}, \tag{A.4}$$

or:

$$\begin{pmatrix} u_r \\ u_\theta \\ u_\phi \end{pmatrix} = \begin{pmatrix} \sin\theta\,\cos\varphi & \sin\theta\,\sin\varphi & \cos\theta \\ \cos\theta\,\cos\varphi & \cos\theta\,\sin\varphi & -\sin\theta \\ -\sin\theta & \cos\varphi & 0 \end{pmatrix} \begin{pmatrix} u_x \\ u_y \\ u_z \end{pmatrix} . \tag{A.5}$$

Differential operators

It is also possible to relate cartesian and spherical formulations of differential operators.

- The *gradient* operator $\vec{\nabla} f$ of a scalar function $f = f(x, y, z)$ in a cartesian c.s. is:

$$\vec{\nabla} f = \frac{\partial f}{\partial x}\,\widehat{x} + \frac{\partial f}{\partial y}\,\widehat{y} + \frac{\partial f}{\partial z}\,\widehat{z}\,, \tag{A.6}$$

while in spherical coordinates:

$$\vec{\nabla} f = \frac{\partial f}{\partial r}\,\widehat{r} + \frac{1}{r}\frac{\partial f}{\partial \theta}\,\widehat{\theta} + \frac{1}{r\sin\theta}\frac{\partial f}{\partial \varphi}\,\widehat{\varphi}\,. \tag{A.7}$$

- The *divergence* operator $\vec{\nabla} \cdot \vec{f}$ of a vector function $\vec{f} = (f_x, f_y, f_z)$ in a cartesian c.s. is:

$$\vec{\nabla} \cdot \vec{f} = \frac{\partial f_x}{\partial x} + \frac{\partial f_y}{\partial y} + \frac{\partial f_z}{\partial z}\,, \tag{A.8}$$

while in spherical coordinates:

$$\vec{\nabla} \cdot \vec{f} = \frac{1}{r^2}\frac{\partial}{\partial r}(r^2 f_r) + \frac{1}{r\sin\theta}\frac{\partial}{\partial \theta}(f_\theta \sin\theta) + \frac{1}{r\sin\theta}\frac{\partial f_\varphi}{\partial \varphi}\,, \tag{A.9}$$

or analogously:

$$\vec{\nabla} \cdot \vec{f} = \frac{\partial f_r}{\partial r} + \frac{2 f_r}{r} + \frac{1}{r}\left(f_\theta \cot\theta + \frac{\partial f_\theta}{\partial \theta} + \frac{1}{\sin\theta}\frac{\partial f_\varphi}{\partial \varphi} \right) . \tag{A.10}$$

- The *laplacian* operator $\nabla^2 f$ of a scalar function $f = f(x,y,z)$ in a cartesian c.s. is:

$$\nabla^2 f = \frac{\partial^2 f}{\partial x^2} + \frac{\partial^2 f}{\partial y^2} + \frac{\partial^2 f}{\partial z^2}\,, \tag{A.11}$$

while in spherical coordinates:

$$\nabla^2 f = \frac{1}{r^2}\frac{\partial}{\partial r}\left(r^2\frac{\partial f}{\partial r}\right) + \frac{1}{r^2\sin\theta}\frac{\partial}{\partial\theta}\left(\sin\theta\frac{\partial f}{\partial\theta}\right) + \frac{1}{r^2\sin^2\theta}\frac{\partial^2 f}{\partial\varphi^2}\,, \tag{A.12}$$

or analogously:

$$\nabla^2 f = \frac{\partial^2 f}{\partial r^2} + \frac{2}{r}\frac{\partial f}{\partial r} + \frac{1}{r^2}\frac{\partial^2 f}{\partial\theta^2} + \frac{\cot\theta}{r^2}\frac{\partial f}{\partial\theta} + \frac{1}{r^2\sin^2\theta}\frac{\partial^2 f}{\partial\varphi^2}\,. \tag{A.13}$$

- The *curl* operator $\vec{\nabla}\times\vec{f}$ of a vector function $\vec{f} = (f_x, f_y, f_z)$ in a cartesian c.s. is:

$$\vec{\nabla}\times\vec{f} = \left(\frac{\partial f_z}{\partial y} - \frac{\partial f_y}{\partial z}\right)\widehat{x} + \left(\frac{\partial f_x}{\partial z} - \frac{\partial f_z}{\partial x}\right)\widehat{y} + \left(\frac{\partial f_y}{\partial x} - \frac{\partial f_x}{\partial y}\right)\widehat{z}\,, \tag{A.14}$$

while in spherical coordinates its components are:

$$\begin{aligned}
\left(\vec{\nabla}\times\vec{f}\right)_r &= \frac{1}{r\sin\theta}\left(\frac{\partial}{\partial\theta}(f_\varphi\sin\theta) - \frac{\partial f_\theta}{\partial\varphi}\right)\,,\\
\left(\vec{\nabla}\times\vec{f}\right)_\theta &= \frac{1}{r}\left(\frac{1}{\sin\theta}\frac{\partial f_r}{\partial\varphi} - \frac{\partial}{\partial r}(rf_\varphi)\right)\,,\\
\left(\vec{\nabla}\times\vec{f}\right)_\varphi &= \frac{1}{r}\left(\frac{\partial}{\partial r}(rf_\theta) - \frac{\partial f_r}{\partial\theta}\right)\,,
\end{aligned} \tag{A.15}$$

or analogously:

$$\begin{aligned}
\left(\vec{\nabla}\times\vec{f}\right)_r &= \frac{1}{r}\frac{\partial f_\varphi}{\partial\theta} + \frac{\cot\theta}{r}f_\varphi - \frac{1}{r\sin\theta}\frac{\partial f_\theta}{\partial\varphi}\,,\\
\left(\vec{\nabla}\times\vec{f}\right)_\theta &= \frac{1}{r\sin\theta}\frac{\partial f_r}{\partial\theta} - \frac{\partial f_\varphi}{\partial r} - \frac{f_\varphi}{r}\,,\\
\left(\vec{\nabla}\times\vec{f}\right)_\varphi &= \frac{\partial f_\theta}{\partial r} + \frac{f_\theta}{r} - \frac{1}{r}\frac{\partial f_r}{\partial\theta}\,.
\end{aligned} \tag{A.16}$$

Strain and stress tensors

In Chapter 2 we have associated a vector displacement $\vec{u}$ to the deformation, which in a cartesian c.s. can be written as $\vec{u} = (u_x, u_y, u_z)$.
This displacement defines the infinitesimal strain tensor ϵ_{ij} of the body associated to that deformation by Eq. (2.9), that we recall here below:

$$\epsilon_{ij} = \frac{1}{2}\left(\frac{\partial u_i}{\partial x_j} + \frac{\partial u_j}{\partial x_i}\right) , \tag{A.17}$$

where $i, j = x, y, z$, so that for example:

$$\epsilon_{xx} = \frac{\partial u_x}{\partial x} \quad , \quad \epsilon_{xy} = \frac{1}{2}\left(\frac{\partial u_x}{\partial y} + \frac{\partial u_y}{\partial x}\right) . \tag{A.18}$$

In spherical coordinates, the following relations are taken from [Takeuchi and Saito, 1972]:

$$\begin{aligned}
\epsilon_{rr} &= \frac{\partial u_r}{\partial r} , \\
\epsilon_{\theta\theta} &= \frac{1}{r}\frac{\partial u_\theta}{\partial \theta} + \frac{1}{r}u_r , \\
\epsilon_{\varphi\varphi} &= \frac{1}{r\sin\theta}\frac{\partial u_\varphi}{\partial \varphi} + \frac{1}{r}u_\theta \cot\theta + \frac{1}{r}u_r , \\
\epsilon_{r\theta} &= \frac{\partial u_\theta}{\partial r} - \frac{1}{r}u_\theta + \frac{1}{r}\frac{\partial u_r}{\partial \theta} , \\
\epsilon_{\theta\varphi} &= \frac{1}{r}\frac{\partial u_\varphi}{\partial \theta} - \frac{1}{r}u_\varphi \cot\theta + \frac{1}{r}u_r , \\
\epsilon_{\varphi r} &= \frac{1}{r\sin\theta}\frac{\partial u_r}{\partial \varphi} + \frac{\partial u_\varphi}{\partial r} - \frac{1}{r}u_\varphi .
\end{aligned} \tag{A.19}$$

As in cartesian coordinates, also in spherical ones the strain tensor is related to the stress tensor τ_{ij}. The relations between the two tensors are taken from [Takeuchi and Saito, 1972] and written specifically for the case of isotropic elastic bodies as:

$$\begin{aligned}
\tau_{rr} &= (\lambda + 2\mu)\epsilon_{rr} + \lambda(\epsilon_{\theta\theta} + \epsilon_{\varphi\varphi}) , \\
\tau_{\theta\theta} &= (\lambda + 2\mu)\epsilon_{\theta\theta} + \lambda(\epsilon_{rr} + \epsilon_{\varphi\varphi}) , \\
\tau_{\varphi\varphi} &= (\lambda + 2\mu)\epsilon_{\varphi\varphi} + \lambda(\epsilon_{rr} + \epsilon_{\theta\theta}) , \\
\tau_{r\theta} &= \mu\epsilon_{r\theta} , \\
\tau_{\theta\varphi} &= \mu\epsilon_{\theta\varphi} , \\
\tau_{\varphi r} &= \mu\epsilon_{\varphi r} .
\end{aligned} \tag{A.20}$$

Appendix B
Spherical Bessel functions

Unmodified spherical Bessel functions

As introduced in Chapter 2 and in-detail shown in [Arfken, 1985], the spherical Bessel equation for a function $f = f(x)$ reads:

$$x^2 \frac{\partial^2 f}{\partial x^2}(x) + 2x \frac{\partial f}{\partial x}(x) + (x^2 - n(n+1)) f(x) = 0\,, \tag{B.1}$$

whose regular solutions in $x = 0$ are the *regular spherical Bessel functions* of order n, defined as:

$$j_n(x) = \sqrt{\frac{\pi}{2x}} J_{n+\frac{1}{2}}(x)\,, \tag{B.2}$$

where $J_m(x)$ is the Bessel function of order m, while its singular solutions in $x = 0$ are the *singular spherical Bessel functions* of order n, defined as:

$$y_n(x) = (-1)^{n+1} \sqrt{\frac{\pi}{2x}} J_{-n-\frac{1}{2}}(x)\,. \tag{B.3}$$

For the sake of this thesis, only regular solutions are allowed to start the numerical integration near the planetary center. They are displayed in Fig. 5.1 up to degree $n = 4$.

Thanks to the recurrence relation:

$$j_{n-1}(x) + j_{n+1}(x) = \frac{2n+1}{x}\, j_n(x)\,, \tag{B.4}$$

it is possible to obtain the following relations for first and second derivatives of spherical Bessel functions:

$$j'_n(x) = j_{n-1}(x) - \frac{n+1}{x} j_n(x)\,, \tag{B.5}$$

$$j''_n(x) = -\frac{2}{x} j_{n-1}(x) + \frac{(n+1)(n+2) - x^2}{x^2} j_n(x)\,. \tag{B.6}$$

Modified spherical Bessel functions

If the argument x of spherical Bessel functions is pure imaginary: $x = iy$, where $y \in \mathbb{R}$, we have to consider the following modified spherical Bessel equation:

$$y^2 \frac{\partial^2 f}{\partial y^2}(iy) + 2y \frac{\partial f}{\partial x}(iy) - (y^2 + n(n+1))f(iy) = 0\,. \tag{B.7}$$

Its solutions are the *modified spherical Bessel functions* of order n, in form:

$$i_n(y) = \sqrt{\frac{\pi}{2y}} I_{n+\frac{1}{2}}(y)\,, \tag{B.8}$$

where $I_m(y)$ is the modified Bessel function of order m, so that:

$$I_n(y) = i^{-n} J_n(iy)\,, \tag{B.9}$$

hence:

$$i_n(y) = i^{-n} j_n(iy)\,, \tag{B.10}$$

Note that, in the previous notation, i_n indicates the modified spherical Bessel function, while i indicates the imaginary unit: $i^2 = -1$.
They are displayed in Fig. 5.1 up to degree $n = 4$.

The first and second derivatives of modified spherical Bessel functions are:

$$i'_n(y) = i_{n-1}(y) - \frac{n+1}{y} i_n(y)\,, \tag{B.11}$$

$$i''_n(y) = -\frac{2}{y} i_{n-1}(y) + \frac{(n+1)(n+2)+y^2}{y^2} i_n(x)\,. \tag{B.12}$$

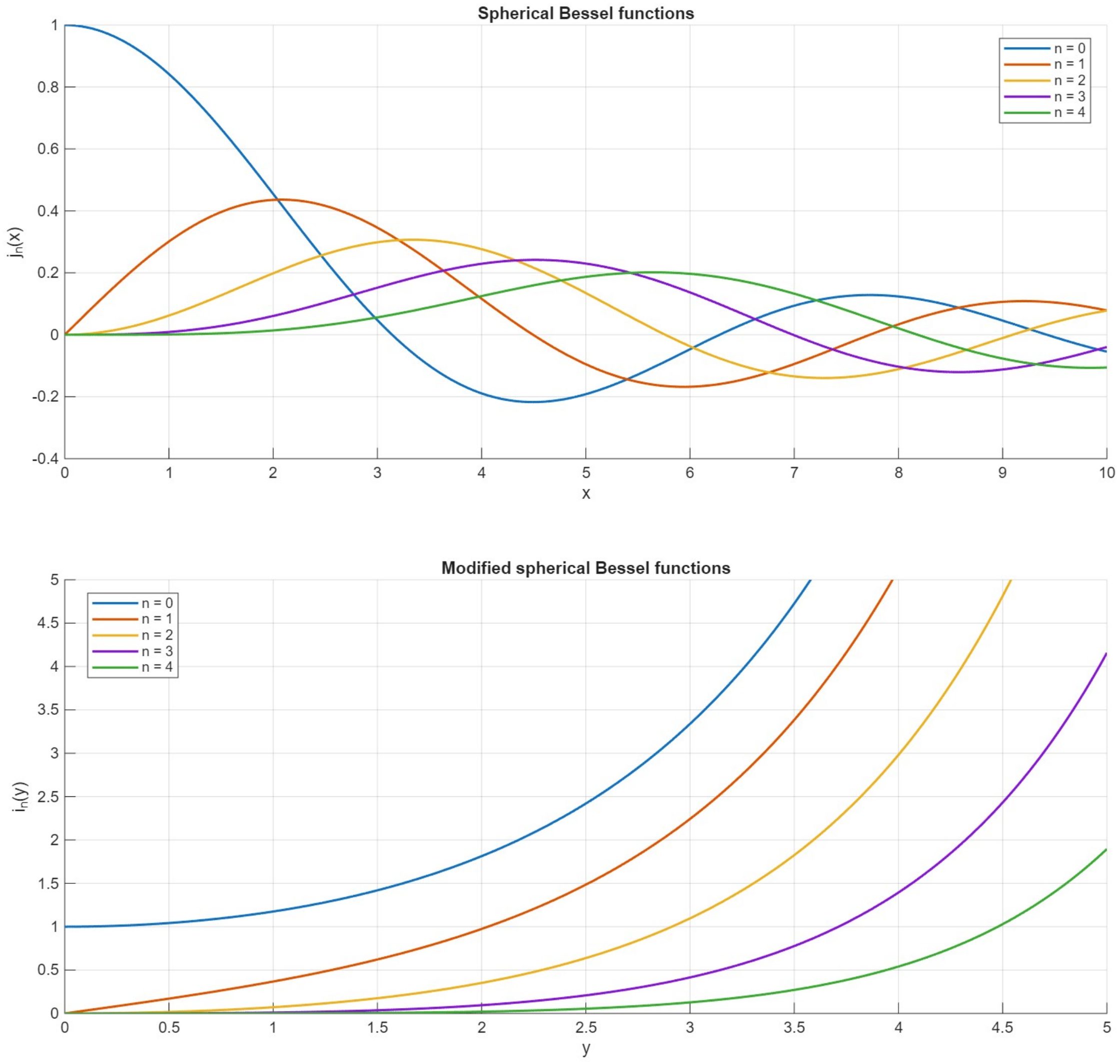

Figure 5.1: *In the upper image, spherical Bessel functions up to degree* $n = 4$ *are displayed in a range between* 0 *and* 10*. In the lower image, modified spherical Bessel functions up to degree* $n = 4$ *are displayed in a range between* 0 *and* 5*.*

Appendix C
Runge-Kutta numerical integration

Runge-Kutta method

The Runge-Kutta method is a linear single-step numerical method that estimates the value of a function at the end of the step using linear formulas to calculate provisional intermediate values in the interval. Here, I follow [Tinti and Zaniboni, 2025].

Consider an interval in the t variable domain between t_n and t_{n+1}, with width Δt, and an *Ordinary Differential Equation* (ODE) in form:

$$u'(t) = f\left(u(t), t\right) \,, \tag{C.1}$$

where $u(t)$ is a continuous function, $u'(t)$ is its continuous first derivative and $f(u(t), t)$ is a continuous function of $(u(t), t)$. Suppose we do not know any analytical formulation for $u(t)$, so that we have to solve the ODE numerically.
If we know the value of $u(t_n) = u_n$ and we have to obtain numerically the value of $u(t_{n+1}) = u_{n+1}$, we can estimate the value of u in the middle point of the interval $t_{n+\frac{1}{2}}$ by using another numerical formula, for example the explicit Euler formula (that is formally analogous to the first order Taylor expansion):

$$\widetilde{u}_{n+\frac{1}{2}} = u_n + \frac{1}{2}\Delta t\, f_n \,, \tag{C.2}$$

where $f(u(t_n), t_n) = f_n$ follows the same notation as u_n and the tilde indicates an intermediate value in the considered step.
It immediately follows from Eq. (C.1) that:

$$\widetilde{f}_{n+\frac{1}{2}} = f\left(\widetilde{u}_{n+\frac{1}{2}}, t_{n+\frac{1}{2}}\right) \,. \tag{C.3}$$

Finally, we evaluate u_{n+1} as:

$$u_{n+1} = u_n + \Delta t\, \widetilde{f}_{n+\frac{1}{2}} \,. \tag{C.4}$$

The generalized structure of the Runge-Kutta method of order s is made up of s intermediate points in the interval $[t_n, t_{n+1}]$ and it can be illustrated as:

1. choose s intermediate values $c_m \leqslant 1,\ m = 1, 2, ..., s$ so that each t_{n+c_m} point falls into the interval;

2. conventionally, the first intermediate value is chosen as $c_1 = 0$ so that the starting point is $t_{n+c_1} = t_n$. Calculate:

$$\widetilde{u}_{n+c_1} = u_n\,, \tag{C.5}$$

$$\widetilde{f}_{n+c_1} = f_n = f\left(\widetilde{u}_{n+c_1}, t_{n+c_1}\right)\,; \tag{C.6}$$

3. calculate:

$$\widetilde{u}_{n+c_2} = u_n + \Delta t\, \alpha_{2,1}\, \widetilde{f}_{n+c_1}\,, \tag{C.7}$$

$$\widetilde{f}_{n+c_2} = f\left(\widetilde{u}_{n+c_2}, t_{n+c_2}\right)\,; \tag{C.8}$$

4. calculate:

$$\widetilde{u}_{n+c_3} = u_n + \Delta t\left(\alpha_{3,1}\, \widetilde{f}_{n+c_1} + \alpha_{3,2}\, \widetilde{f}_{n+c_2}\right)\,, \tag{C.9}$$

$$\widetilde{f}_{n+c_3} = f\left(\widetilde{u}_{n+c_3}, t_{n+c_3}\right)\,; \tag{C.10}$$

5. iterate for each m value until $m = s$;

6. the unknown value u_{n+1} is finally evaluated as:

$$u_{n+1} = u_n + \Delta t\left(b_1 \widetilde{f}_{n+c_1} + b_2 \widetilde{f}_{n+c_2} + \ ...\ + b_s \widetilde{f}_{n+c_s}\right)\,. \tag{C.11}$$

The coefficients $\alpha_{m,p}\,,\ 2 \leqslant m \leqslant s\,,\ 1 \leqslant p \leqslant m-1$ and $b_q\,,\ 1 \leqslant q \leqslant s$ are related through the following *Butcher matrix*:

$$\begin{array}{c|cccccc}
0 & & & & & & \\
c_2 & \alpha_{1,2} & & & & & \\
c_3 & \alpha_{3,1} & \alpha_{3,2} & & & & \\
c_4 & \alpha_{4,1} & \alpha_{4,2} & \alpha_{4,3} & & & \\
... & ... & ... & ... & ... & & \\
c_s & \alpha_{s,1} & \alpha_{s,2} & \alpha_{s,3} & ... & \alpha_{s,s-1} & \\
\hline
 & b_1 & b_2 & b_3 & ... & b_{s-1} & b_s
\end{array}$$

where for each row it must be valid the following condition:

$$\sum_{p=1}^{m-1} \alpha_{m,p} = c_m \,. \tag{C.12}$$

Each coefficient b_q is found from the comparison between the explicit formula of $u(t_{n+1})$ and its s-th order Taylor expansion.

Fourth order Runge-Kutta method

Considering $s = 4$ and making all the discussion on Runge-Kutta coefficients explicit, from the comparison between this and the fourth order Taylor expansion of $u(t_{n+1})$ it is possible to reach the following conditions for b_q:

$$\begin{cases} b_1 + b_2 + b_3 + b_4 = 1 \\ b_2c_2 + b_3c_3 + b_4c_4 = \dfrac{1}{2} \\ \dfrac{1}{2}\left(b_3c_3^2 + b_4c_4^2\right) = \dfrac{1}{6} \\ \dfrac{1}{6}b_4c_4^3 = \dfrac{1}{24} \end{cases} \tag{C.13}$$

from which we obtain the following Butcher matrix:

$$\begin{array}{c|cccc} 0 & & & & \\ \frac{1}{2} & \frac{1}{2} & & & \\ \frac{1}{2} & 0 & \frac{1}{2} & & \\ 1 & 0 & 0 & 1 & \\ \hline & \frac{1}{6} & \frac{1}{3} & \frac{1}{3} & \frac{1}{6} \end{array}$$

Bibliography

[Agnew, 2005] Agnew, D. C. (2005). Earth tides: an introduction. *University of California, San Diego.*

[Alterman et al., 1959] Alterman, Z., Jarosch, H., and Pekeris, C. (1959). Oscillations of the Earth. *Proceedings of the Royal Society of London. Series A. Mathematical and Physical Sciences*, 252(1268):80–95.

[Arfken, 1985] Arfken, G. (1985). *Mathematical Methods for Physicists.* Elsevier, Academic Press.

[Backus, 1967] Backus, G. E. (1967). Converting vector and tensor equations to scalar equations in spherical coordinates. *Geophysical Journal International*, 13(1-3):71–101.

[Baker, 1984] Baker, T. (1984). Tidal deformations of the Earth. *Science Progress (1933-)*, pages 197–233.

[Barros et al., 2022] Barros, S. C., Akinsanmi, B., Boué, G., Smith, A., Laskar, J., Ulmer-Moll, S., Lillo-Box, J., Queloz, D., Cameron, A. C., Sousa, S., et al. (2022). Detection of the tidal deformation of WASP-103b at 3 σ with CHEOPS. *Astronomy & Astrophysics*, 657:A52.

[Belardinelli, 2025] Belardinelli, M. E. (2024/2025). Teaching material of "Tectonophysics" class. *Alma Mater Studiorum - Università di Bologna.*

[Binnington and Poisson, 2009] Binnington, T. and Poisson, E. (2009). Relativistic theory of tidal Love numbers. *Physical Review D—Particles, Fields, Gravitation, and Cosmology*, 80(8):084018.

[Brustein and Sherf, 2022] Brustein, R. and Sherf, Y. (2022). Classical Love number for quantum black holes. *Physical Review D*, 105(2):024044.

[Bullard and Gellman, 1954] Bullard, E. C. and Gellman, H. (1954). Homogeneous dynamos and terrestrial magnetism. *Philosophical Transactions of the Royal Society of London. Series A, Mathematical and Physical Sciences*, 247(928):213–278.

[Chinnery, 1975] Chinnery, M. A. (1975). The static deformation of an Earth with a fluid core: a physical approach. *Geophysical Journal International*, 42(2):461–475.

[Conzo et al., 2026] Conzo, G., Moriconi, M., and Correa Jr, S. A. (2026). Detection and characterization of the temperate super-Earth Gliese 48 b. *Open European Journal on Variable Stars*.

[Correia, 2014] Correia, A. C. (2014). Transit light curve and inner structure of close-in planets. *Astronomy & Astrophysics*, 570:L5.

[Coughlin et al., 2016] Coughlin, J. L., Mullally, F., Thompson, S. E., Rowe, J. F., Burke, C. J., Latham, D. W., Batalha, N. M., Ofir, A., Quarles, B. L., Henze, C. E., et al. (2016). Planetary candidates observed by Kepler. VII. The first fully uniform catalog based on the entire 48-month data set (Q1–Q17 DR24). *The Astrophysical Journal Supplement Series*, 224(1):12.

[Dziewonski and Anderson, 1981] Dziewonski, A. M. and Anderson, D. L. (1981). Preliminary reference Earth model. *Physics of the earth and planetary interiors*, 25(4):297–356.

[Farrell, 1972] Farrell, W. (1972). Deformation of the Earth by surface loads. *Reviews of Geophysics*, 10(3):761–797.

[Francioni, 2024] Francioni, L. (2024). Tidal response and Love numbers of the moons of Uranus. *Alma Mater Studiorum - University of Bologna*.

[Francioni, 2026] Francioni, L. (2026). `https://github.com/lfrancioni/Love-numbers-of-super-Earths`. Github.

[Gavrilov and Zharkov, 1977] Gavrilov, S. and Zharkov, V. (1977). Love numbers of the giant planets. *Icarus*, 32(4):443–449.

[Gilbert and Backus, 1968] Gilbert, F. and Backus, G. E. (1968). Approximate solutions to the inverse normal mode problem. *Bulletin of the Seismological Society of America*, 58(1):103–131.

[Goossens and Matsumoto, 2008] Goossens, S. and Matsumoto, K. (2008). Lunar degree 2 potential Love number determination from satellite tracking data. *Geophysical research letters*, 35(2).

[Hinderer, 2008] Hinderer, T. (2008). Tidal Love numbers of neutron stars. *The Astrophysical Journal*, 677(2):1216–1220.

[Kamata et al., 2016] Kamata, S., Kimura, J., Matsumoto, K., Nimmo, F., Kuramoto, K., and Namiki, N. (2016). Tidal deformation of Ganymede: Sensitivity of Love numbers on the interior structure. *Journal of Geophysical Research: Planets*, 121(7):1362–1375.

[Kaula, 1963] Kaula, W. M. (1963). Elastic models of the mantle corresponding to variations in the external gravity field. *Journal of Geophysical Research*, 68(17):4967–4978.

[Kellermann et al., 2018] Kellermann, C., Becker, A., and Redmer, R. (2018). Interior structure models and fluid Love numbers of exoplanets in the super-Earth regime. *Astronomy & Astrophysics*, 615:A39.

[Konopliv and Yoder, 1996] Konopliv, A. and Yoder, C. (1996). Venusian k2 tidal Love number from Magellan and PVO tracking data. *Geophysical research letters*, 23(14):1857–1860.

[Kramm et al., 2012] Kramm, U., Nettelmann, N., Fortney, J., Neuhäuser, R., and Redmer, R. (2012). Constraining the interior of extrasolar giant planets with the tidal Love number k2 using the example of HAT-P-13b. *Astronomy & Astrophysics*, 538:A146.

[Longman, 1966] Longman, I. (1966). Computation of Love numbers and load deformation coefficients for a model Earth. *Geophysical Journal International*, 11(1):133–137.

[Love, 1909] Love, A. E. H. (1909). The yielding of the Earth to disturbing forces. *Proceedings of the Royal Society of London. Series A, Containing Papers of a Mathematical and Physical Character*, 82(551):73–88.

[Love, 1911] Love, A. E. H. (1911). *Some problems of geodynamics: being an essay to which the Adams prize in the University of Cambridge was adjudged in 1911*. CUP Archive.

[Mao et al., 2001] Mao, H., Xu, J., Struzhkin, V., Shu, J., Hemley, R., Sturhahn, W., Hu, M., Alp, E., Vocadlo, L., Alfè, D., et al. (2001). Phonon density of states of iron up to 153 gigapascals. *Science*, 292(5518):914–916.

[Martens, 2016] Martens, H. R. (2016). *Using Earth Deformation Caused by Surface Mass Loading to Constrain the Elastic Structure of the Crust and Mantle*. PhD thesis, California Institute of Technology.

[Martens et al., 2019] Martens, H. R., Rivera, L., and Simons, M. (2019). LoadDef: A Python-based toolkit to model elastic deformation caused by surface mass loading on spherically symmetric bodies. *Earth and Space Science*, 6(2):311–323.

[Mazarico et al., 2014] Mazarico, E., Barker, M. K., Neumann, G. A., Zuber, M. T., and Smith, D. E. (2014). Detection of the lunar body tide by the Lunar Orbiter Laser Altimeter. *Geophysical Research Letters*, 41(7):2282–2288.

[Melchior, 1983] Melchior, P. (1983). *The Tides of the Planet Earth*. Elsevier Science & Technology.

[Melini et al., 2022] Melini, D., Saliby, C., and Spada, G. (2022). On computing viscoelastic Love numbers for general planetary models: the ALMA3 code. *Geophysical Journal International*, 231(3):1502–1517.

[Mendenhall, 2026] Mendenhall, B. (2026). Astronomers confirm potentially habitable exoplanet in the solar neighborhood. `https://www.astronomy.com/science/astronomers-confirm-potentially-habitable-exoplanet-in-the-solar-neighborhood/`. Accessed: May 12, 2026.

[Molodensky, 1976] Molodensky, S. (1976). Changes in the Love Numbers during variation of an Earth structure scheme. *Izvestiya, Academy of Sciences, USSR.: Physics of the solid earth*, 12:86.

[Molodensky, 1977] Molodensky, S. (1977). Relation between Love numbers and load factors. *Izv. Phys. Solid Earth*, 13:147–149.

[Munk and MacDonald, 1975] Munk, W. and MacDonald, G. (1975). *The Rotation of the Earth: A Geophysical Discussion*. Cambridge Monographs on Mechanics. Cambridge University Press.

[Na and Baek, 2011] Na, S.-H. and Baek, J. (2011). Computation of the load Love number and the load Green's function for an elastic and spherically symmetric Earth. *Journal of the Korean Physical Society*, 58(5):1195–1205.

[Nakajima et al., 2026] Nakajima, M., Harter, S. K., Jasko, A. V., Polsin, D. N., Szumila, I., Cone, K. A., Lherm, V., Blackman, E. G., Dragulet, F., Stixrude, L., et al. (2026). Electrical conductivities of (Mg, Fe) O at extreme pressures and implications for planetary magma oceans. *Nature Astronomy*, pages 1–10.

[NASA, 2026] NASA (2026). NASA Exoplanet Archive. NASA Exoplanet Science Institute - *California Institute of Technology*. `https://exoplanetarchive.ipac.caltech.edu/cgi-bin/TblView/nph-tblView?app=ExoTbls&config=PS`. Accessed: May 8, 2026.

[Oganov and Ono, 2004] Oganov, A. R. and Ono, S. (2004). Theoretical and experimental evidence for a post-perovskite phase of MgSiO3 in Earth's D layer. *Nature*, 430(6998):445–448.

[Okubo and Saito, 1983] Okubo, S. and Saito, M. (1983). Partial derivative of Love numbers. *Bulletin géodésique (1976-1995)*, 57(1):167–179.

[Petricca et al., 2022] Petricca, F., Genova, A., Goossens, S., Iess, L., and Spada, G. (2022). Constraining the internal structures of Venus and Mars from the gravity response to atmospheric loading. *The Planetary Science Journal*, 3(7):164.

[Poulsen, 2009] Poulsen, S. K. (2009). Tidal Deformation of the Solid Earth - A Finite Difference Discretization. *Niels Bohr Institute, University of Copenhagen.*

[Ragozzine and Wolf, 2009] Ragozzine, D. and Wolf, A. S. (2009). Probing the interiors of very hot Jupiters using transit light curves. *The Astrophysical Journal*, 698(2):1778–1794.

[Renaud, 2025] Renaud, J. P. (2025). TidalPy. *Zenodo Software*, 168:16883555.

[Rodríguez et al., 2026] Rodríguez, M. J., Santoni, L., and Solomon, A. R. (2026). Love numbers of black holes and compact objects. *arXiv preprint arXiv:2604.08653.*

[Saito, 1974] Saito, M. (1974). Some problems of static deformation of the Earth. *Journal of Physics of the Earth*, 22(1):123–140.

[Saito, 1978] Saito, M. (1978). Relationship between tidal and load Love numbers. *Journal of Physics of the Earth*, 26(1):13–16.

[Shida, 1912] Shida, T. (1912). On the body tides of the Earth, a proposal for the International Geodetic Association. *Proceedings of the Tokyo Mathematico-Physical Society. 2nd Series*, 6(16):242–258.

[Singh et al., 2023] Singh, S., Singh, J., Sharma, J., and Ram, J. (2023). High-pressure equations of state and elastic properties of the hcp-Iron. In *Journal of Physics: Conference Series*, volume 2426, page 012056. IOP Publishing.

[Sohl et al., 2003] Sohl, F., Hussmann, H., Schwentker, B., Spohn, T., and Lorenz, R. D. (2003). Interior structure models and tidal Love numbers of Titan. *Journal of Geophysical Research: Planets*, 108(E12).

[Sotin et al., 2007] Sotin, C., Grasset, O., and Mocquet, A. (2007). Mass–radius curve for extrasolar Earth-like planets and ocean planets. *Icarus*, 191(1):337–351.

[Spada et al., 2025] Spada, G., Melini, D., et al. (2025). *Glacial Isostatic Adjustment.* Springer.

[Takeuchi and Saito, 1972] Takeuchi, H. and Saito, M. (1972). Seismic surface waves. In *Methods in computational physics: Advances in research and applications*, volume 11, pages 217–295. Elsevier.

[Thomson, 1863] Thomson, W. (1863). XXVII. On the rigidity of the Earth. *Philosophical Transactions of the Royal Society of London*, (153):573–582.

[Thor et al., 2021] Thor, R. N., Kallenbach, R., Christensen, U. R., Gläser, P., Stark, A., Steinbrügge, G., and Oberst, J. (2021). Determination of the lunar body tide from global laser altimetry data. *Journal of Geodesy*, 95(1):4.

[Tinti and Zaniboni, 2025] Tinti, S. and Zaniboni, F. (2024/2025). Teaching material of "Numerical Geophysics Laboratory" class. *Alma Mater Studiorum - Università di Bologna*.

[Tsuchiya et al., 2004] Tsuchiya, T., Tsuchiya, J., Umemoto, K., and Wentzcovitch, R. M. (2004). Elasticity of post-perovskite MgSiO3. *Geophysical Research Letters*, 31(14).

[Turcotte and Schubert, 2002] Turcotte, D. L. and Schubert, G. (2002). *Geodynamics*. Cambridge university press.

[Udry et al., 2007] Udry, S., Bonfils, X., Delfosse, X., Forveille, T., Mayor, M., Perrier, C., Bouchy, F., Lovis, C., Pepe, F., Queloz, D., et al. (2007). The HARPS search for southern extra-solar planets-XI. Super-Earths (5 and 8 M) in a 3-planet system. *Astronomy & Astrophysics*, 469(3):L43–L47.

[Valencia et al., 2006] Valencia, D., O'Connell, R. J., and Sasselov, D. (2006). Internal structure of massive terrestrial planets. *Icarus*, 181(2):545–554.

[Valencia et al., 2007] Valencia, D., O'connell, R. J., and Sasselov, D. D. (2007). Inevitability of plate tectonics on super-Earths. *The Astrophysical Journal Letters*, 670(1):L45–L48.

[van Dijk and Miguel, 2025] van Dijk, E. and Miguel, Y. (2025). Retrieving interior properties of hot Jupiters with Love numbers and atmospheric measurements. *Monthly Notices of the Royal Astronomical Society*, 540(2):1544–1559.

[Van Heck and Tackley, 2011] Van Heck, H. and Tackley, P. (2011). Plate tectonics on super-Earths: Equally or more likely than on Earth. *Earth and Planetary Science Letters*, 310(3-4):252–261.

[Vermeersen et al., 1996] Vermeersen, L., Sabadini, R., and Spada, G. (1996). Compressible rotational deformation. *Geophysical Journal International*, 126(3):735–761.

[Wagner et al., 2012] Wagner, F., Tosi, N., Sohl, F., Rauer, H., and Spohn, T. (2012). Rocky super-Earth interiors-Structure and internal dynamics of CoRoT-7b and Kepler-10b. *Astronomy & Astrophysics*, 541:A103.

[Walker et al., 1981] Walker, J. C., Hays, P. B., and Kasting, J. F. (1981). A negative feedback mechanism for the long-term stabilization of Earth's surface temperature. *Journal of Geophysical Research: Oceans*, 86(C10):9776–9782.

[Wolszczan and Frail, 1992] Wolszczan, A. and Frail, D. A. (1992). A planetary system around the millisecond pulsar PSR1257+ 12. *Nature*, 355(6356):145–147.

[Wu and Ni, 1996] Wu, P. and Ni, Z. (1996). Some analytical solutions for the viscoelastic gravitational relaxation of a two-layer non-self-gravitating incompressible spherical earth. *Geophysical Journal International*, 126(2):413–436.

[Wu and Peltier, 1982] Wu, P. and Peltier, W. (1982). Viscous gravitational relaxation. *Geophysical Journal International*, 70(2):435–485.

[Zeng and Sasselov, 2013] Zeng, L. and Sasselov, D. (2013). A detailed model grid for solid planets from 0.1 through 100 Earth masses. *Publications of the Astronomical Society of the Pacific*, 125(925):227–239.

[Zeng et al., 2016] Zeng, L., Sasselov, D. D., and Jacobsen, S. B. (2016). Mass–radius relation for rocky planets based on PREM. *The Astrophysical Journal*, 819(2):127.

[Zhang, 1992] Zhang, C. (1992). Love numbers of the Moon and of the terrestrial planets. *Earth, Moon, and Planets*, 56(3):193–207.

[Zieba et al., 2026] Zieba, S., Kreidberg, L., Coy, B. P., Bello-Arufe, A., Paragas, K., Lyu, X., Hu, R., Iyer, A., Kite, E. S., Koll, D. D., et al. (2026). The dark and featureless surface of rocky exoplanet LHS 3844 b from JWST mid-infrared spectroscopy. *Nature Astronomy*, pages 1–16.